Advanced Flux Weakening Techniques for Surface-Mounted Permanent-Magnet Machine Drives

Thesis by

Dragan S. Marić

In Partial Fulfillment of the Requirements

for the Degree of

Doctor of Philosophy

California Institute of Technology

Pasadena, California

1999

(Submitted May 21, 1999)

To My Parents, Živana and Stanislav

Acknowledgements

First and foremost, I would like to thank my advisor, Professor David B. Rutledge, for his support, advice and understanding. I feel both honored and privileged to have been his student. I gratefully thank my research co-advisor from General Motors, Dr. Silva Hiti, for her continuous support, guidance and encouragement.

I acknowledge the financial support of General Motors Co., Advance Technology Vehicles – Torrance Operations, California. I would especially like to thank James M. Nagashima. I am grateful to Constantin C. Stancu for all insightful observations and fruitful brainstorming discussions we have had.

I have had the opportunity to live and work with many outstanding people at the Departments of Electrical Engineering and Control & Dynamic Systems, as well as from entire Caltech community. I have to thank Professor Arden Albee, the Dean of Graduate Studies, for his sincere help during the most critical moments of my stay at Caltech. I am also happy to have met Michael Linden-Martin, the person who made feasible my nascent adjustment to the new country, culture and language.

For my inaugural interest in the subjects of Power Electronics and Electrical Drives, the credit is due to Professor Slobodan N. Vukosavić of the University of Belgrade, Serbia, Yugoslavia, an exceptional person, pedagogue and engineer.

This endeavor would not have been possible without the love and irreplaceable support of my wife Natalia. She has been the only person able to properly understand my state of mind during various stages of my Caltech existence that included the wonderful excitement of studying and doing research with some of the World's most brilliant people,

as well as the seeming hopelessness of dealing with the occasional, unexpected, but earthly obstacles.

Finally, I ought to mention my family, old and new. The thesis is devoted to my parents, Živana and Stanislav, for they raised me and provided the proper education in Yugoslavia during the most difficult decades for our nation and our Fatherland. Also, my merriest memories from Yugoslavia inevitably encompass the one and only brother of mine, Vojkan. Here, in the New World, my days have been tremendously enriched by ceaseless encouragement I have gotten from my parents-in-law, Colonel and Mrs. Alfred H. Davidson III, and my brother-in-law, Miki.

Advanced Flux Weakening Techniques for Surface-Mounted Permanent-Magnet Machine Drives

Abstract

Surface-Mounted Permanent-Magnet Synchronous (SMPMS) machine drives have been considered thus far unsuitable for an efficient, wide-range flux weakening operation. This thesis will detail two novel schemes that provide stable and reliable operation over a wide range above the machine base speed, without dependence on machine parameters, usage of look-up tables or DC bus voltage measurements. Both techniques employ space vector modulation (SVM) with the option of smooth transition into six-step mode through the over-modulation range, maximizing the torque available. The first scheme ensures exact torque command tracking, whereas the second one intrinsically gives a steady state error in the flux weakening area. The second method, on the other hand, is computationally simpler, offers better transient response and the steady state torque error is not a critical feature if the torque control loop is an inner loop. The first method uses closed loop control of the phase voltage magnitude to generate magnetizing current reference for the flux-weakening operation. The second approach detects the steady-state error in the torque current component regulation, and then uses the error to generate the magnetizing current reference. However, when the over-modulation and six-step modes are utilized, the fifth and seventh stator current harmonics of the fundamental frequency propagate through the current control loops, resulting in the sixth harmonic in the current error signals and, henceforth, in the reference voltage duty cycles for the flux weakening control section. This deteriorates drive performance. To filter the sixth harmonic, a constrained lattice-structure allpass-based notch filter is used here, providing minimal phase delay and complete attenuation of the sixth harmonic. Similar filter solutions have been used so far only in certain communications and sonar applications, but this work sets a path for a broader utilization in electrical drive systems. Modeling and simulation techniques, design procedure, and experimental results will be presented. The results of this work proved that SMPMS machines are suitable for applications when the extended speed range was required, e.g., in electric propulsion.

Contents

Acknowledgements iv

Abstract vi

Chapter 1. Introduction 1

1.1. Motivation 2

1.2. Electric Propulsion Performance Requirements 3

1.3. Electric Propulsion as a Part of Electric Vehicle System 4

1.4. Electric Vehicle Propulsion Building Blocks 7

1.5. Organization of the Thesis 10

Chapter 2. Surface Mounted Permanent Magnet Synchronous Machine Drives Modeling 17

2.1. Permanent Magnet Synchronous Machines 18

2.2. Inverter and SMPMS Drive Control 27

2.3. Drive Simulation and Prototype Notes 35

Chapter 3. Flux Weakening for Surface Mounted Permanent Magnet Machine Drives 41

3.1. Flux Weakening Principles 42

3.2. Flux Weakening for High-Speed Operation of SMPMS Drives 44

3.3. A SMPMS Flux Weakening Scheme Using Closed-Loop Reference Voltage Control 49

3.4. A SMPMS Flux Weakening Scheme Using i_q Error Detection 62

3.5. Experiments 69

3.6. Concluding Remarks 76

Chapter 4. Filtering Techniques for Improved Performance of SMPMS Drives in the Flux Weakening Regime 81

4.1. Drive Performance Deterioration in Over-Modulation and Six-Step PWM Regimes 82

4.2. The Sixth Harmonic Filtering 84

4.3. Simulation 95

4.4. Experiment 97

4.5. Concluding Remarks 99

Chapter 5. Discussion and Suggestions for Future Work 102

Appendix A: Battery Technologies – An Overview 106

A.1. Batteries 106

A.2. Battery Charging 108

Appendix B: Permanent Magnet Materials 112

Chapter 1

Introduction

Recent developments in power electronics, permanent magnet (PM) materials, processors and micro-controllers, as well as in advanced control techniques, have significantly contributed to the widespread application of PM machines in various electrical drive systems: from motion control and aerospace implementations, to industry and automotive solutions. The most attractive features of PM synchronous motors are power density, torque-to-inertia ratio and electrical efficiency.

There are two major classes of PM synchronous machine drives which can be distinguished by the shapes of their back-EMF waveforms: sinusoidal or trapezoidal [1] – [3]. Sinusoidal PM drives share many of the basic characteristics of other classic types of polyphase AC motor drives. In particular, the machine current and back-EMF waveforms are practically sinusoidal for highly smooth torque generation [4]. Trapezoidal PM drives, also known as brushless DC drives, are designed to develop trapezoidal back-EMF. The excitation waveforms for three-phase trapezoidal PM machines take the form of quasisquare-wave current waveforms. The nature of the excitation in this case permits some important system simplifications compared to sinusoidal PM drives (e.g., reduced current and position sensor requirements) [3]. However, these simplifications make trapezoidal PM drives vulnerable to certain mechanisms of unwanted pulsating torque generation which do not afflict their sinusoidal counterparts [4]. This is the reason why sinusoidal PM machines

are more frequently chosen than trapezoidal PM machines for applications when minimization of torque pulsation is of a critical importance, e.g., in electric vehicles.

1.1 Motivation

The use of permanent magnets to generate substantial air gap magnetic flux without external excitation makes it possible to design PM machines with unsurpassed efficiency characteristics. This becomes more and more important all over the world where the laws of market and official mandates are putting the spotlight on reduced energy dissipation. For instance, the US government has gradually been imposing minimum energy efficiency requirements during the 1990s on major classes of residential appliances and heating, ventilating and air conditioning (HVAC) systems [4], [5].

The low losses made it feasible, by appropriate use of permanent magnets, to accomplish machine designs with impressive power density and torque-to-inertia ratio, as shown in [4]. This is why PM machines are very suitable for many applications that demand fast dynamic response.

An application that is favorable to all these advantages of PM machines is electric propulsion. Namely, for autonomous electric vehicles, when energy is provided from batteries, the drive efficiency is of a critical importance. The higher power density is desirable because of limited space on the vehicle. Transitions from motoring to regeneration regimes require fast dynamic response. Therefore, taking into account these characteristics, PM machines became very attractive for people involved in electric and hybrid-electric vehicle research programs [6] – [10].

1.2. Electric Propulsion Performance Requirements

Drive performance requirements that stem from characteristics of an electric propulsion system impose specific challenges to control design. Electric vehicle traction requires high torque ('constant torque' region) for low-speed acceleration and reduced torque for high-speed cruising ('constant power' region), [4], [6], [11] and [12].

Constant power operation poses special challenges for PM synchronous machines since there is no field winding which can be directly weakened as in conventional, separately excited DC and wound-rotor synchronous machines. Therefore, to achieve desired performance, a development of effective flux weakening control techniques for PM synchronous machines has recently been an exciting area of research in control of electrical drives, [13] – [21]. Thus far, interior PM synchronous machines have been considered more suitable for a wide flux weakening operation than surface-mounted PM synchronous (SMPMS) machines. However, the latter ones are less expensive and, hence, more attractive for practical implementation and industrial production. A thorough investigation of the possibility for high performance flux weakening methods for SMPMS machine drives has been needed.

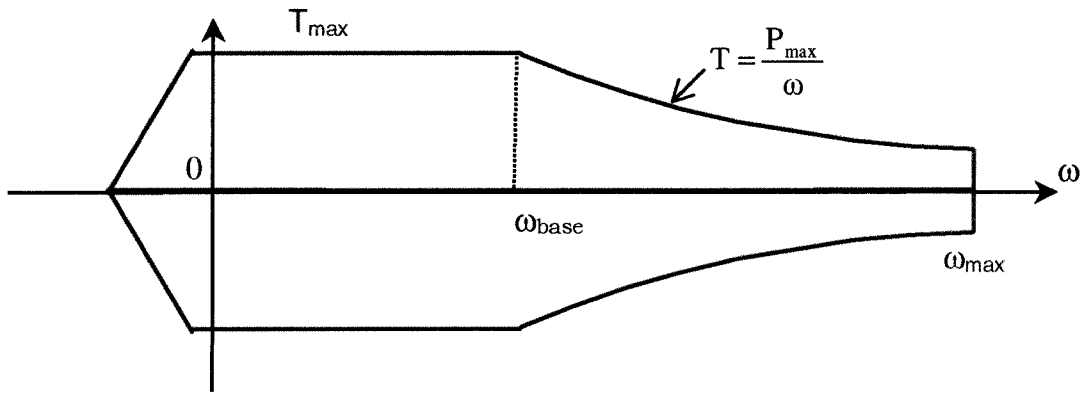

Fig. 1. 1. Typical torque-speed requirement for electric propulsion.

1.3. Electric Propulsion as a Part of Electric Vehicle System

The proper design of control techniques for electric propulsion requires that designers observe and fully understand the role of this subsystem as a part of the master system – here, the electric vehicle (EV). The system characteristics should not ever be viewed or determined as a mere collection of the characteristics of all corresponding subsystems. The additional system attributes originate in the interactions and type of interconnections among the subsystems, described in the general theory of systems as the synergy effect. A more elaborate discussion on this rather philosophical topic was presented in [22]. For this reason, a brief overview of an EV system is included here. The hybrid vehicle (HV) concept, Fig. 1.2, includes all components of an EV system, with addition of internal combustion engine (ICE) subsystem and all necessary interconnections. Insight into the EV system sets the foundations for a good understanding of HV systems, whose full description is beyond the scope of this work.

There are two basic methods for producing EV's, either to convert or to build for purpose. For the conversion method, the electric machine, controller, inverter and batteries replace the ICE and associated equipment. This offers some economy because the entire vehicle body is already there. However, in most cases, this method results in a greater weight, higher center of gravity and other weight distribution differences that can affect handling. The concepts of purpose-built EV's include the consistent weight-saving design, optimum safety concept, low-drag-coefficient body design, and low rolling resistance. Consequently, the purpose-built approach is a concept of choice for GM, Nissan, BMW and other car manufacturers at this moment [23] – [26].

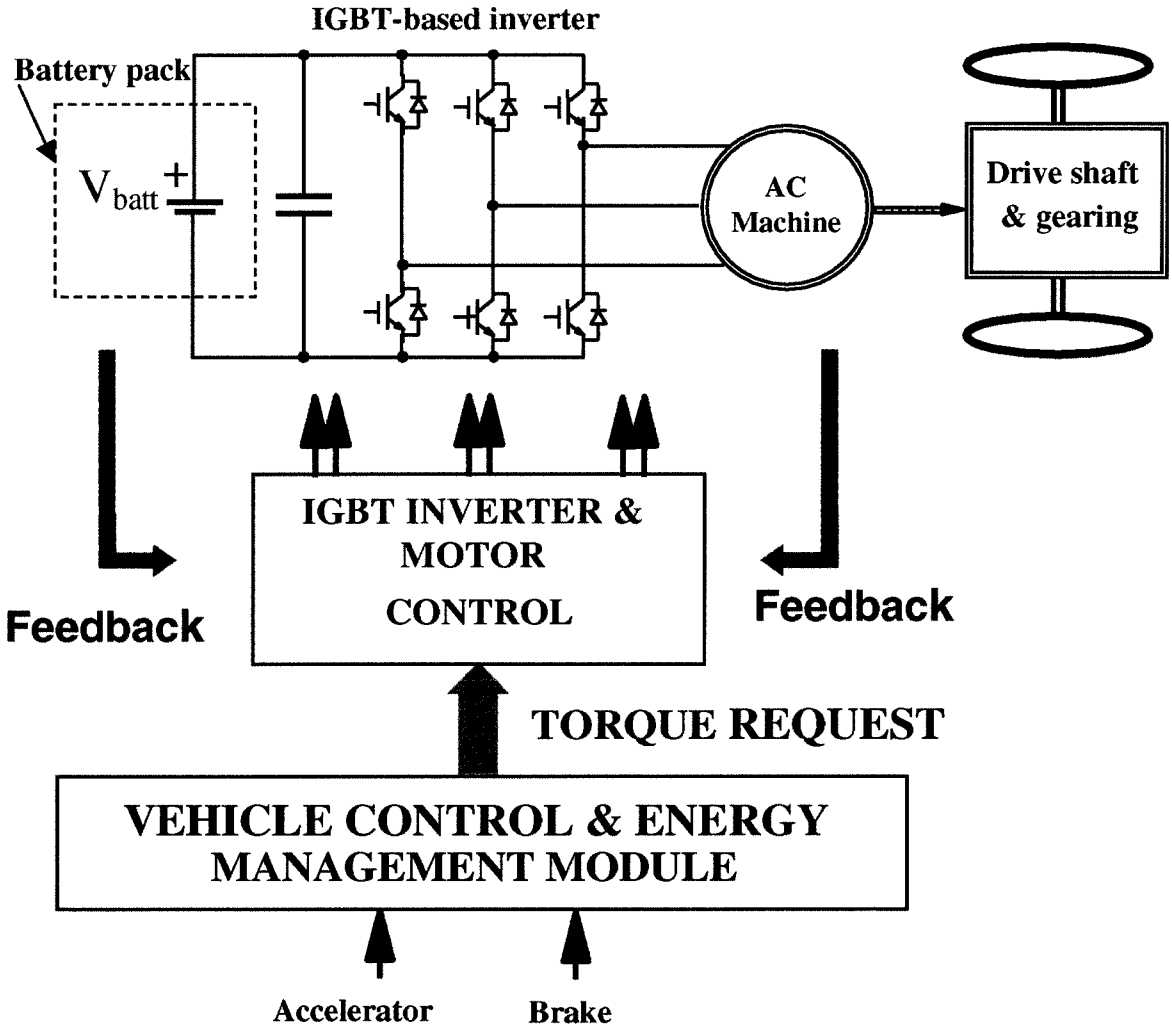

Fig. 1.2. Electric vehicle structural block-diagram.

The source of energy for EV's that are targeted for production are batteries. As the specific energy and specific power of electrochemical batteries are generally much smaller than those of gasoline, a large number of batteries are required to assure a desired level of power performance [27], [28]. The challenge of transforming EV's from concept to consumer product is to make it safe, convenient and easy for drivers to recharge batteries [29] – [32]. A short review of current battery technologies is given in the Appendix A. For the electric propulsion designer, a major difference here, when compared with industrial

motor drives, emerges from the fact that during the normal braking electric machine can operate as a generator. The braking energy is recuperated with high efficiency and batteries are recharged because the DC link between batteries and DC-AC inverter is energy bi-directional.

Electric propulsion interfaces energy supply with vehicle wheels, transferring energy in either direction as demanded, with highest possible efficiency, under driver's control at any instant [23]. An electric propulsion system consists of electrical and mechanical sections. The electrical part includes the machine, power converter and electronic controller, whereas the mechanical section encompasses the drive shaft, transmission, suspension and wheels. The boundary between these two sections is the air gap of the electric machine, where the electromechanical energy conversion takes place. The electric propulsion is a major power electronics application in an EV, frequently described as the EV's heart.

Maximizing energy usage and monitoring energy capacity are cardinal to attaining desired performance of an EV. The energy management module, Fig. 1.2, making use of sensory inputs from all subsystems of the vehicle, predicts vehicle range for standardized driving profiles, controls the energy usage of subsystems, suggests more efficient driving behavior, directs regenerated energy from braking to the batteries, selects a battery charging algorithm based on battery charge and cycle life history, modulates climate control in response to current driving conditions, and adjusts lighting brightness according to external light [23]. When the module is capable of communication with a navigation system (GPS), it is able to plan energy efficient routes, locate charger stations for long voyages, and modify its predictions in accordance with traffic conditions. Since the air conditioning, lamps, power steering, audio equipment and other accessories rely on diverse power converters to supply

energy from the batteries, the energy management module acts as a master controller for this purpose, [33], [34].

1.4. Electric Vehicle Propulsion Building Blocks

1.4.1 Electric Machine

Electric machines have been available for over a century. The evolution of machines, unlike that of electronics and computers, has been slow and long [23]. Nonetheless, the development of motors is ceaselessly fueled by novel technologies of high-energy permanent magnets, sophisticated motor topologies, and modern CAD techniques.

Traditional DC commutator machines have been prominent in early days of electric propulsion. Their control is straightforward. However, the principal problem of them arises from their commutators and brushes, which makes them less dependable and unsuitable for maintenance-free operation, the prime considerations in EV propulsion. Hence, the commutatorless AC machines have become the solution for automotive applications. AC induction motors are very reliable, robust (practically, maintenance-free) and quite inexpensive. However, their efficiency is significantly lower when compared with PM machines, since the machine magnetization is provided by an additional stator current component. On the other hand, in PM machines, magnets on the rotor provide lifelong excitation. The advantages of PM AC machines have been already outlined at the beginning of this chapter. Higher efficiency of PM drives results in higher vehicle mileage per battery charge. The only outlay is the initial cost of magnets, which reflects in the motor price. Because of the highest remanent induction and coercitivity, as well as reasonable cost, the NdFeB magnet is the choice nowadays [2], [3], [23], [35]. A review of PM technologies and physical characteristics is given in Appendix B.

1.4.2 Power Converters

In the past several years, power device technology has made tremendous progress [3], [23]. These devices have rapidly grown in ratings and performance. Among the power devices available, the gate-turnoff thyristor (GTO), power bipolar-junction transistor (BJT), metal-oxide field-effect transistor (MOSFET), insulated-bate bipolar transistor (IGBT), and MOS-controlled thyristor (MCT) are particularly popular for EV propulsion [23], [36]. GTO and power BJT require current gating, while MOSFET, IGBT and MCT operate with voltage gating. At present, as in the case given in Fig. 2, the IGBT (introduced first in mid-1980s [37]) is the most attractive because it possesses high input impedance and the high-speed switching characteristics close to those of power MOSFET, with the conductivity characteristics of a BJT.

The evolution of power converter topologies follows that of the power devices, aiming to achieve high power density, high efficiency and robust performance [3], [23]. For electric propulsion systems with AC machines, DC-AC inverters are used. In addition to conventional pulse-width modulated (PWM) inverters, novel inverter topologies and resonant inverters have been investigated. Potentially, the zero-voltage-switching (ZVS) or zero-current-switching (ZCS) inverters can offer almost zero switching loss, lower heat sinking requirement, less severe EMI problem, and reduced acoustic noise. However, given the present state of the market vis à vis additional prices of resonant components and the control circuitry added, the conventional bridge PWM topologies remain dominant for practical implementations, as in Fig. 2. The switching techniques used are very important aspects of the inverters. Numerous PWM switching schemes have been developed for battery-fed inverters, focusing on better utilization of the DC-link voltage, suitability for digital processor implementations and tolerance of the DC voltage fluctuations. The

modulation techniques can be classified [3] as the voltage-controlled PWM and current-controlled PWM [38]. This work encompasses a specific application of the space vector modulation (SVM) [39], [40], with over-modulation and smooth transition into the six-step mode [41], to assure electric vehicle maximal torque production by means of optimal DC bus voltage utilization.

1.4.3 Electronics Controllers

To implement modern control strategies, powerful microelectronics devices are necessary. This includes microprocessors, microcontrollers, digital signal processors (DSP), and transputers [23]. Unlike the microprocessor, which is the CPU of microcomputer systems, the microcontroller includes all resources to serve as stand-alone, single-chip controllers. Thus, microcontrollers assure that the minimum hardware configuration is achieved. However, their speed is frequently insufficient for modern control applied in high-performance EV systems. DSP's possess powerful computational capabilities. For instance, ADSP21xx and TMS320xx families are the most frequently used DSP's in power electronics and drives applications. The future solutions will certainly include broad application of transputers, which are particularly designed for parallel processing applications. Such powerful devices will expand the utilization of possible advanced control schemes even further, regarding the computational complexity of the techniques [42], [43].

The technologies involved in electric vehicles are diversified and, for the previously presented reasons, include electrical, mechanical, automotive, and chemical engineering. The designers of the electric propulsion control algorithms must be aware of what such a specific system imposes to their work, and to have a thorough understanding of the particularities in related subsystems given their interaction with electric propulsion section.

1.5. Organization of the Thesis

The major part of this thesis details two advanced flux weakening schemes for surface-mounted permanent magnet synchronous (SMPMS) machine drives. A new way to utilize SVM with over-modulation and six-step modes for maximal torque production and robust flux weakening control in SMPMS drives will be presented in Chapter 2. The drive control was realized in the *d-q* synchronous reference frame. Modeling oriented towards effective drive simulation and drive implementation will be described. The modulation technique was implemented in a battery fed drive. All models for the simulation were developed as the design aid for this intrinsically non-linear system.

Chapter 3 will discuss two advanced flux weakening schemes for SMPMS drives. The first one uses the reference voltage magnitude for control in the flux weakening section, i.e., to control the amount of injection of negative *d*-component of the stator current. The second method utilizes the *q*-axis current error for the same purpose. Both schemes were compared through simulation. The advantage of the first approach is that there is no steady state *q*-axis current error in the flux weakening region. Since electric propulsion requires a high level of torque linearity, the first scheme was chosen for the practical implementation. The experimental results confirmed theoretical and simulation predictions. The feed-forward terms were introduced into the current control loops, for approximate decoupling of *d* and *q* axes, resulting in better transient performance and stability at highest speeds.

In Chapter 4, further improvement of robust performance of the drive during the flux weakening operation was introduced. Although the over-modulation and six-step modes offer the maximal torque production, the stator current waveforms become distorted, with significantly higher harmonics content. In the flux weakening region, we always operate with this shape of stator currents. The most significant are the fifth and seventh harmonics that

propagate through the current control loop, resulting in the sixth harmonics being present in the flux weakening reference. As a solution, a constrained lattice-structure allpass-based filter has been utilized. The filter solutions from this part of signal processing theory have been used before in certain communications and sonar applications.

The subject of Chapter 5 is the direction for future research in high speed techniques for both SMPMS and interior PM drives, as well as discussion of possible extensions of signal processing techniques for other problems in control of power converters and electrical drives.

Parts of this work have been published in [9], [10] and [44].

Appendix A reviews the present status of the battery technologies as an important part of EV propulsion systems.

Appendix B briefly presents recent developments in permanent magnet materials, as the moving force for more frequent usage of PM machine drives.

References

[1] M. A. Rahman and P. Zhou, "Analysis of Brushless Permanent Magnet Synchronous Motors," *IEEE Trans. on Industrial Electronics*, vol. 43, pp. 256-267, April 1996.

[2] J. R. Hendershot and T. J. E. Miller, "Design of Brushless Permanent-Magnet Motors," Magna Physicsand Oxford Science Publications, 1994.

[3] B. K. Bose (editor), "Power Electronics and Variable Frequency Drives – Technology and Applications," IEEE Press, 1997.

[4] T. M. Jahns and W. L. Soong, "Pulsating Torque Minimization Techniques for Permanent Magnet AC Motor Drives – A Review," *IEEE Trans. on Industrial Electrnonics*, vol. 43, pp. 321-330, April 1996.

[5] "Manufacturers, Environmentalists Agree on National Appliance Standards," *Air Conditioning, Heating and Refrigeration News*, pp. 1, 21, August 18, 1986.

[6] M. Eshani, K. M. Rahman, and H. A. Toliyat, "Propulsion System Design of Electric and Hybrid Vehicles," *IEEE Trans. on Industrial Electronics*, vol. 44, pp. 19-27, February 1997.

[7] S. Henneberger, U. Pahner, K. Hameyer, and R. Belmans, "Computation of a Highly Saturated Permanent-Magnet Synchronous Motor for a Hybrid Electric Vehicle," *IEEE Trans. on Magnetics*, vol. 33, pp. 4086-4088, September 1997.

[8] C. C. Chan, K. T. Chau, J. Z. Jiang, W. Xia, M. Zhu, and R. Zhang, "Novel Permanent Magnet Motor Drives for Electric Vehicles," *IEEE Trans. on Industrial Electrnonics*, vol. 43, pp. 331-339, April 1996.

[9] D. S. Marić, S. Hiti, C. C. Stancu, J. M. Nagashima, and D. B. Rutledge, "Robust Flux Weakening Scheme for Surface-Mounted Permanent-Magnet Synchronous Drives

Employing an Adaptive Lattice-Structure Filter," *In Proc. of IEEE APEC99 Conference*, vol.1, pp. 271-276, March 1999.

[10] D. S. Marić, S. Hiti, C. C. Stancu, and J. M. Nagashima, "Two Improved Flux Weakening Schemes for Surface-Mounted Permanent-Magnet Synchronous Machine Drives Employing Space Vector Modulation," *In Proc. of IEEE IECON'98 Conference*, vol. 1, pp. 509-513, September 1998.

[11] B. Sneyers, G. Maggetto, and J. Van Eck, " Inverter Fed Permanent Magnet Motor for Road Electric Traction," *In proc. Int. Conf. on Electric Machines*, Budapest, pp. 550-553, September 1982.

[12] H. A. Toliyat, K. M. Rahman, and M. Eshani, " Electric Machines in Electric and Hybrid Vehicle Applications," *In Proc. 1995 Int. Conf. Power Electronics*, Seoul, Korea.

[13] G. Schaefer, "Field Weakening of Brushless PM Servomotors with Rectangular Current," *In Proc. EPE Conf.*, vol. 3, pp. 429-434, 1991.

[14] R. C. Becerra and M. Ehsani, "High-Speed Torque Control of Brushless PM Motors," *IEEE Trans. on Industrial Electronics*, vol. 35, pp. 402-405, August 1988.

[15] T. M. Jahns, "Flux Weakening Regime Operation of an Interior PM Synchronous Motor Drive," *IEEE Trans. on Industry Applications*, vol. 23, pp. 681-689, July/August 1987.

[16] S. Morimoto, Y. Takeda, and T. Hirasa, "Flux-Weakening Control Method for Surface Permanent Magnet Synchronous Motors," *In Proc. International Power Electronics Conference (IPEC)*, pp. 942-949, Tokyo, 1990.

[17] A. Kumamoto and Y. Hirane, "A Semi-Closed Loop Torque Control of a Buried Permanent Magnet Motor Based on a New Flux Weakening Approach," *In IEEE-IAS Annual Meeting Rec.*, pp. 656-661, 1989.

[18] A. Adnanes and T. Undeland, "Optimum Torque Performance in PMSM Drives above Rated Speed," *In IEEE-IAS Annual Meeting Rec.*, pp.169-175, 1991.

[19] W. Soong and T. J. E. Miller, "Theoretical Limitations to the Field-Weakening Performance of the Five Classes of Brushless Synchronous AC Motor Drive," *In Proc. IEE Conf. on Electric Machines and Drives*, 1993.

[20] J. H. Song, J. M. Kim, and S. K. Sul, "A New Robust SPMSM Control to Parameter Variations in Flux Weakening Region," *in Proc. IEEE IECON'96 Conf.*, pp. 1193-1198, 1996.

[21] S. D. Sudhoff, K. A. Corzine, and H. J. Hegner, "A Flux-Weakening Strategy for Current-Regulated Surface-Mounted Permanent-Magnet Machine Drives," *IEEE Trans. on Energy Conservation*, vol. 10, no. 3, Sep. 1995, pp. 431-437.

[22] D. S. Marić, "*Small Signal State Space Model of Induction and Synchronous Machines and Stability Analysis*," Dipl. Ing. Thesis (in Serbian), University of Belgrade, Yugoslavia, April 1994.

[23] C. C. Chan and K. T. Chau, "An Overview of Power Electronics in Electric Vehicles," *IEEE Trans. on Industrial Electronics*, vol. 44, pp. 3-13, February 1997.

[24] F. A. Wyezalek, "GM Electric Vehicle Technology," *In Proc. of International Symposium on Automotive Technology Automation*, pp. 271-277, 1991.

[25] N. Irie, M. Fukino, and H. Horie, "Nissan FEV – A New Concept Electric Vehicle," *In Proc. of Electric Vehicle Symposium*, no. 13.02, 1992.

[26] K. Faust, A. Goubeau, and K. Scheuerer, "Introduction to the BMW-E1," *SAE SP-915*, pp. 33-40, 1990.

[27] W. H. Deluca, A. F. Tummilllo, J.E. Kulaga, C. E. Webster, K. R. Gillie, and R. L. Hogrefe, "Performance Evaluation of Advanced Battery technologies for Electric

Vehicle Applications," *In Proc. of Intersoc. Energy Conversion Eng. Conference*, pp. 314-319, 1990.

[28] D. Coates and L. Miller, "Advanced Batteries for Electric Vehicle Applications," *In Proc. of International Electric Vehicle Symposium*, no. 14.03, 1992.

[29] J. K. Nor, "Fast Charging Advances the Art of refueling Electric Vehicles," *In Proc. of International Symposium on Automotive Technologies Automation*, pp. 65-72, 1991.

[30] S. T. Hung, D. C. Hopkins, and C. R. Mosling, " Extension of Battery Life via Charge Equalization Control," *IEEE Trans. on Industrial Electronics*, vol. 40, pp. 96-104, 1993.

[31] "Electric Vehicle Chargers," Hughes Power Control Systems, Torrance, CA, 1992.

[32] C. A. Bleijs and J. L. Mazoyer, "Preparing the Infrastructure for the Charging of Tomorrow's Electric Cars," *In Proc. of International Electric Vehicle Symposium*, no. 9.02, 1992.

[33] J. Dieckmann and D. Mallory, "Variable Speed Compressor, HFC-134a Based Air Conditioning System for Electric Vehicles," *SAE SP-915*, pp. 87-91, 1992.

[34] "Electric Vehicle Power Accessories," Hughes Power Control Systems, Torrance, CA, 1992.

[35] M. Sagawa, S. Fugimura, H. Yamamoto, and Y. Maysuura, "New Material for Permanent Magnets on a Base of Nd and Fe," *In Journal Applied Physics*, vol. 55, no. 6, pp. 2083-2087, 1984.

[36] M. Fracchia, T. Ghiara, and M. Marchesoni, "Generalized Design of Power Converters for Electric Vehicle," *In Proc. of International Vehicle Symposium*, no. 16.01, 1992.

[37] B. J. Baliga, M. S. Adler, P. V. Gray, R. P. Love, and N. Zommer, "The Insulated Gate Transistor," *IEEE Trans. on Electron Devices*, vol. ED-31, pp. 821-828, 1984.

[38] J. Holtz, "Pulse-width Modulation – A Survey," *IEEE Transactions on Industrial Electronics*, vol. 39, pp. 410-420, October 1992.

[39] S. Hiti, *"Modeling and Control of Three-Phase PWM Converters,"* Ph.D. dissertation, VPI&SU, Blacksburg, VA, 1995.

[40] V. R. Stefanović and S. N. Vukosavić, "Space-Vector PWM Voltage Control with Optimized Switching Strategy," *In Proc. of IEEE IAS Annual Meeting 1992,* pp. 1025~1033, 1992.

[41] J. Holtz, W. Lotzkat, and A. Khambadkone, "On Continuous Control of PWM Inverters in the Overmodulation Range Including the Six-step Mode," *In Proc. of IEEE IECON'92 Conference*, pp. 307~312, November 1992.

[42] D. Q. Zhang, C. Cecati, and E. Chiricozzi, "Some Practical Issues of the Transputer Based Real Time Systems," *In Proc. of IEEE IECON'92 Conference*, pp. 1403-1407, November 1992.

[43] P. C. K. Luk, "On Applying Parallel Processing to a Versatile Induction Motor System," *In Proc. of IEEE IECON'93 Conference*, pp. 907-912, November 1993.

[44] D. S. Marić, S. Hiti, C. C. Stancu, J. M. Nagashima, and David B. Rutledge, "Two Flux Weakening Schemes for Surface-Mounted Permanent-Magnet Synchronous Drives – Design and Transient Response Considerations," *accepted for publication and presentation at IEEE ISIE'98 Conference*, July, 1999.

Chapter 2

Surface Mounted Permanent Magnet Synchronous Machine Drives Modeling

Synchronous permanent magnet (PM) electric machines use magnets to produce the air gap magnetic field rather than requiring a magnetizing component of stator current as in an induction motor. Significant advantages arise from the simplification in construction, the reduction in losses and the improvements in efficiency. Modern brushless PM synchronous motors may operate near unity power factor and have a large pullout torque for a given frame size.

In Chapter 1, the significance of the maximal battery voltage utilization in electric propulsion (EP) was highlighted. This work includes a description of a new application of the space vector modulation (SVM) with over-modulation in a PM-based electric propulsion system. The advantageous features of SVM technique for maximal torque production are described here. Further exploitation of its characteristics is also essential for flux weakening methods, which is presented in succeeding chapters.

The theoretical results are used to create efficient original EP simulation models. An EP system is, from the control point of view, a highly non-linear environment. This motivates the development of simulation replicas of the system for benign analysis and testing of control algorithms. Once the theoretical control algorithms are verified this way, we can more confidently proceed towards the implementation in real drive prototype.

2. 1. Permanent Magnet Synchronous Machines

Depending on the location of the magnets on the rotor, typical PM synchronous machines can be broadly classified into two groups, interior PM synchronous (IPMS) that have PM's buried inside the rotor, Fig. 2.1, and surface mounted PM synchronous (SMPMS), which have their PM's mounted on the surface of the machine rotor, Fig. 2.2, [1] – [3]. For three phase PM machines of power levels necessary for electrical traction, the stator configuration is made as standard sinusoidally distributed three phase windings, Fig. 2.3, i.e., the stator is the same as in induction machines, which minimizes manufacturing cost.

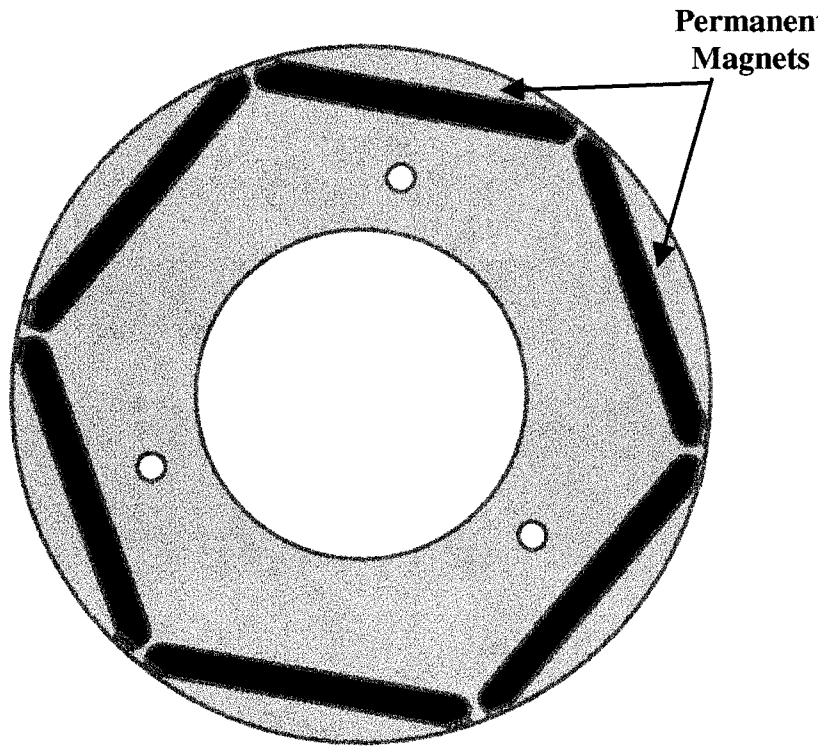

Fig. 2.1. Rotor of IPMS machine.

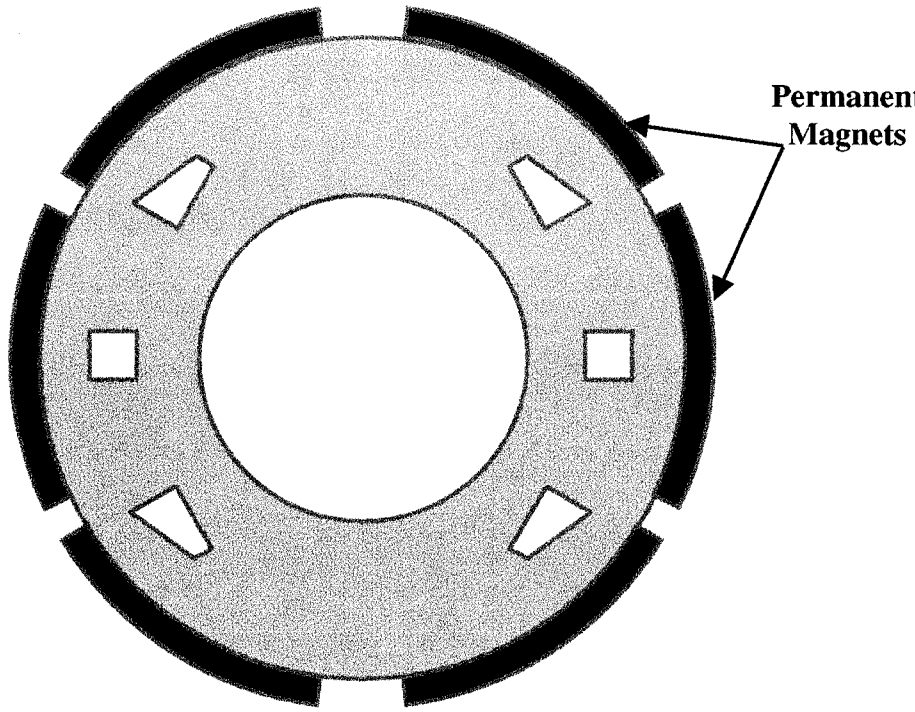

Fig. 2.2. Rotor of a SMPMS machine.

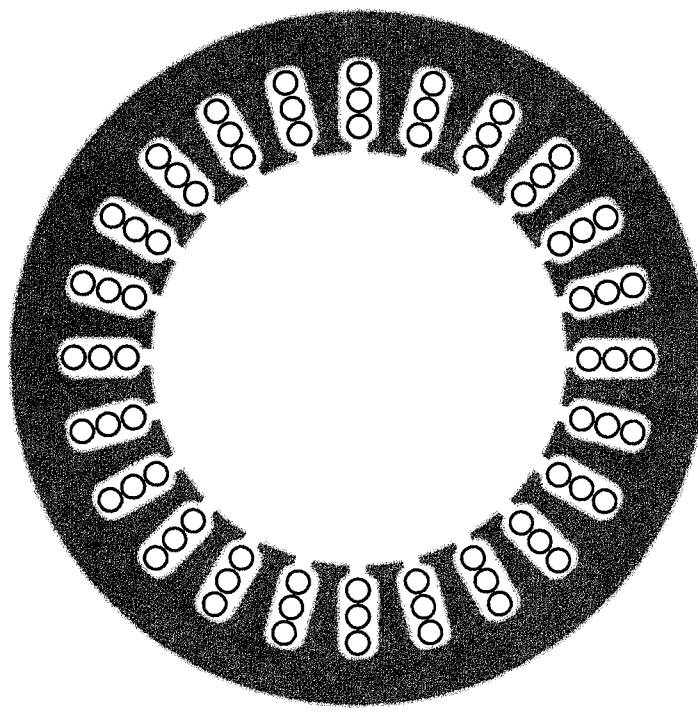

Fig. 2.3. Typical AC machine stator.

According to Kirchhoff's voltage law, for all three windings we can write the following voltage equations at the stator terminals, as in [1], [4], [5]:

$$v_a = R_a i_a + \frac{d\psi_a}{dt}$$

$$v_b = R_b i_b + \frac{d\psi_b}{dt} \qquad (2\text{-}1)$$

$$v_c = R_c i_c + \frac{d\psi_c}{dt}$$

In case of a standard, symmetric machine, stator phase resistances are equal: $R_a = R_b = R_c = R$. Flux linkages are related to stator currents as follows:

$$\begin{bmatrix} \psi_a \\ \psi_b \\ \psi_c \end{bmatrix} = \begin{bmatrix} L_a(\theta) & L_{ab}(\theta) & L_{ac}(\theta) \\ L_{ba}(\theta) & L_b(\theta) & L_{bc}(\theta) \\ L_{ca}(\theta) & L_{cb}(\theta) & L_c(\theta) \end{bmatrix} \cdot \begin{bmatrix} i_a \\ i_b \\ i_c \end{bmatrix} + \begin{bmatrix} k_0 \cos\theta \\ k_0 \cos(\theta + 120^0) \\ k_0 \cos(\theta + 240^0) \end{bmatrix} \cdot \psi_{PM} \qquad (2\text{-}2)$$

The inductances in (2-2) depend on the rotor angle θ between rotor flux ψ_{PM} axis and stator phase *a* axis, Fig. 2.4. The coefficient k_0 describes the portion of PM flux that crosses the phase *a* plane when *a* axis and ψ_{PM} are aligned (ideally, $k_0=1$). Magnetic saturation effects are not discussed in this work. They are not significant in SMPMS machines because the effective air gap is large. However, when necessary, this consideration can be included, as in [6] and [7] for instance. Equations (2-1) and (2-2) describe the electrical subsystem of the machine. Kirchhoff's current law implies $i_a+i_b+i_c=0$. The machine magnetic circuit is designed in such a way that the axial flux reluctance is much higher than radial flux reluctance, which implies $\psi_a+\psi_b+\psi_c=0$, as mentioned in [8]. Therefore, there are only two linearly independent currents and only two linearly independent flux linkages, which suggests that the three phase machine can be represented with an equivalent two phase machine.

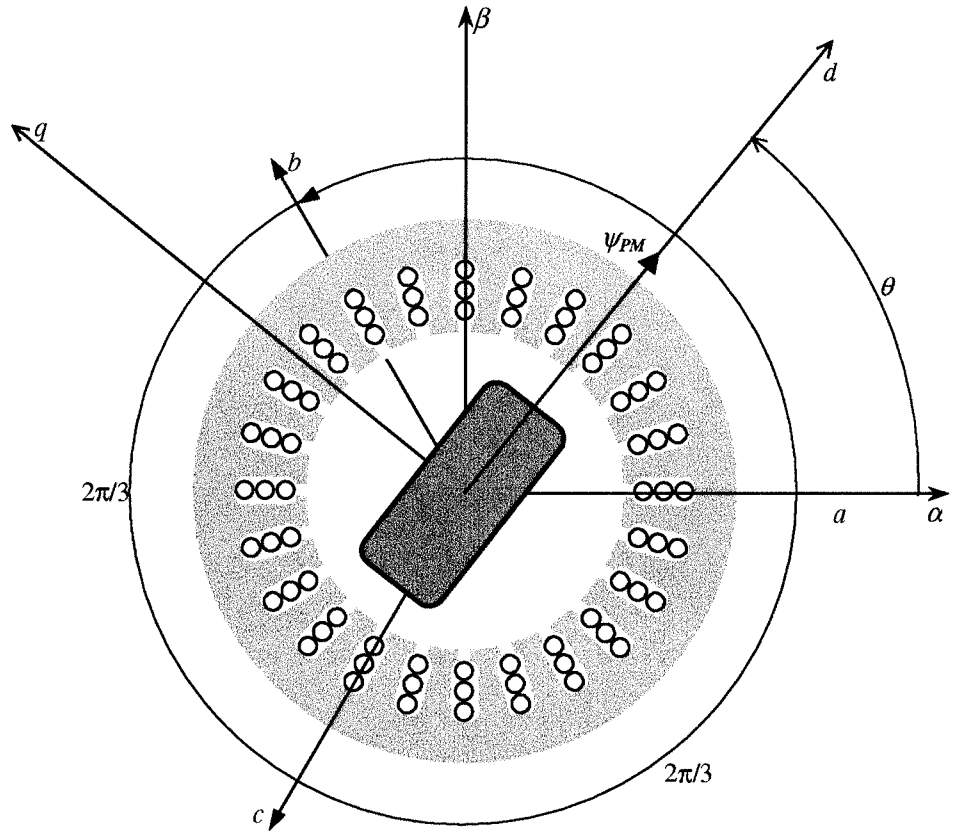

Fig. 2.4. Illustration of the rotational transformation.

If the equivalent two phase machine has two stationary orthogonal windings α and β, where α axis is aligned with the axis of stator phase *a*, Fig. 2.4, then the transformed two phase quantities are related to the corresponding three phase physical values as ([2], [4], [5]):

$$\begin{bmatrix} x_\alpha \\ x_\beta \end{bmatrix} = \frac{2}{3}\begin{bmatrix} 1 & -\frac{1}{2} & -\frac{1}{2} \\ 0 & \frac{\sqrt{3}}{2} & -\frac{\sqrt{3}}{2} \end{bmatrix} \cdot \begin{bmatrix} x_a \\ x_b \\ x_c \end{bmatrix} = \mathbf{C} \cdot \begin{bmatrix} x_a \\ x_b \\ x_c \end{bmatrix} \tag{2-3}$$

Here, x can be voltage, current or flux from previous equations. The new variables in α–β stationary reference frame are time dependent in both transient regime and steady state.

When the shaft speed is constant, these variables are sinusoidal and their angular frequency is equal to the electrical value of the angular rotor speed.

If we now transform these coordinates into a *d-q* coordinate system that rotates synchronously with rotor, as shown in Fig. 2.4, voltages, currents and fluxes become constant in a steady state. The position of *d-q* system relative to the stationary system is given by angle θ. The transformation matrix is defined as:

$$\begin{bmatrix} x_d \\ x_q \end{bmatrix} = \begin{bmatrix} \cos\theta & \sin\theta \\ -\sin\theta & \cos\theta \end{bmatrix} \cdot \begin{bmatrix} x_\alpha \\ x_\beta \end{bmatrix} = \mathbf{D} \cdot \begin{bmatrix} x_\alpha \\ x_\beta \end{bmatrix}; \qquad \theta = \theta(0) + \int_0^t \omega_e d\tau \tag{2-4}$$

Here, ω_e is electrical rotor speed (rad/sec), related to the mechanical rotor speed as $\omega_e = \omega P$, where P is number of machine pole pairs. The direct transformation from *a,b,c* system to the *d-q* system can be performed by using **B=DC** conversion matrix:

$$\begin{bmatrix} x_d \\ x_q \end{bmatrix} = \frac{2}{3} \begin{bmatrix} \cos\theta & \cos(\theta - 120^0) & \cos(\theta - 240^0) \\ -\sin\theta & -\sin(\theta - 120^0) & -\sin(\theta - 240^0) \end{bmatrix} \cdot \begin{bmatrix} x_a \\ x_b \\ x_c \end{bmatrix} = \mathbf{B} \cdot \begin{bmatrix} x_a \\ x_b \\ x_c \end{bmatrix} \tag{2-5}$$

The equivalence of a two phase system with three phase system can be also illustrated by observing the resulting rotating field produced by these winding systems. In the case of sinusoidally distributed windings, we can write, [5], the expressions for magnetic induction resulting from a symmetric system of sinusoidal three phase currents in stator, as:

$$\begin{aligned} B_a &= B_m \cos(\omega_e t)\cos\theta \\ B_b &= B_m \cos(\omega_e t - 120^0)\cos(\theta - 120^0) \\ B_c &= B_m \cos(\omega_e t - 240^0)\cos(\theta - 240^0) \end{aligned} \tag{2-6}$$

The magnetic induction is then a rotating wave:

$$B_{tot} = B_a + B_b + B_c = \frac{3}{2} B_m \cos(\omega_e t - \theta) \tag{2-7}$$

Two phase sinusoidally distributed perpendicular x and y windings, with currents mutually shifted in phase for 90^0, produce:

$$\begin{aligned} B_x &= B_M \cos(\omega_e t)\cos\theta \\ B_y &= B_M \cos(\omega_e t - 90^0)\cos(\theta - 90^0) \end{aligned} \tag{2-8}$$

The resulting magnetic induction wave in the air gap is now of the form equivalent to (2-7):

$$B_{tot} = B_x + B_y = B_M \cos(\omega_e t - \theta) \tag{2-9}$$

After the transformation **B** is performed, the PM machine model in the synchronous *d-q* reference frame becomes ($\psi_{df}=k_0\psi_{PM}$) [4], [5]:

$$\begin{aligned} v_d &= Ri_d + L_d \frac{di_d}{dt} - \omega_e L_q i_q \\ v_q &= Ri_q + L_q \frac{di_q}{dt} + \omega_e L_d i_d + \omega_e \psi_{df} \end{aligned} \tag{2-10}$$

For a SMPMS machine, we have $L_d=L_q=L$. The flux and current vectors are: $\boldsymbol{\psi}=\psi_{df}\mathbf{d}_0$ and $\mathbf{i}=i_d\mathbf{d}_0+i_q\mathbf{q}_0$, where $\mathbf{d}_0$ and $\mathbf{q}_0$ are the axes unit vectors in the *d-q* coordinate system. Hence, the machine produced electromechanical torque is [5]:

$$\mathbf{T_e} = \frac{3}{2} P\boldsymbol{\psi} \times \mathbf{i} = \frac{3}{2} P\psi_{df} i_q \mathbf{o}_0, \qquad T_e = \frac{3}{2} P\psi_{df} i_q \tag{2-11}$$

Here, $\mathbf{o}_0$ is the unit vector perpendicular to the *d-q* plane, pointing in the direction of the machine shaft, and P is the number of machine pole pairs.

The machine's mechanical subsystem is described by Newton's equation:

$$J\frac{d\omega}{dt} = T_e - T_{load} \tag{2-12}$$

J is the total moment of inertia on the shaft, T_{load} is the load torque and ω is the rotor mechanical speed in rad/sec.

The additional equations are necessary to correlate the electrical speed, mechanical speed and rotor angle:

$$\omega_e = P\omega = \frac{d\theta}{dt} \tag{2-13}$$

Equations (2-10), (2-11) and (2-12) suggest that the field oriented control can be directly implemented in the *d-q* reference frame [4]. The vector diagram is given in Fig. 2.5, and it is commensurate with the derived mathematical model.

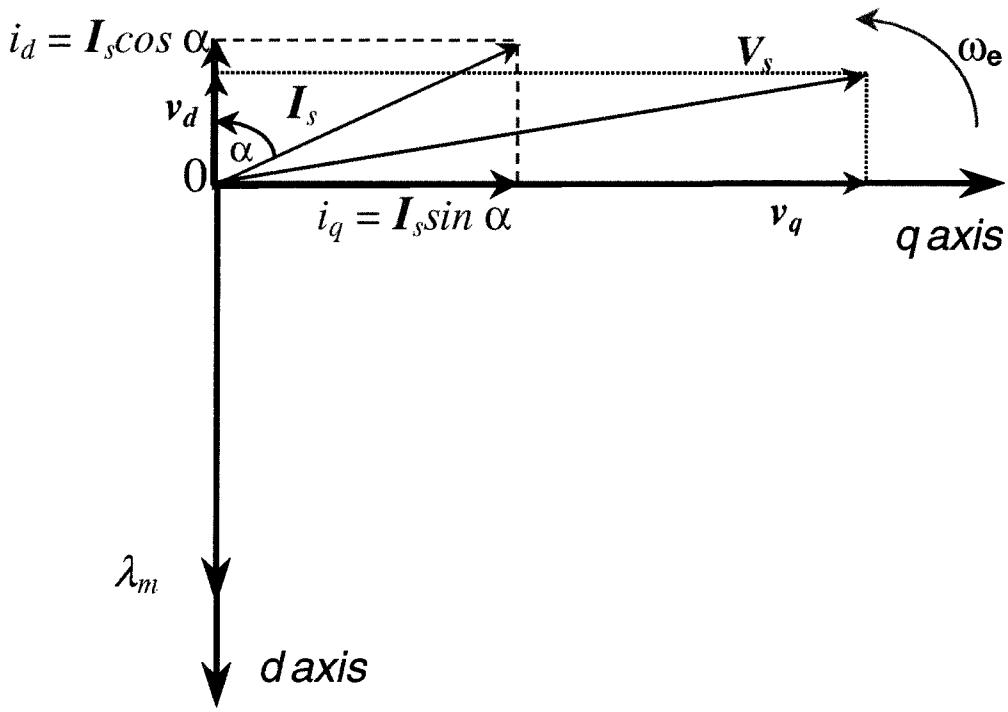

Fig. 2.5. Vector diagram of a PM machine.

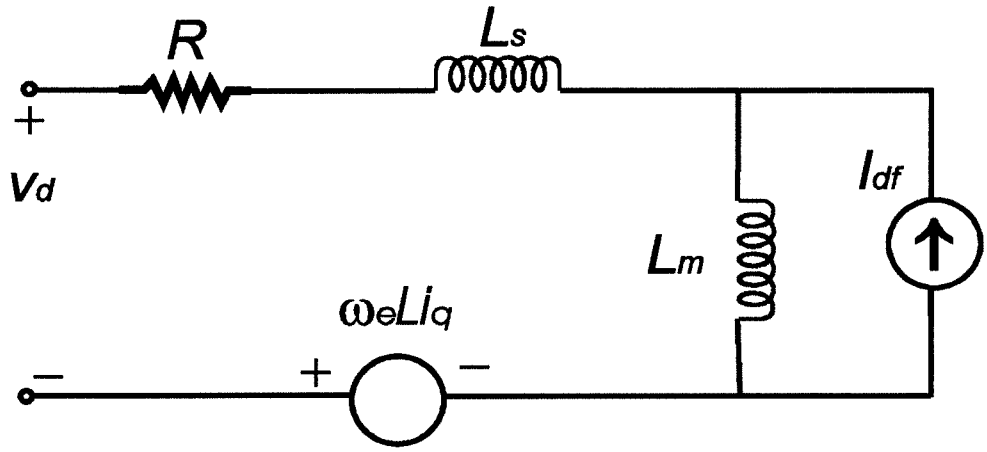

a)

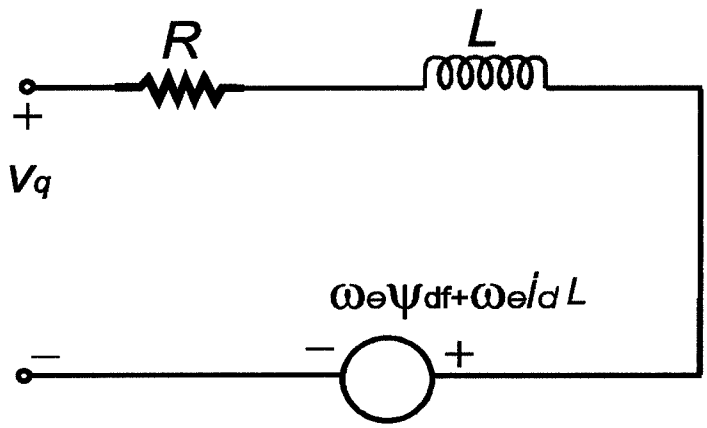

b)

Fig. 2.6. Coupled *d-q* equivalent circuits for a SMPMS machine in the synchronous reference frame.

The SMPMS machine equivalent circuits are given in Fig. 2.6, drawn according to equations (2-10). There, L_s is the leakage inductance of the machine, and magnetizing inductance is calculated as $L_m=L-L_s$, [2], [4], [5]. The magnet flux source is represented by the equivalent current source $I_{df}=\psi_{df}/L_m$ and appears in the *d* axis, whereas the resulting back EMF appears as a dependent voltage source in the *q* axis circuit (term $\omega_e\psi_{df}$). The similar circuits can be used for an IPM machine as well. In that case, the inductances L_s and L_m in

Fig. 2.6.a. become L_{sd} and L_{md} respectively, and L in the back EMF source is then L_q. Likewise, in Fig. 2.6.b inductance L ought to be L_q, and L in the back EMF source is now L_d.

These equivalent circuits are used in development of a new SMPMS drive simulation model to represent the electrical subsystem of the machine. This allows us to model the entire drive system (including control algorithms, PWM inverter techniques, as well as the mechanical subsystem) and observe the performance of each subsystem.

Even though some simulators, like *SABER*™, permit direct modeling of mechanical subsystems, equations (2-11) – (2-13) in this case, a significant simulation time savings and the model complexity reduction can be accomplished by employing the analogy between mechanical and electrical quantities, Table 2.1.

MECHANICAL	ELECTRICAL
Torque T (Nm)	Current I (A)
Angular speed ω (rad/sec)	Voltage V (V)
Inertia J (kgm^2)	Capacitance C (F)
Friction coefficient k_F (kgm^2/rad)	Resistance R (Ω)

Table 2.1. Analogy between mechanical and electrical quantities.

A usual assumption is that the load torque can be expressed as a sum of a constant (speed independent) value T_c=*const.* and a friction term $k_F\omega$:

$$T_{load} = T_c + k_F\omega \tag{2-14}$$

The resulting equivalent circuit of the machine mechanics is then given in Fig. 2.7.

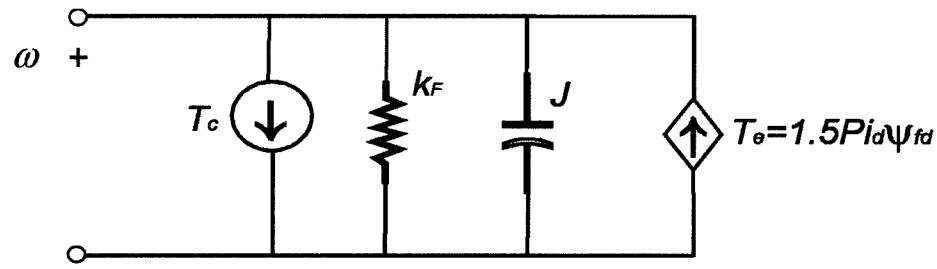

Fig. 2.7. Equivalent electrical circuit of SMPMS machine mechanical subsystem.

2. 2. Inverter and SMPMS Drive Control

A general block diagram of the drive control is given in Fig. 2.8. The control is implemented in a digital signal processor (DSP), [9]. The stator current control is realized using the previously described *d-q* model, equations (2-10) – (2-13). Fast proportional-integral (PI) controllers are employed here. The inverter, its average model and a new application of the space vector modulation (SVM) for maximal EP torque production will be described here. The flux weakening section and current controller design considerations are subjects of the forthcoming chapters.

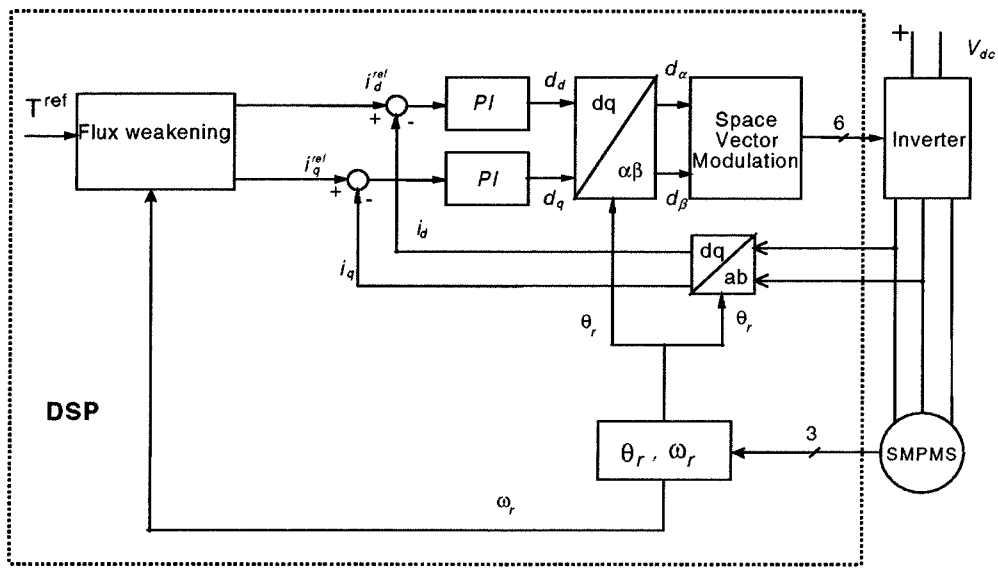

Fig. 2.8. Inverter and SMPMS drive control.

2.2.1. Three Phase Inverter for SMPMS Drive

The IGBT inverter is a standard three phase topology, Fig. 2.9. The switching strategy of choice is the SVM, [2], [10] – [12], which provides maximal DC voltage utilization. To increase maximum torque available, over-modulation and six-step are used to provide maximal fundamental amplitude of the inverter output voltage. This method is explained later in the chapter.

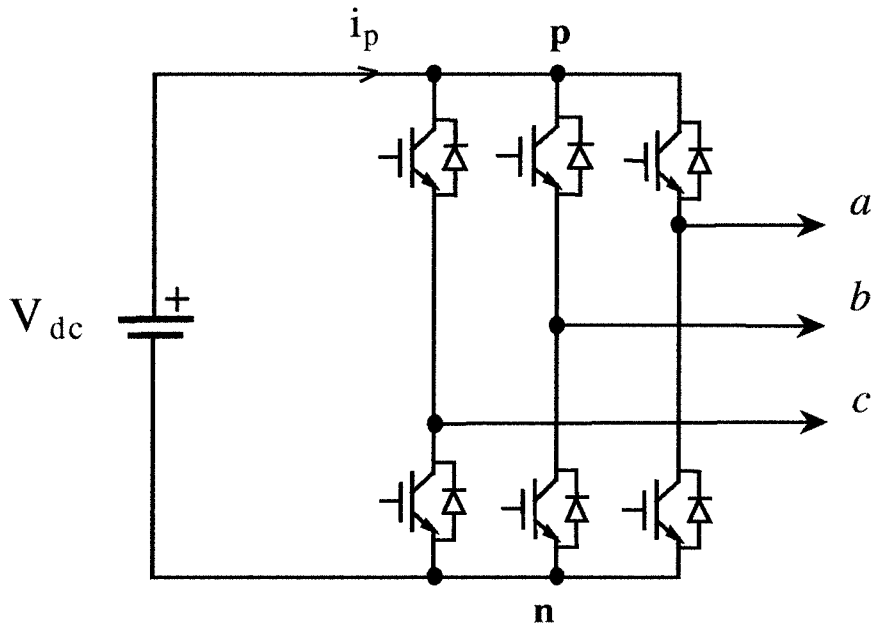

Fig. 2.9. An IGBT-based three phase voltage source inverter (VSI).

For simulation model used as a development assistance tool here, a tremendous acceleration of the simulation time can be achieved by using the average inverter model, [9]. However, the simulation models for inverter fault modes must include a full-blown switching model of the inverter in order to analyze non-symmetric modes of operation. The state space averaged circuits have been previously described in [11], [13] – [15]. Whereas the circuit presented in [11] includes a detailed modeling of second order effects that exist in a real converter, a less complex version, Fig. 2.10, was used here, providing good environment for the development and verification of drive control strategies.

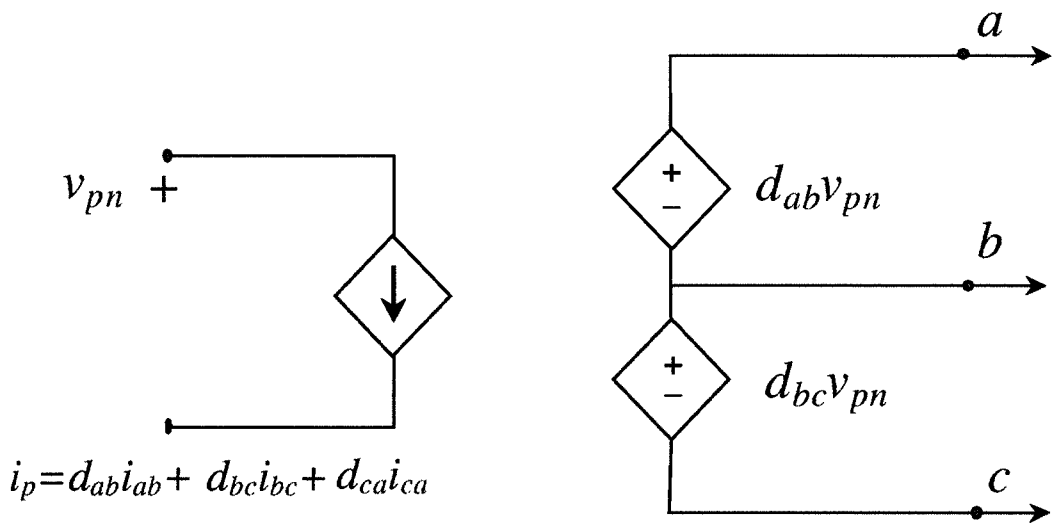

Fig. 2.10. Average model of a voltage source inverter.

The method of averaging used to develop circuit in Fig. 2.10. was described in [11] and is derived based on previous results given in [16] – [18]. For a DC-DC converter operating in the continuous conduction mode, the state-space model is:

$$\frac{d\mathbf{x}}{dt} = (1 - s(t))\mathbf{f}_0(\mathbf{x}) + s(t)\mathbf{f}_1(\mathbf{x}) \tag{2-15}$$

where *s(t)* is the active switch switching function (1 for time instants when switch is on, 0 when it is off) and *1-s(t)* is the passive switch switching function. In steady state, the converter goes through cyclic changes of the two switching configurations, and the resulting state trajectories are periodic with the switching period T_s. Time-invariant state space equations that describe the average circuit behavior over the whole switching period are obtained through averaging, as presented in [16] – [18]:

$$\frac{d\bar{\mathbf{x}}}{dt} = (1 - \bar{s}(t))\mathbf{f}_0(\bar{\mathbf{x}}) + \bar{s}(t)\mathbf{f}_1(\bar{\mathbf{x}}); \qquad \bar{z}(t) = \frac{1}{T_s}\int_t^{t+T_s} z(\tau)d\tau \tag{2-16}$$

The moving average d of the switching function $s(t)$ is usually referred to as the switching duty cycle. In three phase converters, the moving average values of all variables are functions of time even in a steady state. It was shown in [11] that for a VSI, the model in Fig. 2.10 is:

$$\overline{i_p} = \overline{\mathbf{s}_\nabla^{\mathrm{T}} \cdot \mathbf{i}_\nabla} = \begin{bmatrix} \bar{s}_{ab} & \bar{s}_{bc} & \bar{s}_{ca} \end{bmatrix} \cdot \mathbf{i}_\nabla = \begin{bmatrix} d_{ab} & d_{bc} & d_{ca} \end{bmatrix} \cdot \mathbf{i}_\nabla = \mathbf{d}_\nabla^{\mathrm{T}} \cdot \mathbf{i}_\nabla$$

$$\bar{\mathbf{v}}_\nabla = \mathbf{d}_\nabla \bar{v}_{pn} \tag{2-17}$$

where:

$$\mathbf{i}_\nabla = \frac{1}{3}\begin{bmatrix} i_a - i_b \\ i_b - i_c \\ i_c - i_a \end{bmatrix} = \begin{bmatrix} i_{ab} \\ i_{bc} \\ i_{ca} \end{bmatrix}; \quad \mathbf{s}_\nabla = \begin{bmatrix} s_{ap} - s_{bp} \\ s_{bp} - s_{cp} \\ s_{cp} - s_{ap} \end{bmatrix} = \begin{bmatrix} s_{ab} \\ s_{bc} \\ s_{ca} \end{bmatrix}; \quad \mathbf{v}_\nabla = \begin{bmatrix} v_a - v_b \\ v_b - v_c \\ v_c - v_a \end{bmatrix} = \begin{bmatrix} v_{ab} \\ v_{bc} \\ v_{ca} \end{bmatrix} \tag{2-18}$$

To prevent shorting the DC bus voltage source and to provide paths for inductor currents, one and only one switch per inverter leg must be closed at any time. The allowed switching combinations are listed in Table 2.2, referring to the notation in Fig. 2.9.

	a	***b***	***c***
0	*p*	*p*	*p*
1	*p*	*p*	*n*
2	*p*	*n*	*p*
3	*p*	*n*	*n*
4	*n*	*p*	*p*
5	*n*	*p*	*n*
6	*n*	*n*	*p*
7	*n*	*n*	*n*

Table 2.2. Switching combinations for a voltage source inverter.

These constraints can be expressed in terms of switching functions as:

$$s_{ap} + s_{an} = 1, \qquad s_{bp} + s_{bn} = 1, \qquad s_{cp} + s_{cn} = 1, \qquad \text{at an time.} \tag{2-19}$$

2.2.2. Space Vector Modulation with Over-Modulation and Six-Step Modes

Modern AC drives with gate-commutated switches use various pulse width modulation (PWM) methods for voltage or current control. The desirability of a method to be used, [12], depends on a high utilization of the DC bus voltage, dynamic response, harmonic distortion of the output waveform for a given switching frequency, as well as on the ease of implementation.

The most preferred PWM technique today is space vector modulation (SVM), [2], [10] – [12], [19], which offers a sinusoidal output voltage mode with 15% better DC bus utilization and 33% fewer commutations per switching period than conventional sinusoidal PWM. This work includes a description of previously unpublished usage of SVM for EP maximal torque production, further expanded by employing over-modulation and a smooth transition into six-step mode, as well as utilization of SVM properties for novel SMPMS flux weakening techniques.

The SVM can be effectively explained by using the space vector representation of a three phase variable [2]:

$$\underline{\mathbf{x}}(t)=\frac{2}{3}\left(x_1(t)+x_2(t)e^{-j\frac{2\pi}{3}}+x_3(t)e^{-j\frac{4\pi}{3}} \right), \tag{2-20}$$

where $x_1(t)$, $x_2(t)$ and $x_3(t)$ are arbitrary functions of time that, at any instant, satisfy:

$$x_1(t)+x_2(t)+x_3(t)=0 \quad . \tag{2-21}$$

Henceforth, the duty cycle space vector resulting from symmetric sinusoidal voltage system of frequency ω_e is [2]:

$$\underline{\mathbf{d}}=de^{j\omega_e t} \quad . \tag{2-22}$$

Fig. 2.11 shows this vector in a complex plane that is aligned with axes of the α-β reference frame. The switching vectors from Table 2.2 determine the vertices of the hexagon.

$$\underline{\mathbf{d}} = d_\alpha + jd_\beta = \frac{2}{3}\left(d_a + d_b e^{-j\frac{2\pi}{3}} + d_c e^{-j\frac{4\pi}{3}} \right) \quad . \tag{2-23}$$

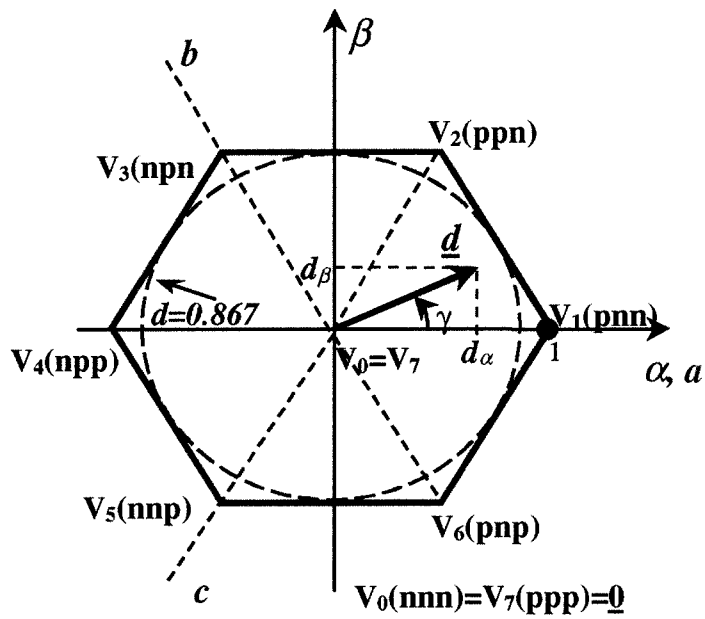

Fig. 2.11. Switching state vectors and reference duty cycle vector in a complex (α-β) plane.

The reference duty cycle vector $\underline{d}$ is sampled at the fixed clock frequency f_s. Then, the sampled value can be approximated by two neighboring switching vectors ($\mathbf{V}_1$ and $\mathbf{V}_2$ in Fig. 2.11) and one zero vector, [2], [10], [11], resulting in corresponding duty cycles for each of the necessary vectors:

$$d_1 = d(\cos\gamma - \frac{1}{\sqrt{3}}\sin\gamma), \qquad d_2 = \frac{2}{\sqrt{3}} d\sin\gamma, \qquad d_0 = 1 - d_1 - d_2 \quad . \tag{2-24}$$

It is apparent from the averaging approach of the SVM technique that the *on* duration of a zero vector ($t_0 = d_0/f_s$) decreases as the length of the reference vector increases. When d_0 reaches zero, it means that the circular path of the reference vector $\underline{d}$ touches the hexagon from inside. This is the boundary of the sinusoidal mode (at that moment: $d = 0.867$) because the circles of a bigger diameter have portions located out of the hexagon, i.e., the circle is, then, to be constrained to the physical limit given by hexagon edges. An additional singular operating point exists in the six-step mode. It is characterized by the following switching sequence: $\mathbf{V_1 - V_2 - \ldots - V_6}$, and yields the highest possible fundamental output voltage, [10], corresponding to $d = 0.956$. Control in the intermediate range $0.867 < d < 0.956$ can be achieved by over-modulation, [10].

The over-modulation technique subdivides into two different modes. In the first mode, the modified trajectory of the reference vector follows the circle as long as the circle arc is situated within the hexagon, Fig. 2.12; the modified vector tracks the hexagon edge in the remaining portions.

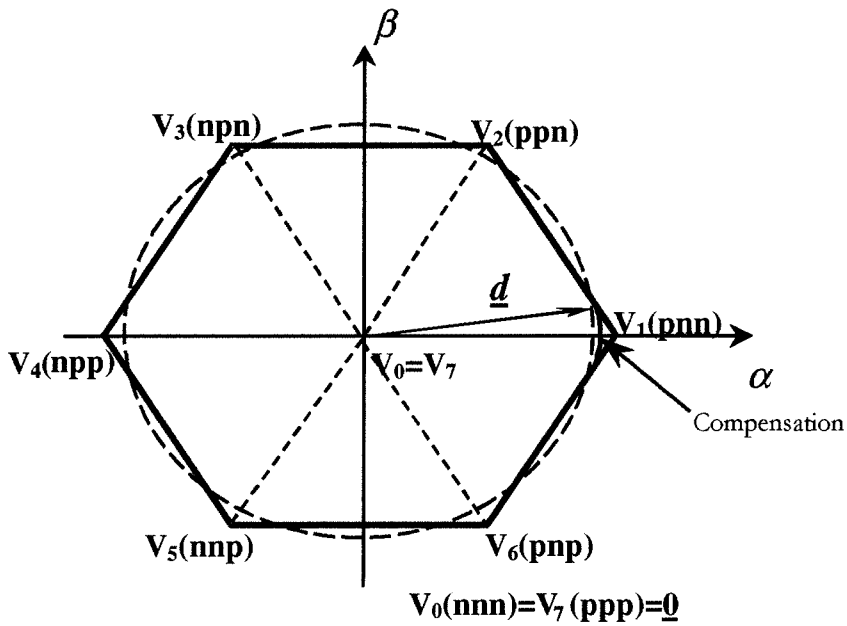

Fig. 2.12. Over-modulation.

Expression (2-24) is used when the modified reference is on the arc. When it follows the hexagon edge, the duty cycles become:

$$d_1 = \frac{\sqrt{3}\cos\gamma - \sin\gamma}{\sqrt{3}\cos\gamma + \sin\gamma}, \qquad d_2 = 1 - d_1, \qquad d_0 = 0 \tag{2-25}$$

To compensate for the voltage loss due to the limit along the hexagon edge, the modified vector can be extended when it is within the hexagon, Fig. 2.12. This compensation is fully implemented in our drive prototype.

The first over-modulation mode reaches its limit when the trajectory of the modified reference vector is the hexagon ($d = 0.907$). During the second mode, $0.907 < d < 0.956$, detailed in [10], as d gradually approaches 0.956, the modified reference tends to get locked at the corners of the hexagon for an increasing time period. The lock-in time reaches 1/6 of the fundamental period when the second over-modulation mode has smoothly converged into six-step operation. In this mode, the reference vector length is modified (to fit within the available physical limit), as well as the phase of the vector, according to:

$$\gamma_p = \begin{cases} 0; & 0 \le \gamma \le \gamma_h \\ \dfrac{\gamma - \gamma_h}{\pi/6 - \gamma_h} \cdot \dfrac{\pi}{6}; & \gamma_h < \gamma < \dfrac{\pi}{3} - \gamma_h \\ \dfrac{\pi}{3}; & \dfrac{\pi}{3} - \gamma_h \le \gamma < \dfrac{\pi}{3} \end{cases} \tag{2-25}$$

The hold angle determines the lock-in time and is changed according to the value of d to ensure smooth transition into the six-step mode [10]. The normalized sketch of the d_α (which is directly proportional to the phase voltage v_a) is given in Fig. 2.13.

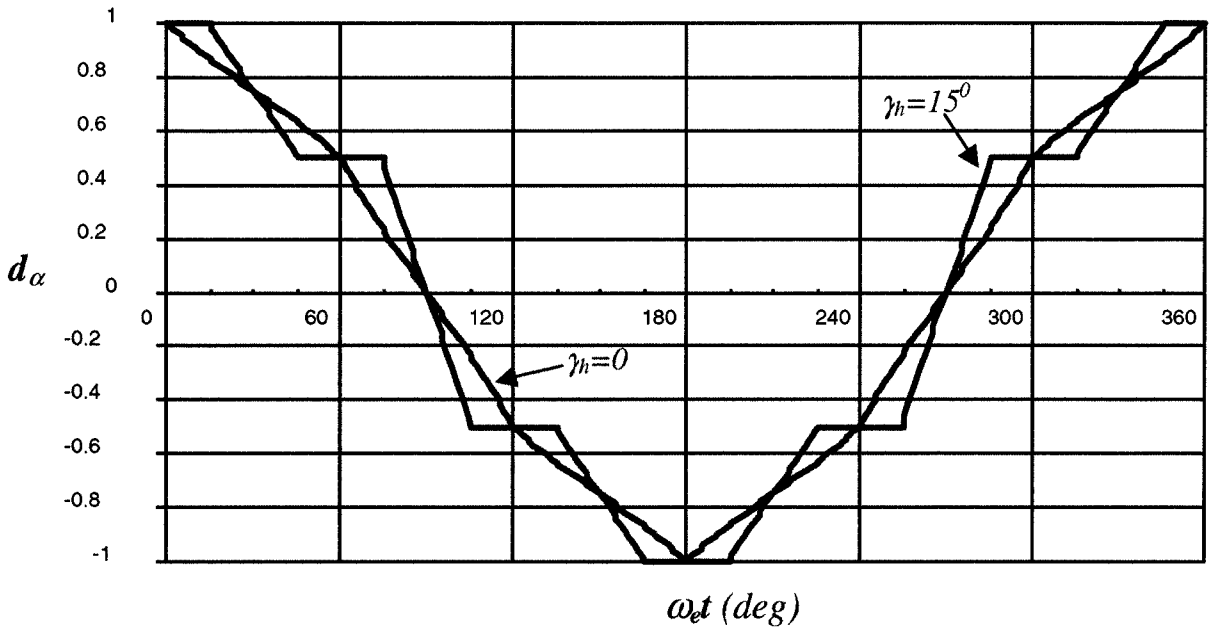

Fig. 2.13. Transition into the six-step mode by gradual increase of the hold angle (lock-in time).

We observe that the hexagon boundary of the mode 1 ($\gamma_h = 0$) produces a piece-wise linear, hexagon-like shape of the phase voltage, Fig. 2.13. As we proceed toward the full six-step mode, the flat portions become longer because lock-in times, i.e., γ_h values, increase.

2. 3. Drive Simulation and Prototype Notes

The work on this project included development and full implementation of these models in three different simulators (*Analog Workbench*™, *MATLAB/SIMULINK*™ and *SABER*™). The simulation results are presented and used throughout the remaining part of the thesis. The *Analog Workbench* models proved to be fastest for inverter operation and circuit model simulations. On the other hand, the control algorithms are most efficiently verified using the *MATLAB/SIMULINK* model. *SABER* gave the optimal performance of

a fully assembled drive model because of its suitable environment for integration of the electrical circuit section, blocks in *Z* (discrete time) and Laplace domains and the actual software routines implemented in *C* computer language.

The drive prototype was put together and tested in the 100KW AC dynamometer laboratory at General Motors ATV – Torrance Operations. The SMPMS machine used was of a twelve-pole, water-cooled, automotive type, with continuous power rating of 40 KW, as well as a 75KW two-minute power rating. Other relevant machine parameters are given in Table 2.3. The rotor position detection was implemented using inexpensive Hall-effect sensors placed inside the machine and mutually shifted for 120^0 degrees.

R	0.02 Ω
L	0.2 mH
J	0.05 kgm^2
ω_{base} (at 250Vdc)	2300 rpm
λ_m	0.08 Wb
ω_{max}	8100 rpm

Table 2.3. The drive prototype: SMPMS machine parameters.

As a power stage, an IGBT-based, water-cooled inverter was used. The IGBT modules with built-in diodes had 600V/600A maximum voltage and current ratings. The experiments were carried out with both Pb-acid battery and stiff-output laboratory voltage DC sources as energy supplies for up to 350VDC.

The control board included *Analog Devices'* 16-bit, fixed-point digital signal processor from *ADSP21xx* family, operating at 24MHz-clock frequency. This processor offered a good balance between speed and cost, which is particularly important for commercial

applications. However, all algorithms for the real-time control had to be implemented in the processor's assembly language. A fast PWM co-processor was used for implementation of the SVM techniques.

References

[1] M. A. Rahman and P. Zhou, "Analysis of Brushless Permanent Magnet Synchronous Motors," *IEEE Trans. on Industrial Electronics*, vol. 43, pp. 256-267, April 1996.

[2] B. K. Bose (editor), "Power Electronics and Variable Frequency Drives – Technology and Applications," IEEE Press, 1997.

[3] A. G. Jack and A. J. Mitcham, "Design and Initial Test Results for a Permanent Magnet Synchronous Motor for a Vehicle Drive," *In Proc. of Conference on Electric Machines*, pp. 751-757, Manchester, UK, September 1992.

[4] D. W. Novotny and T. A. Lipo, "Vector Control and Dynamics of AC Drives," Calderon Press • Oxford, 1996.

[5] P. C. Krause, "Analysis of Electric Machinery," McGraw Hill, 1986.

[6] P. Vas, M. Alakula and K. E. Hallenius, "Field-Oriented Control of Saturated AC Machines," *In Record of the Third IEE International Conf. on Power Electronics and Variable Speed Drives*, pp. 283-286, London, 1988.

[7] R. D. Lorentz and D. W. Novotny, "Saturation Effects in Field Oriented Induction Machines," *In Proc. of IEEE IAS Annual Meeting*, pp. 150-155, October 1987.

[8] S. N. Vukosavić, "Design of Adaptive Algorithms for Microprocessor-Based Velocity and Position Control of an Induction Motor Drive," Ph.D. dissertation (in Serbian), University of Belgrade, 1989.

[9] D. S. Marić, S. Hiti, C. C. Stancu and J. M. Nagashima, "Two Improved Flux Weakening Schemes for Surface-Mounted Permanent-Magnet Synchronous Machine Drives Employing Space Vector Modulation," *In Proc. of IEEE IECON'98 Conference*, vol. 1, pp. 509-513, September 1998.

[10] J. Holtz, W. Lotzkat and A. Khambadkone, "On Continuous Control of PWM Inverters in the Overmodulation Range Including the Six-step Mode," *in Proc. IECON '92*, pp. 307-312, 1992.

[11] S. Hiti, *"Modeling and Control of Three-Phase PWM Converters,"* Ph.D. dissertation, VPI&SU, Blacksburg, VA, 1995.

[12] V. R. Stefanović and S. N. Vukosavić, "Space-Vector PWM Voltage Control with Optimized Switching Strategy," *In Proc. IEEE IAS Annual Meeting 1992,* pp. 1025-1033, 1992.

[13] J. R. Wood, "Power Conversion in Electrical Networks," *Topical Report*, Harvard University, 1974.

[14] R. D. Middlebrook and S. Ćuk, "A General Unified Approach to Modeling Switching-Converter Power Stages," *In Rec. of IEEE PESC'76*, pp. 18-34, 1976.

[15] G. W. Wester and R. D. Middlebrook, "Low-Frequency Characterization of Switched DC-DC converters," *In Rec. of IEEE PESC'72*, pp. 9-20, 1972.

[16] S. R. Sanders, J. M. Noworolski, X. Z. Liu, and G. C. Verghese, "Generalized Averaging Method for Power Conversion Circuits," *IEEE Trans. on Power Electronics*, vol. 6, no. 2, pp. 251-259, 1991.

[17] J. M. Noworolski and S. R. Sanders, "Generalized In-Place Circuit Averaging," *In Rec. of IEEE PESC'91*, pp. 445-450, 1991.

[18] S. R. Sanders and G. C. Verghese, "Synthesis of Averaged Circuit Models for Switched Power Converters," *IEEE Trans. on Circuits and Systems*, vol. 38, no. 8, pp. 905-915, 1991.

[19] H. W. van der Broeck, H. C. Skudelny, and G. V. Stanke, "Analyses and Realization of a Pulsewidth Modulator Based on Voltage Space Vectors," *IEEE Trans. on Industry Applications*, vol. 24, no. 1, pp. 142-150, 1988.

[20] D. S. Marić, S. Hiti, C. C. Stancu, J. M. Nagashima, and D. B. Rutledge, "Robust Flux Weakening Scheme for Surface-Mounted Permanent-Magnet Synchronous Drives Employing an Adaptive Lattice-Structure Filter," *In Proc. of IEEE APEC99 Conference*, vol. 1, pp. 271-276, March 1999.

[21] D. S. Marić, S. Hiti, C. C. Stancu, J. M. Nagashima, and David B. Rutledge, "Two Flux Weakening Schemes for Surface-Mounted Permanent-Magnet Synchronous Drives – Design and Transient Response Considerations," *accepted for publication and presentation at IEEE ISIE'98 Conference*, July, 1999.

Chapter 3

Flux Weakening for Surface Mounted Permanent Magnet Synchronous Machine Drives

Due to their distinct characteristics, but also because of improvements in and reduced cost of permanent magnet technologies, PM machines have been used in many electrical drive applications. Some applications, like electrical traction, require a wide operating range above the motor base speed, i.e., a wide region of flux weakening operation, as mentioned in Chapter 1. Thus far, SMPMS machines have been predominantly considered unsuitable for an effective, wide-range flux weakening operation. The efficiency of SMPMS machines suffers at high speeds due to the large magnetizing current component needed for flux weakening. In addition, it is difficult to achieve stable motor operation at elevated speeds.

This chapter describes, in detail, two advanced schemes that provide stable and reliable operation over the EP required velocity range above base speed of a SMPMS machine, without dependence on conditions in drive environment, machine parameters, usage of look-up tables or DC bus voltage measurement. Both schemes employ space vector modulation with the option of smooth transition into six-step mode through the over-modulation region, as presented in Chapter 2. The first scheme ensures exact torque command tracking, whereas the second method intrinsically gives a steady state torque error in the flux weakening region. The second technique, on the other hand, is computationally

simpler and offers advantageous performance during transients. Its steady state torque error is not a critical feature if the torque control loop is an inner loop, e.g., in velocity control schemes and positioning servomechanisms.

3.1. Flux Weakening Principles

Prior to the development of modern DC-AC conversion systems, high performance electrical drives were the province solely of DC machines with mechanical commutators and brushes. The torque available was limited by the maximal values of field and armature currents (motor and DC power supply limitations), by the maximal voltage available from the power supply and by the maximal current that could be handled by the brushes and commutator at a given speed [1].

The basic principle of flux weakening was first fully developed in separately excited DC machines. If the field and armature currents are set to their maximum permissible values, [1], the maximal machine torque that can be delivered to the mechanical load is:

$$T_{emax} = K_T \psi_{fmax} I_{amax} \tag{3-1}$$

where the flux is $\psi_{fmax} = L_f I_{fmax}$, I_{amax} is the maximum field current and I_{amax} is the maximum armature current. K_T is the motor torque constant.

As the speed of the DC machine increases, the voltage applied to the motor must increase to match the back electromotive force (EMF), which is given by:

$$E = K_E \psi_f \omega_m \tag{3-2}$$

where K_E is the back EMF constant of the machine and ω_m is the machine speed. Finally, at a certain speed, the voltage of any real power supply cannot be increased further to maintain the armature current at the maximum value I_{amax}. If the field current is not changed at this

moment, the armature current, and consequently the output torque, will drop to zero. Hence, the torque control can be kept beyond this speed only if the back EMF is controlled in such a manner that it always stays below the maximum supply voltage, leaving a sufficient voltage margin for i_a. This is rendered by decreasing the field current, i.e., ψ_f. The minimum filed current at any speed is determined by the maximum allowed armature current. The back EMF remains constant by decreasing the field current (and, hence, the flux and the torque) in inverse proportion to the speed. Therefore, the output power is constant. This is the reason why the flux weakening operation is frequently referred to as a 'constant power operation'. The ideal flux weakening characteristics are given in Fig. 3.1.

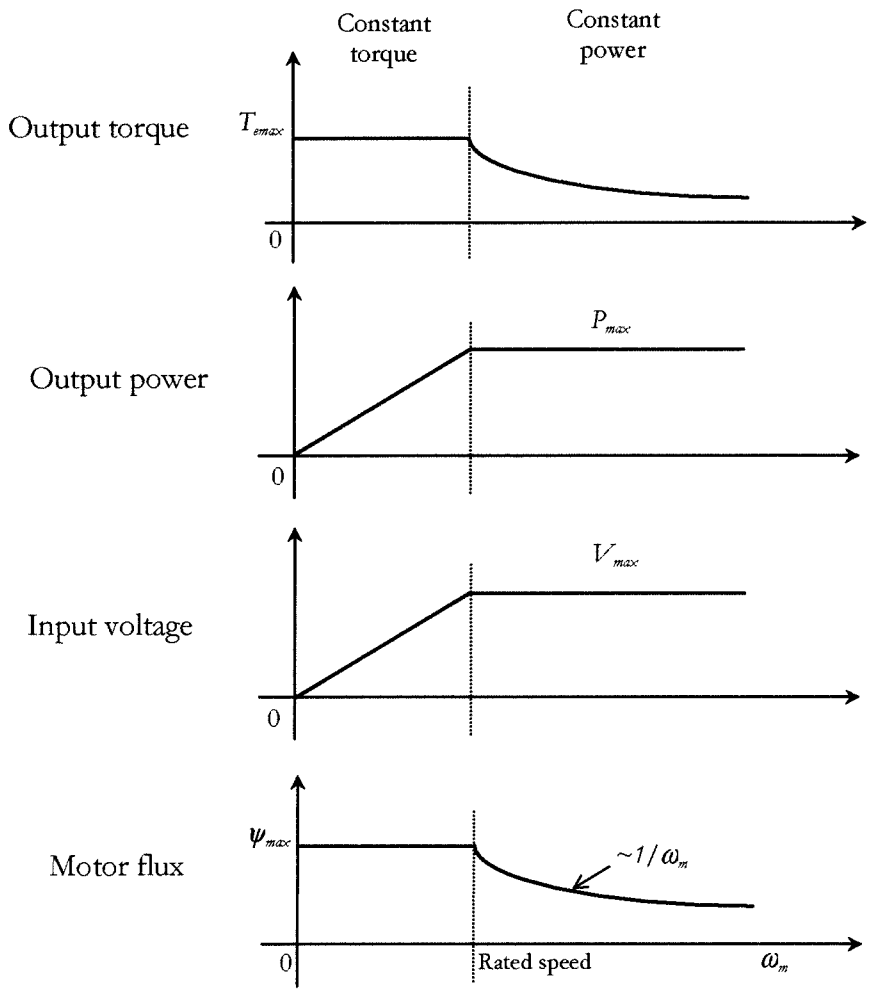

Fig. 3.1. Ideal flux weakening drive characteristics.

3.2. Flux Weakening for High-Speed Operation of SMPMS Drives

The amplitude of the back EMF for any PM AC machine increases linearly with rotor speed [2] – [4]. Then (similarly to the behavior of DC machine drives summarized above), unless special steps are undertaken, both the phase current amplitude and the motor torque fall off quite abruptly as the rotor speed crosses the critical value. At the critical point, the magnitude of the phase back EMF reaches maximum available magnitude of the phase voltage supplied by the DC-AC inverter.

To understand the limits of high-speed operation in SMPMS machines, it is useful to commence the discussion by considering the impact of the voltage and current constraints that the inverter imposes [3] – [6]. Namely, the maximum allowable motor phase voltage and phase current are determined by the inverter and machine ratings and by the DC bus voltage V_{dc}. As shown in Chapter 2, the PM synchronous machine modeling in a synchronous reference frame yields:

$$v_d = Ri_d + L_d \frac{di_d}{dt} - \omega_e L_q i_q \tag{3-3}$$

$$v_q = Ri_q + L_q \frac{di_q}{dt} + \omega_e L_d i_d + \omega_e \psi_{df} \tag{3-4}$$

$$T_e = \frac{3}{2} P\left(\psi_{df} i_q + i_d i_q \left(L_d - L_q\right)\right) \tag{3-5}$$

The following limitations must be satisfied at any instant:

$$v_d^2 + v_q^2 \le V_{\max}^2 \tag{3-6}$$

$$i_d^2 + i_q^2 \le I_{\max}^2 \tag{3-7}$$

In (3-6), V_{max} is the maximal available amplitude of the fundamental phase voltage component at the inverter output. In (3-7), I_{max} is the maximal allowable phase current.

Since the drive is implemented with closed-loop current control, it is convenient to define an operating region in terms of its location in the (i_d, i_q)-plane. The current-limit constraint (3-7) forms a circle centered at the origin of this plane. From equations (3-3) and (3-4), it can be shown, [7], that the voltage-limit constraint (3-6), in general, defines an ellipse whose center is offset from the origin. The ellipse is defined by:

$$\left(\frac{V_{\max}^2}{\omega_e L_q}\right)^2 = i_q^2 + \left(\frac{L_d}{L_q}\right)^2\left(i_d + \frac{\psi_{df}}{L_d}\right)^2 \tag{3-8}$$

For a non-salient machine with $L_d=L_q$, such as a SMPMS machine, this expression reduces to a set of voltage-limit circles that are centered at $-\psi_{df}/L$, Fig. 3.2. The radii are directly proportional to V_{max} but inversely proportional to the rotor speed $\omega_r=\omega_e/P$, [2], [5], [8].

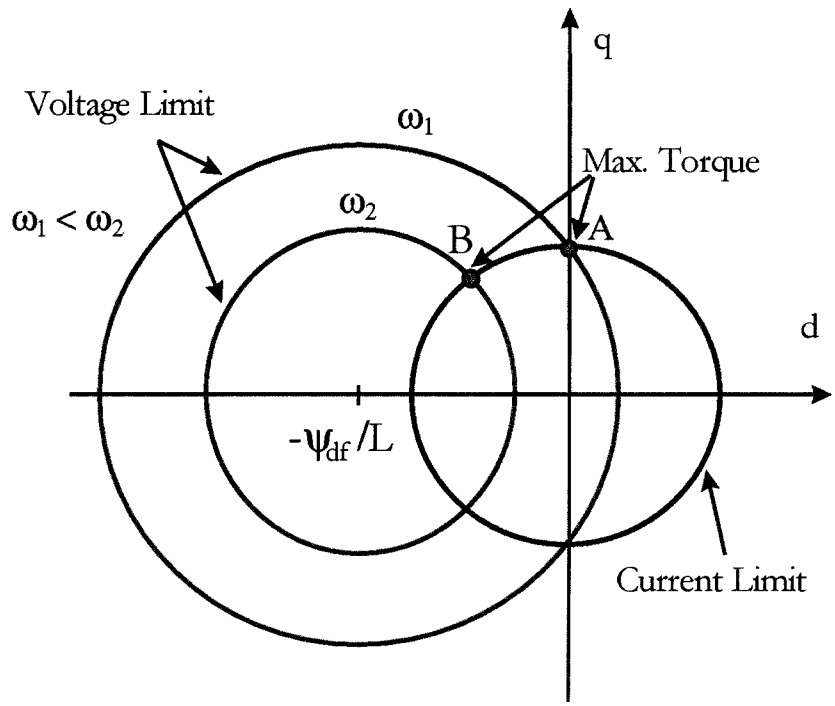

Fig. 3.2. Two voltage-limit circles and the current-limit circle for a SMPMS machine.

A given operating point will not exceed the voltage or current-limit constraints if it lies within the intersection of the voltage and current-limit circle.

It is essential to observe in Fig. 3.2 that the radius of the voltage-limit circle contracts as the speed increases, gradually narrowing the area of achievable steady-state operating points of the drive system. When the speed is low, the voltage-limit circle fully encompasses the current-limit circle, [3]. In this case, the drive can operate anywhere within the current-limit circle, which has a fixed diameter. As the speed approaches the base value, the voltage-limit circle shrinks. The current-limit disk is not completely encircled any more by the voltage-limit circumference. This has the effect of decreasing the maximal torque that can be attained by the machine as the rotor speed increases. Consequently, SMPMS control strategy at low speeds is chosen to maximize the *torque-per-ampere* ratio, i.e., i_d is set to zero if back EMF is smaller than V_{max}, [5], [6]. When the base speed is reached, $\omega_b = V_{max} / \psi_{df}$, the voltage-limit circle has already shrunk so that its perimeter passes through the origin of the (i_d , i_q)-plane. Now, the operation beyond this point is enabled by controlling the flow of the negative i_d current, which accordingly decreases the total flux in the machine air gap. Otherwise, if we held i_d at zero (as we do in the low-speed regime) in an attempt to maintain the maximal *torque-per-ampere* ratio, the voltage-limit circle would coerce i_q to plummet immediately to zero as the speed approaches the threshold value ω_b.

A necessary reference i_d^* for any achievable torque and at any speed can be determined from equations (3-3) – (3-7), as was done in [9]. If the effect of the stator resistance is neglected, $R=0$ in equations (3-3) and (3-4), and if the equality sign is used in equations (3-6) and (3-7), the maximum torque attainable and the corresponding reference i_d^* are obtained as presented in [5] and [6]:

$$T_{e\max} = \frac{3}{2} P \psi_{df} \sqrt{\frac{V_{\max}^2}{(\omega_e L)^2} - \frac{1}{4}\frac{\psi_{df}}{L}\left[1 + \frac{V_{\max}^2}{(\omega_e \psi_{df})^2} - \frac{(LI_{\max})^2}{\psi_{df}^2}\right]} \tag{3-9}$$

$$i_d^* = \frac{1}{2}\frac{L}{\psi_{df}}\left[\left(\frac{V_{\max}}{\omega_e L}\right)^2 - \left(\frac{\psi_{df}}{L}\right)^2 - I_{\max}^2\right] \tag{3-10}$$

The least complex approach to the flux weakening operation is to make a look-up table of the precalculated values for i_d^*, different torque levels and different states of charge of DC batteries that are used as the energy source. Such a table is quite cumbersome and requires new adjustments every time a machine with different parameters is employed. Even though the table can be improved, for example, by experimental data for the magnetization characteristics of the machine, the method is very sensitive to any changes or uncertainties related to the system parameters and variations in the operating conditions, e.g., temperature.

Two previously published flux weakening schemes, [5], [9], offered certain improvements because the schemes do not use machine parameters for any calculations in the flux weakening region. The method suggested in [5] offered good steady state operation, without steady state error present in [9], but was computationally more complex than [9] and required DC bus voltage sensing. The method presented in [9] brought some stability concerns, as mentioned in [2], and ineptly combined a *d-q* frame current control with a three phase hysteresis current control.

This chapter presents two modified and improved flux weakening schemes for SMPMS drives. The aforementioned problems of the earlier algorithms are eliminated. Then, two new schemes are compared regarding their steady state and transient performance.

Although these techniques were developed for SMPMS machine drives, there are no physical hurdles that would prevent their refitting for use in IPM machine drives. Because of the rotor saliency present in IPM machines, the d and q axes' inductances are not equal, $L_d \neq L_q$, and voltage-limit circles become voltage-limit ellipses, as previously noted. The main difference stems from the location of the PM's on the machine rotor. The IPM machines have a smaller effective air gap between stator and rotor than SMPMS since interior PM motors have their magnets buried inside the rotor, Figs. 2.1 and 2.2. As a result, IPM drives have traditionally been considered suitable for easy flux weakening operation with low levels of the weakening i_d current injection. Consequently, many research papers, describing various control algorithms, have been published for high-speed IPM machine drives, [7], [10] – [16]. However, IPM machines are significantly more expensive than their SMPMS counterparts. This makes SMPMS machines much more attractive for the industry.

From the discussion given above, it is apparent that the effectiveness of flux weakening control techniques in a practical drive system is helped by proper parameter design of all drive subsystems. Some examples of different possible approaches to the machine design, which exceed the scope of this work, were presented in [17] and [18] for EV applications, and in a more general manner in [19]. The inverter design, including both power and control stages, ought to be performed considering all regular operating regimes of the drive, as well as failure modes. The fault situations when an adequate closed-loop control is lost (for instance, a gate driver supply failure) impose a necessity for sizing the switching components and selecting protection circuitry. A loss of the flux weakening control at elevated speeds implies the appearance of very high values of back EMF across the inverter devices.

3.3. A SMPMS Flux Weakening Scheme Using Closed-Loop Reference Voltage Control

3.3.1. Algorithm Description

The general block diagram of the SMPMS drive with field-oriented control and flux weakening operation is shown in Fig. 2.8. In the closed-loop voltage scheme, the flux weakening mode is initiated as soon as the phase voltage magnitude reaches V_{max}. If the sine wave mode of the inverter modulation is used, then from [5]:

$$V_{\max} = \frac{1}{\sqrt{3}} V_{dc} \tag{3-11}$$

and for the full six-step operation, [6]:

$$V_{\max} = \frac{2}{\pi} V_{dc} \tag{3-12}$$

However, the actual measurement and knowledge of the DC bus voltage is not necessary. Equivalent phase voltages in the synchronous *d-q* reference frame can be represented as follows, [1], [5]:

$$v_d = \frac{2}{3} d_d V_{dc} \tag{3-13}$$

$$v_q = \frac{2}{3} d_q V_{dc} \tag{3-14}$$

where d_d and d_q are current regulator outputs, Fig. 2.8, that are bounded according to:

$$-1 \le d_d \le 1 \tag{3-15}$$

$$-1 \le d_q \le 1 \tag{3-16}$$

Then, the phase voltage magnitude can be expressed as:

$$V_{phase} = \sqrt{v_d^2 + v_q^2} = \frac{2}{3} V_{dc} d \tag{3-17}$$

where d is the phase voltage reference duty cycle or reference modulation index, defined as follows:

$$d = \sqrt{d_d^2 + d_q^2} \tag{3-18}$$

In this algorithm, d^2, the square of the reference duty cycle, is used as a feedback variable in the flux weakening section and compared to the square, d_m^2, of the onset modulation index. From (3-11) – (3-18), it follows that the boundaries of the sine wave and six-step regions are respectively:

$$d_{msw} = \frac{\sqrt{3}}{2}; \qquad d_{mss} = \frac{3}{\pi} \tag{3-19}$$

Therefore, the output values of the PI current controllers can be used to calculate the square of the reference modulation index d^2. This value is then used to calculate the error signal of the flux weakening structure:

$$\Delta_{fw} = d^2 - d_m^2 \tag{3-20}$$

The block-diagram of the flux weakening algorithm is given in Fig. 3.3. Clearly, the actual V_{dc} value is not needed for the flux adaptation. The error in (3-20) is processed by an additional PI controller in the flux weakening loop. To prevent serious deterioration of the machine characteristics by demagnetization of the rotor permanent magnets, the output of the PI regulator must be limited to the designed $-I_{dmax}$. This guarantees that the magnets will not be damaged. As previously emphasized, to achieve maximal torque production at low to moderate velocities, the upper limit ought to be set to zero.

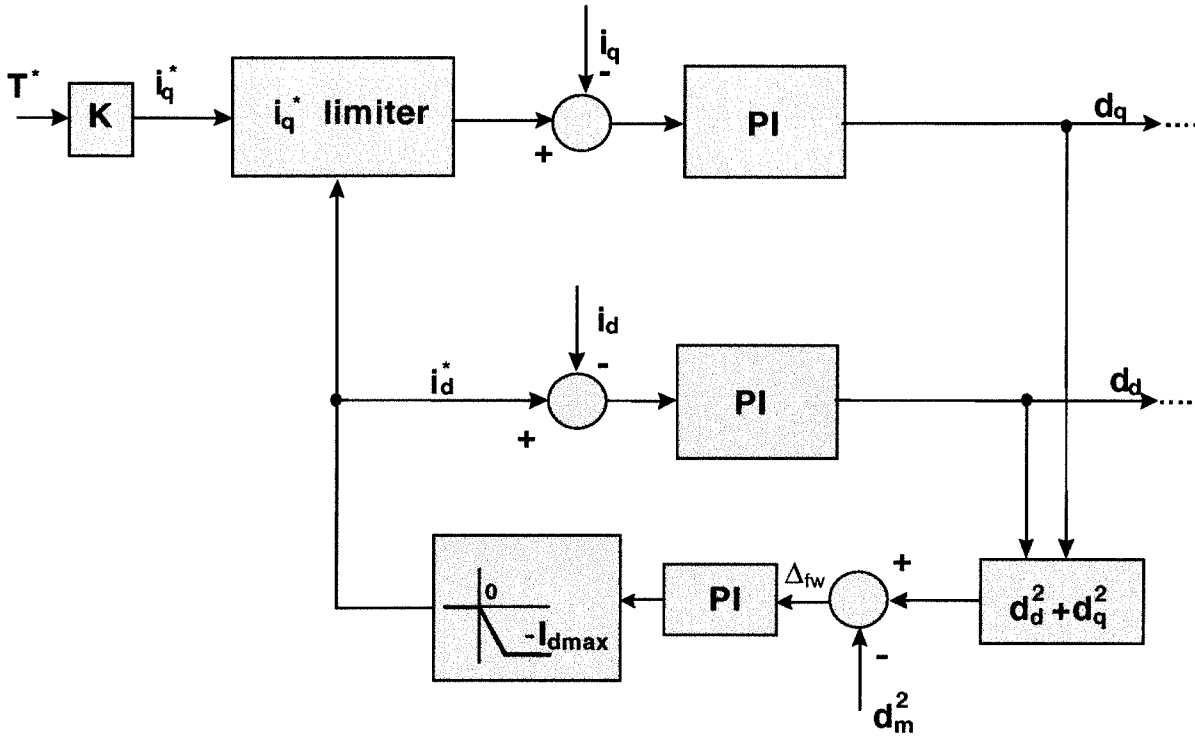

Fig. 3.3. A SMPMS flux weakening control scheme with closed-loop voltage control.

Here, T^* is the torque command. In our case, T^* is generated by the vehicle level control that processes the accelerator pedal or cruise control input signals.

The value of the on-set point d_m can be simply adjusted in software if necessary. This feature is especially useful, for instance, in cases when an outer controller in the system (e.g., at the vehicle control level) demands the disabling of the six-step mode. In EV's, this may take place when the battery voltage drops below a certain value but the vehicle level controller still requires and permits the flux weakening operation. In this example, d_m ought to take the value that corresponds to the boundary of the non-distorted sinusoidal mode of the SVM (i.e., d_m=*0.867*).

3.3.2. Design Guidelines for Practical Implementation

It was discussed in [6] that feed-forward compensation of the cross-coupling terms in (3-3) and (3-4) (the terms that include multiplication of speed with current) is typically used in practical drive implementations for the enhancement of the current control, regardless of the flux weakening scheme being employed, [1], [2], [20]. The SMPMS flux weakening scheme is, hence, modified for practical implementation so that the advantages of such compensation are utilized, Fig. 3.4. The compensation also offers an opportunity to design controller parameters using results from the linear systems control theory and still to accomplish excellent overall system performance.

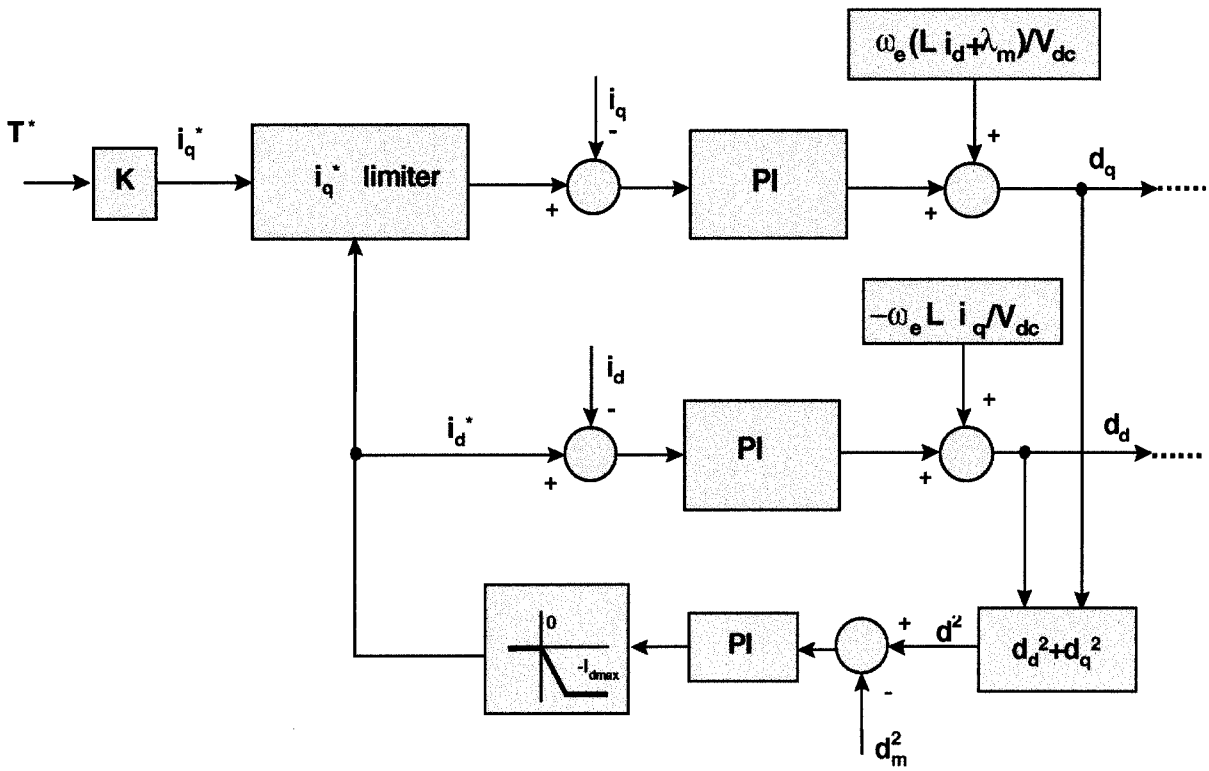

Fig. 3.4. The SMPMS voltage control flux weakening scheme modified for improved performance.

The design task requires that the proportional and integral gains of two PI current controllers and the gains for the flux weakening section are determined. When feed-forward terms are used, the voltage equations of the SMPMS machine reduce to:

$$v_d = Ri_d + L\frac{di_d}{dt} \tag{3-21}$$

$$v_q = Ri_q + L\frac{di_q}{dt} \tag{3-22}$$

where voltages and currents are given in their physical units. In the Laplace domain, these equations can be transformed to the following form:

$$\frac{i_d(s)}{v_d(s)} = \frac{i_q(s)}{v_q(s)} = \frac{1}{R + sL} \tag{3-23}$$

If the gain of the current sensors is K_A and if we use (3-13) and (3-14), we can write this as:

$$\frac{i_d(s)}{d_d(s)} = \frac{i_q(s)}{d_q(s)} = \frac{K_s}{R + sL} \tag{3-24}$$

Here, the currents are scaled with the sensor gain K_A; then, $K_s=2V_{dc}/3K_A$. Now, any method from control systems theory can be applied to design the current control. However, a relatively simple but very effective method is presented here. It includes PI controllers whose parameters are selected using compensation by left-half-plane (stable) pole-zero cancellation. In the Laplace domain, the PI controller transfer function is:

$$C_{PI}(s) = K_p + \frac{K_i}{s} \tag{3-25}$$

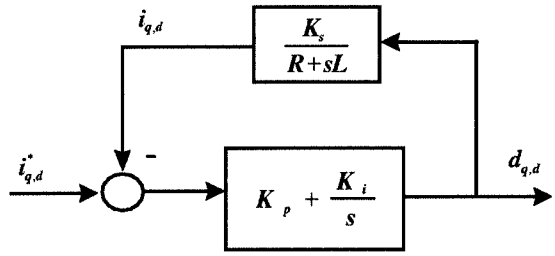

Fig. 3.5. Equivalent block-diagram for decoupled current control using proportional-integral law.

The equivalent block-diagram for the current control design is given in Fig. 3.5. The compensation implies that, ideally, the following relationship is satisfied:

$$s + \frac{K_i}{K_p} = s + \frac{R}{L} \tag{3-26}$$

and consequently:

$$\frac{K_i}{K_p} = \frac{R}{L} \tag{3-27}$$

After the compensation, the open and closed-loop current transfer functions become, according to Fig. 3.5 and using equations (3-24) – (3-27):

$$G_0(s) = K_p \frac{K_s}{sL} \tag{3-28}$$

$$G_C(s) = \frac{i_{d(q)}}{i^*_{d(q)}} = \frac{G_O(s)}{1+G_O(s)} = \frac{1}{1+\frac{s}{\omega_c}} \tag{3-29}$$

where $\omega_c = K_p K_s / L$ is the closed-loop bandwidth. Now, we choose the desired bandwidth first. This sets forth the value for K_p. Then, K_i is calculated from (3-27). In practice, the compensation (3-27) is achieved only approximately, but it still results in very good performance, when the feed-forward terms are used.

We notice here that the controller gains are simple functions of V_{dc}. As a result, the current control can be further improved by including, if necessary, a simple algorithm for the adaptation of the PI coefficients when the DC bus voltage varies.

Design of the PI controller in the flux weakening section is more convoluted because of an additional non-linearity that comes from the modulation index calculation:

$$f(d_d, d_q) = d^2 = d_d^2 + d_q^2 \tag{3-30}$$

At this point, we are interested in designing the parameters in such a way that the transfer function from the i_q^* to the output of the flux weakening section, i_d^*, provides an adequate response at elevated speeds.

From Fig. 3.5 and equations (3-24) – (3-28), it follows that the transfer function between the current command input and the duty cycle of the corresponding axis is:

$$G_V(s) = \frac{d_{d(q)}(s)}{i^*_{d(q)}(s)} = \frac{R}{K_s} \frac{1 + \frac{s}{R/L}}{1 + \frac{s}{\omega_c}} = K_M \frac{1 + \frac{s}{\omega_M}}{1 + \frac{s}{\omega_c}} \tag{3-31}$$

For the flux weakening loop design, we can now reduce the block-diagram shown in Fig. 3.4 to the structure given in Fig. 3.6.

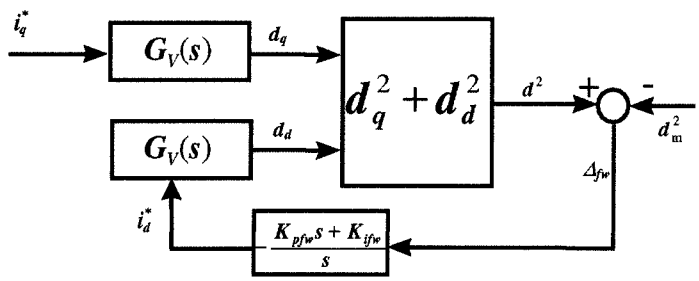

Fig. 3.6. Simplified block-diagram for the design of the flux weakening PI controller.

By observing that the flux weakening operation means that the square of the reference duty cycle d^2 stays close to d_m^2, the function can be linearized around the d_m point by retaining only the first-order terms in the Taylor expansion for $d^2=f(d_d,d_q)$. The linearization is performed around the midpoint of the possible range for d_d and d_q, when:

$$|d_{d0}| = |d_{q0}| = \frac{d_m}{\sqrt{2}} \tag{3-32}$$

Then, keeping only the first order terms in the expansion, we have:

$$f(d_d, d_q) \approx f(d_{d0}, d_{q0}) + \frac{\partial f(d_{d0}, d_{q0})}{\partial d_d}\Delta d_d + \frac{\partial f(d_{d0}, d_{q0})}{\partial d_q}\Delta d_q \tag{3-33}$$

$$f(d_d, d_q) \approx f(d_{d0}, d_{q0}) + 2d_{d0}(d_d - d_{d0}) + 2d_{q0}(d_q - d_{q0}) \tag{3-34}$$

And, finally, this results in:

$$f(d_d, d_q) \approx 2d_{d0}d_d + 2d_{q0}d_q - f(d_{d0}, d_{q0}) \tag{3-35}$$

We know that $f(d_{d0},d_{q0})=d_m^2=(3/\pi)^2$ when the six-step mode is utilized. Now, if we use $K_0=|d_{d0}|$, we obtain:

$$\frac{i_d^*}{i_q^*} = \frac{G_{FW0}(s)}{1+G_{FW0}(s)} \tag{3-36}$$

where G_{FW0} is:

$$G_{FW0}(s) = K_0 G_V(s)\frac{K_{pfw}s + K_{ifw}}{s} = K_0 K_M K_{ifw} \cdot \frac{1+\frac{s}{\omega_M}}{1+\frac{s}{\omega_c}} \cdot \frac{1+\frac{s}{K_{ifw}/K_{pfw}}}{s} \tag{3-37}$$

If we again apply the compensation so that $K_{ifw}/K_{pfw}=\omega_c$, and if we introduce $K_{FW}=K_0K_MK_{ifw}$, the equation (3-37) becomes:

$$G_{FW0} = K_{FW}\frac{1+\frac{s}{\omega_M}}{s} \tag{3-38}$$

The next step is to choose K_{FW}, i.e., K_{ifw} so that the flux weakening response is optimized. Here, it is important to bear in mind that a very high increase of K_{FW} is limited by the presence of the limiter in the flux weakening section, Fig. 3.4. Once K_{ifw} is determined, the proportional gain is then: $K_{pfw}= K_{ifw}/\omega_c$.

Using the flux weakening region implies the use of all, or almost all, of the available inverter voltage. Since the current regulators command the inverter voltage, the capability of these regulators to utilize the voltage and their behavior under voltage constraints is very important. When a linear regulator operates in saturation, it becomes, actually, a nonlinear system. Two desired conditions are, first, keeping the saturation level at the output as long as possible so that the settling time is minimized and, second, once the regulator exits saturation, it ought to act again as the linear regulator with the same performance as before, [21]. Therefore, a proper anti-windup scheme needs to be implemented. This issue was addressed in detail in [21] – [25]. Also, instead of a PI structure, an equivalent pseudo-differential feedback (PDF) regulator can be used, [26], to improve the disturbance rejection, if necessary.

The aforementioned approach gives a good estimate for the controller parameters in the flux weakening loop. The values are used for the full simulation model of the SMPMS machine drive, as described in Chapter 2. The simulation model offers a possibility to observe the flux weakening operation and slightly adjust the parameters as needed.

3.3.3. Simulation

The simulation model included all drive segments described in Chapter 2 and the flux weakening scheme from Fig. 3.4. Also, the simulation model accounted for a simple first-order, low-pass filter for the high frequency noise rejection in the flux weakening section. This yields:

$$G_{FW0} = K_{FW} \frac{1 + \frac{s}{\omega_M}}{s\left(1 + \frac{s}{\omega_{LP}}\right)} \tag{3-39}$$

The simulation covered a rapid acceleration with maximum torque produced by the SMPMS machine. Normalization was performed so that the corresponding maximum torque current component is $i_q^*=0.8$ p.u. The load torque was constant. When the maximum speed was reached, $\omega_{max}=1$ p.u, a deceleration to $\omega=0.22$ p.u. was required. The necessary braking current was $i_q^*=-0.16$ p.u. Once this speed was reached, the torque was adjusted to match the load demand, $i_q^*=0.18$ p.u, so that a steady state operation was achieved. The DC bus voltage was 250 V, the minimal allowable operating voltage for the drive prototype. The results of this simulation are summarized in Fig. 3.7. The time scale is not normalized.

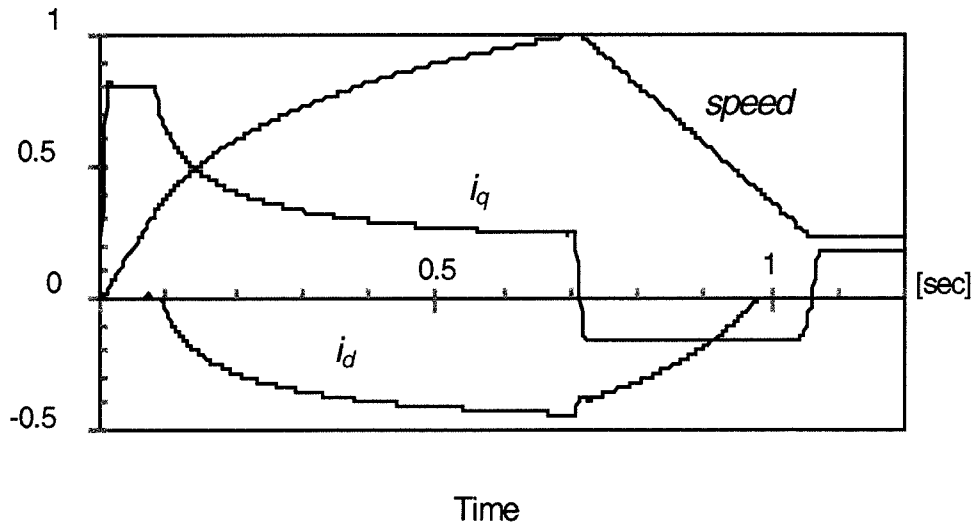

Fig. 3.7. Simulation results with flux weakening scheme employing closed-loop output voltage control.

The simulation results in Fig. 3.7 verify that the scheme is fully operational and that it provides the expected operation over the desired speed range. When the flux weakening is initiated and negative i_d injected, we can see that the maximal achievable i_q decreases because the total current is subject of the current limit from equation (3-7). The flux weakening is started as soon as the six-step mode is reached, as shown in Fig. 3.8.

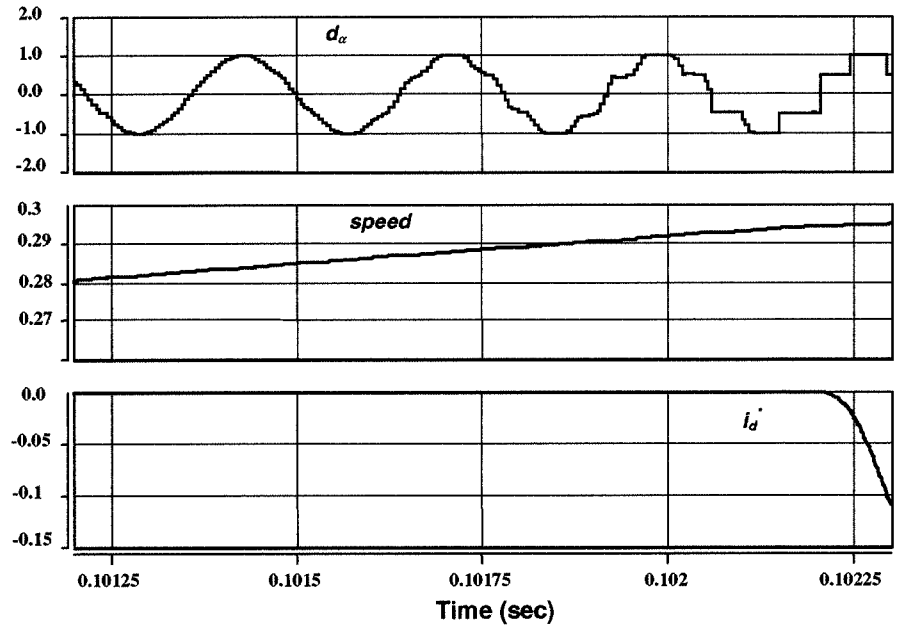

Fig. 3.8. Entrance into flux weakening.

A very important concern for the evaluation of the control performance is the transient response to torque step command. The next simulation was done at a constant speed of *0.7* p.u., i.e., deep in the flux weakening region. The torque component current reference changed from *0* to *0.2* p.u., with a slew rate of *50* p.u./sec, Fig. 3.9. The transition into six-step was disabled, i.e., d_m set to *0.867*, in order to observe i_q and i_d transient responses in a clear manner. Namely, in the over-modulation and six-step modes, these current components contain the sixth harmonic, which is discussed in detail in the next chapter.

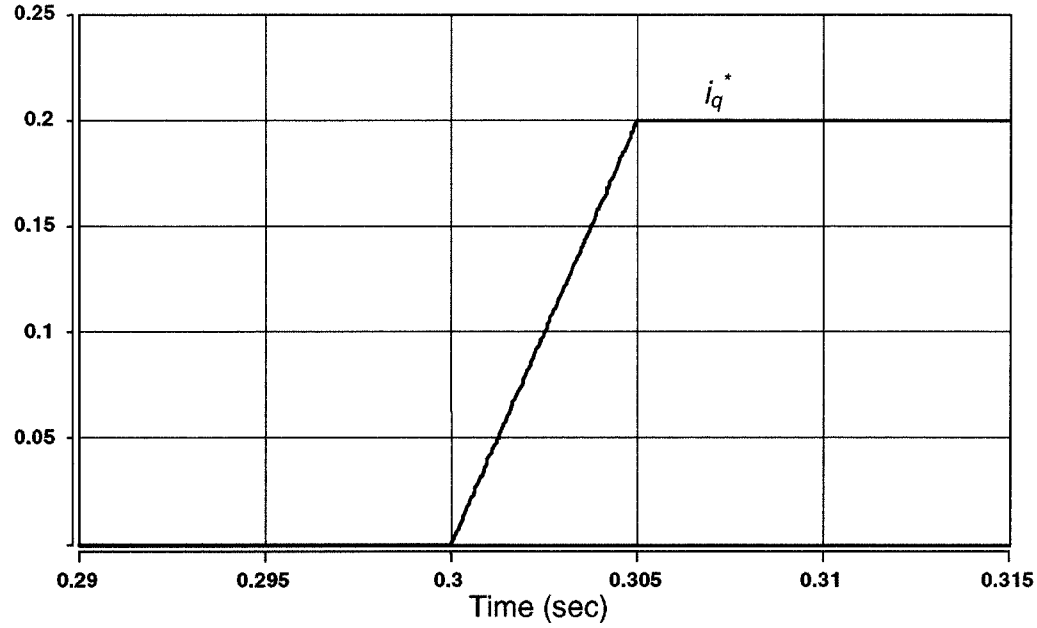

Fig. 3.9. The current reference corresponding to the torque step command.

The time domain responses are shown in Fig. 3.10. A certain delay in i_d response can be observed and an overshoot in i_q is noticeable. An attempt to decrease the i_q overshoot results in a larger i_d delay, i.e., a trade-off between these two characteristics must be made in a real drive system.

We notice that the settling time is also relatively long compared to the time duration of the reference transient, Fig. 3.9, and it is equal to approximately five times the rise time. This response is also illustrated in Fig. 3.11, where i_q versus i_d trajectory is presented in the *d-q* plane. There, we can clearly see that the i_q overshoot is almost *20%*. This imposes some qualitative limitations in electrical drives in which this scheme is utilized and a rapid transient response of the torque control loop is demanded.

The simulation results provided a very thorough insight into the merits of the scheme and highlighted features that may require additional attention in some applications.

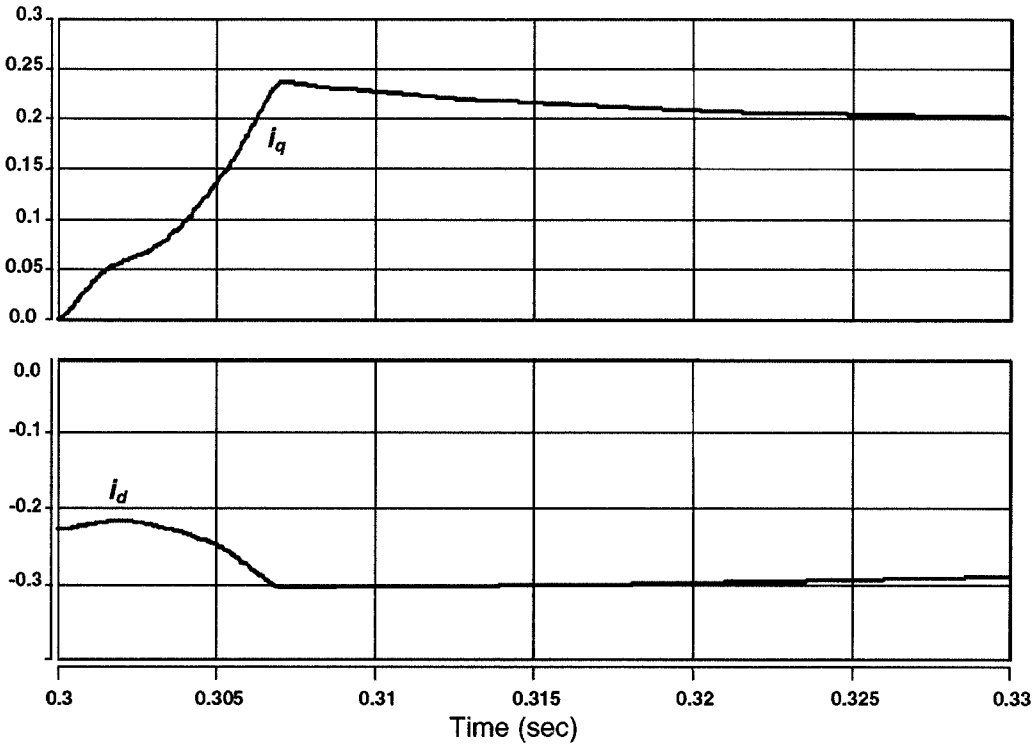

Fig. 3.10. i_q and i_d transient responses to the torque step command.

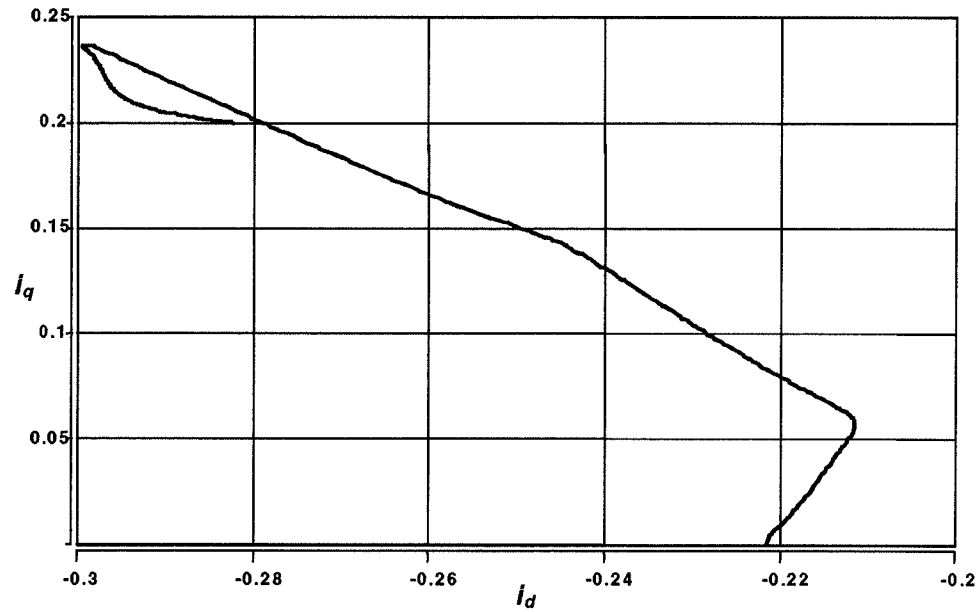

Fig. 3.11. Transient i_q versus i_d trajectory in the *d-q* plane.

3.4. A SMPMS Flux Weakening Scheme Using i_q Error Detection

3.4.1. Algorithm Description

The field-oriented control is implemented in a synchronous reference frame, as shown in Fig. 2.8, using fast PI current controllers. Therefore, there is no steady-state error in the current regulation at low-to-moderate velocities. However, as the voltage-limit from equation (3.6) is approached and when the PI controllers verge upon saturation, the available voltage margin (necessary for the i_q current) becomes narrower and the i_q error appears. Consequently, the value of this error can be used as a condition to initiate the flux weakening operation. The error is compared with a predetermined threshold value. Once the threshold is crossed, an appropriate reference i_d^* is generated. The i_d^* is, then, proportional to the filtered $|i_q^{err}|$ signal, Fig. 3.12.

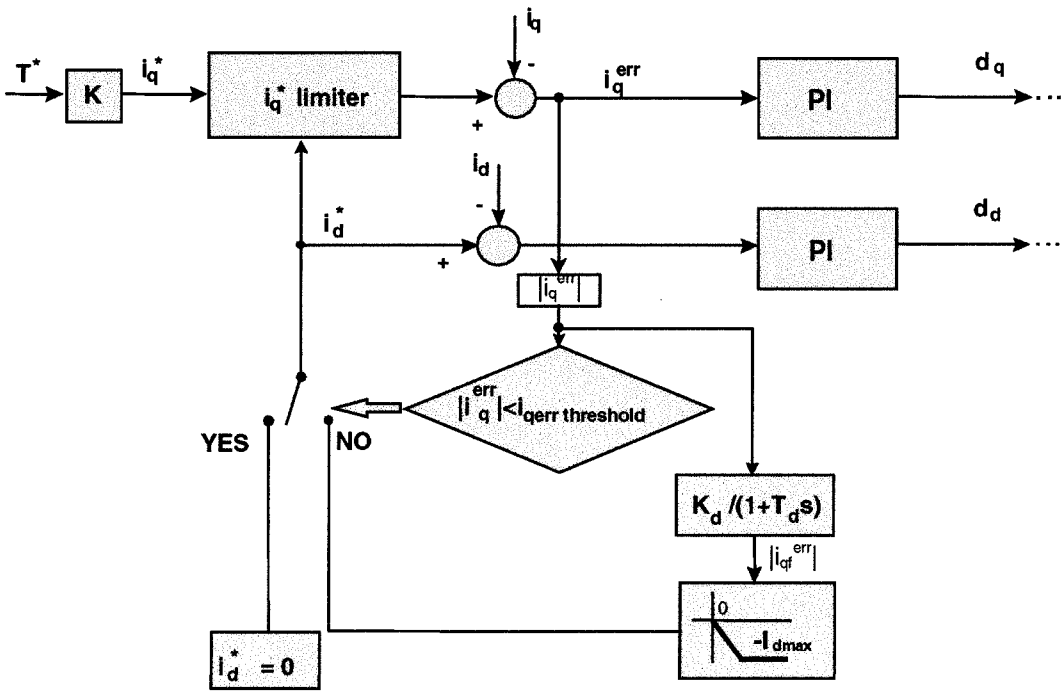

Fig. 3.12. A SMPMS flux weakening control scheme with i_q^{err} detection.

A simple first-order, low-pass filter is used to prevent unnecessary i_d injection due to the high frequency noise and to regulate the rate of injection during transients when a step change in the torque reference is received. However, since the threshold condition is present in the flux weakening section, a steady state i_q error is inevitable at high speeds. This intrinsic error can be minimized by an appropriate selection of the K_d constant. The error is not important in drive systems where outer control loops are closed. This is the case in velocity control systems, e.g., in automotive applications this corresponds to the cruise control being activated at the superimposed vehicle control level.

Therefore, in torque control systems where an exact tracking of the torque reference is desired, the previously discussed scheme with the closed-loop reference voltage control provides advantageous steady state performance without steady state error, whereas the current error detection scheme offers reduced computational complexity. Also, it will be shown in the forthcoming discussion that the error detection scheme has better transient response characteristics than the reference voltage control technique [28].

3.4.2. Design Considerations for Practical Implementation

As discussed in section 3.3.2, feed-forward compensation of the cross-coupling terms in equations (3-3) and (3-4) is used for the performance enhancement of the current control loops. Therefore, practical implementation should use the block-diagram given in Fig. 3.13. The threshold value needs to be low, but it must be at least two times higher than the minimum resolution of the current sensors used in the system. The threshold condition ought to be realized with a hysteresis condition so that the oscillations around the boundary are prevented. When the error is used for the improved transient performance only [27], the sign of the rotor speed should be included. Namely, if $(i_q^* - i_q)\,sgn\omega_e > 0$, the current regulation

lacks the control voltage margin. On the other hand, when $(i_q^*-i_q)sgn\omega_e<0$, the back EMF assists the current regulation. Therefore, in such a case $K_d=Ksgn\omega_e$, where K is a positive constant. Here, for the flux weakening, we just use the absolute value of the error signal [28].

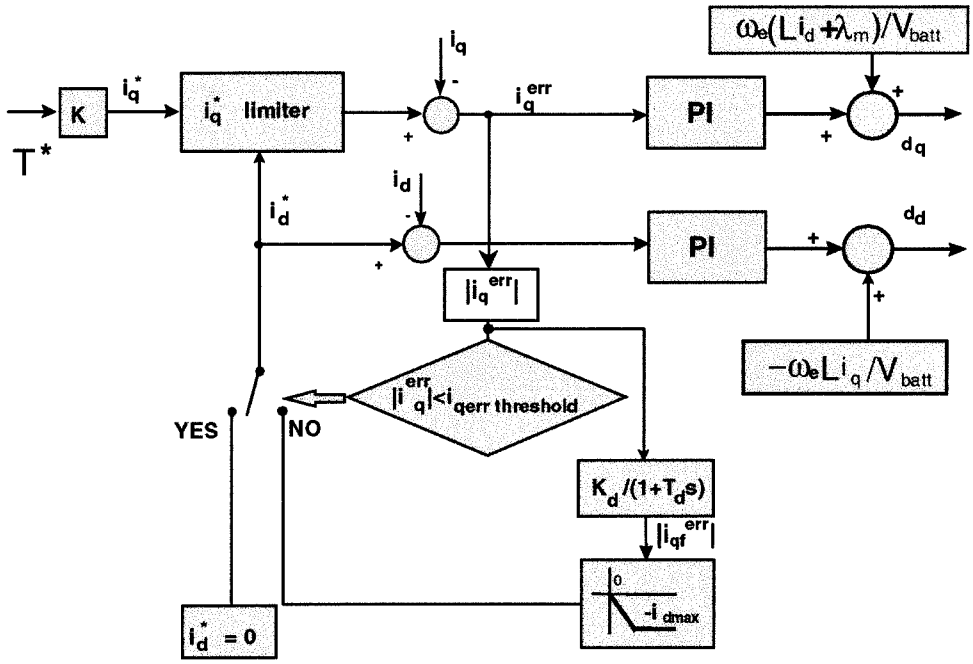

Fig. 3.13. The SMPMS flux weakening control scheme with i_q^{err} detection and decoupled current control.

When the decoupling method is used, by analogy with the previous case, we see that the current regulation satisfies the equation (3-29). Then, the i_q sensitivity transfer function is:

$$\frac{i_q^{err}}{i_q^*}=\frac{\dfrac{s}{\omega_c}}{1+\dfrac{s}{\omega_c}} \tag{3.40}$$

and, when the flux weakening is initiated, the transient behavior is described by:

$$\frac{i_d^*}{i_q^*}=K_d\frac{\dfrac{s}{\omega_c}}{\left(1+\dfrac{s}{\omega_c}\right)(1+sT_d)} \tag{3.41}$$

This equation shows that a fast transient response can be expected. Compared with the previous scheme, the time constant T_d corresponds to T_{LP}.

This scheme is used for the simulation model. The model gives us a possibility to observe the performance of the flux weakening technique and to modify the loop parameters, if necessary.

3.4.3. Simulation

The simulation model accounted for all drive subsystems delineated in Chapter 2, as well as for the algorithm in Fig. 3.13. The simulation covered a rapid acceleration with maximal torque applied to the drive shaft. The load torque, battery voltage, the normalization of the physical units, as well as the sequence of changes in the torque command, were the same as described in section 3.3.3. The results are summarized in Fig. 3.14. The simulation results verify that the technique is fully operational and that it ensures a stable operation over the entire speed range.

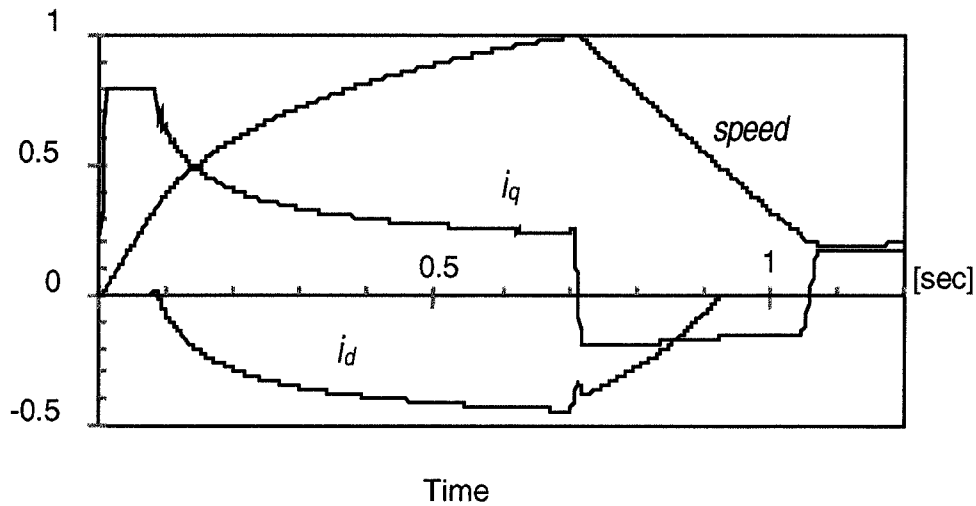

Fig. 3.14. Simulation results for the flux weakening scheme employing an i_q error-detection algorithm.

In comparison with the first scheme, we can observe the presence of current error in the q axis. However, we also notice that the error is speed dependent. Namely, during braking, following the moment when the maximum speed is reached, we see that i_q gets closer to desired $i_q^*=-0.16$ p.u. as the speed decreases. This effect is related to the decrease of the back EMF with the decrease in speed. Particularly, the speed decrease implies a reduction in the absolute value of injected i_d, i.e., a decrease of the flux weakening component that is responsible for providing the necessary voltage margin for torque producing component i_q.

The flux weakening was initiated as soon as the six-step mode had begun, as shown in Fig. 3.15. Again, the duty cycle d_α is directly proportional to the phase voltage v_a, and speed and current reference are given in per-unit values.

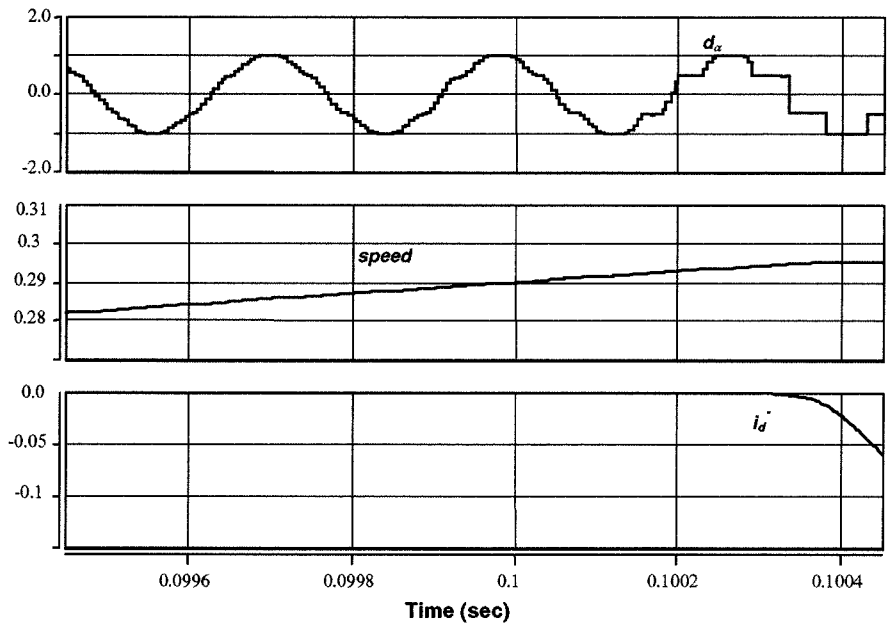

Fig. 3.15. Entrance into flux weakening.

As it was mentioned for the previous scheme, it is very important to evaluate the transient response to a torque step command. Therefore, a similar simulation test was repeated for this technique too. The speed, the torque reference (Fig. 3.9), the slew rate, and the SVM mode were set to be the same as in the case of the voltage reference algorithm. The time domain responses are shown in Fig. 3.16.

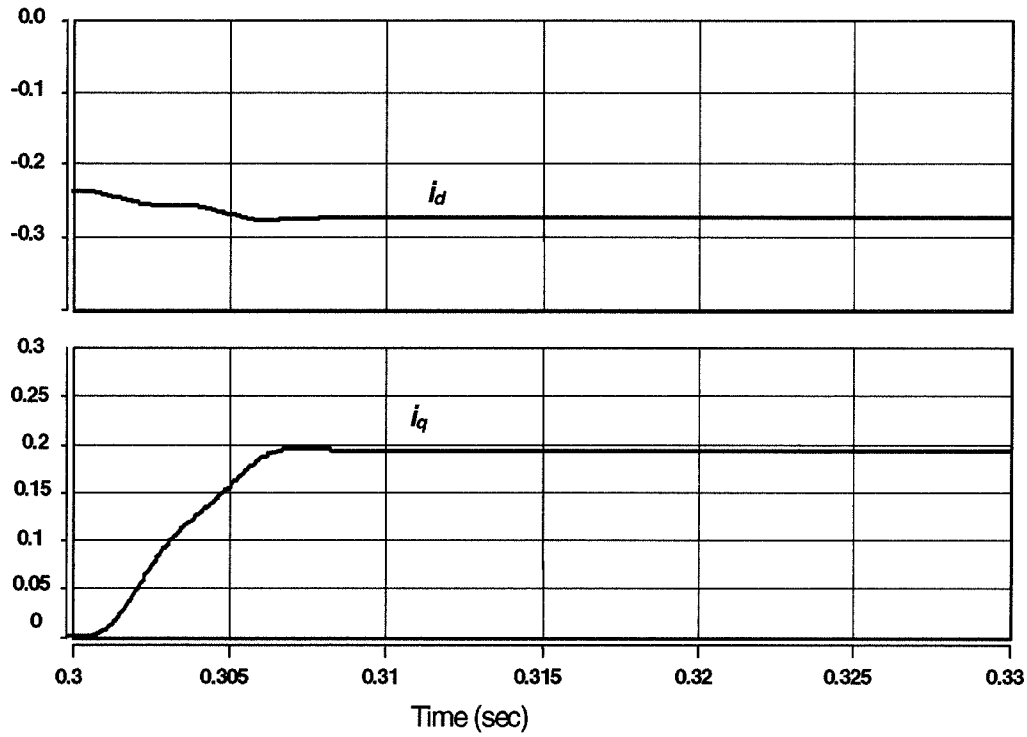

Fig. 3.16. i_q and i_d transient responses to the torque step command.

The transient response is significantly better than the equivalent response of the previous scheme. The problems associated with the i_d delay and the overshoot in i_q are not present. The corresponding settling time is much shorter here.

This response is also presented in Fig. 3.17, where i_q versus i_d trajectory is given in the *d-q* plane. There is no i_q overshoot, but a small error in the *q* axis can be observed at the

end of the transient. The trajectory is shorter than the one presented in Fig. 3.11.

The simulation data supplied important insights for a general comparison of the two algorithms. The results proved the viability of the schemes and provided necessary information for the evaluation of their steady state and transient performance [28]. The closed-loop control of the voltage reference ensures optimal steady state characteristics and can be utilized in applications where a rapid transient response is not a critical feature [6]. On the other hand, the i_q error scheme provides a superior transient behavior, but at the expense of certain steady state torque error and somewhat lower efficiency [6], [28]. Therefore, the latter method can be used in velocity control systems (when the torque loop is an inner loop) or in systems that demand a rapid transient response, when a scheme for compensation of the torque non-linearity must be incorporated.

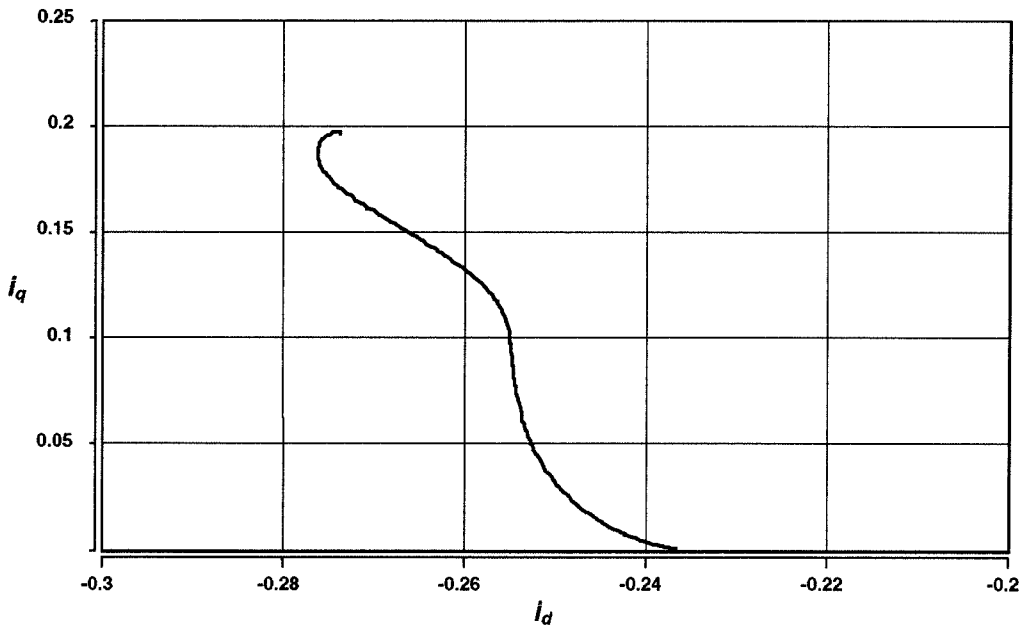

Fig. 3.16. Transient i_q vs. i_d trajectory in the *d-q* plane.

3.5. Experiments

The first scheme has been implemented in the assembly language of a low-cost, fixed-point, 16-bit digital signal processor, *Analog Devices ADSP2181*. The voltage reference control scheme was chosen for the main drive of the electric vehicle because of its advantageous torque linearity behavior and somewhat less demanding transient response requirements related to this application. The second, i_q error scheme is being considered for possible use in an auxiliary drive for hybrid vehicles, where a significantly faster transient performance is required.

An IGBT-based, three phase, full-bridge inverter (made by General Motors Advanced Technology Vehicles for use in the second-generation EV1 cars) was used as a power stage that interfaces a DC source with a SMPMS machine. The technical details were provided in Chapter 2. The machine parameters are given in Table 2.3.

Figs. 3.17 and 3.18 show how i_d adapts to the changes in speed for two values of the DC bus voltage, 250V and 350V.

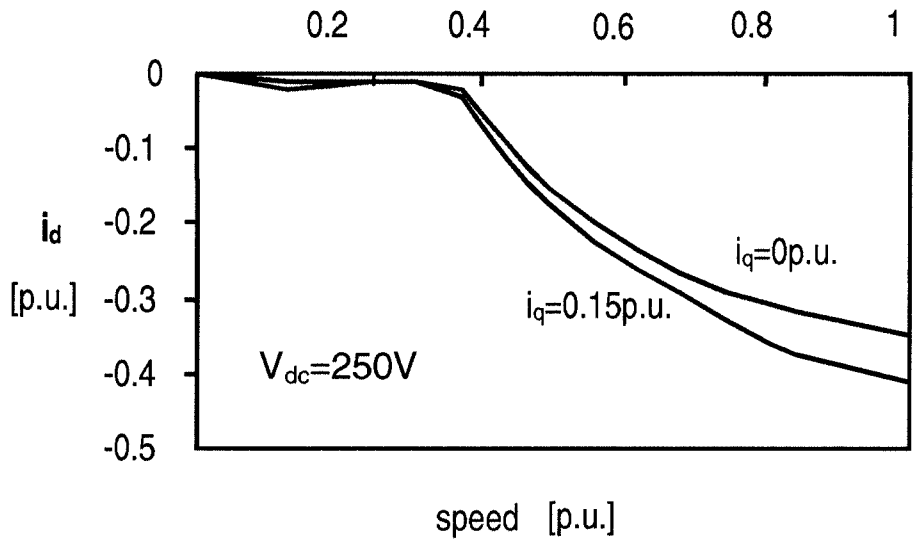

Fig. 3.17. i_d versus *speed* at $250V_{dc}$.

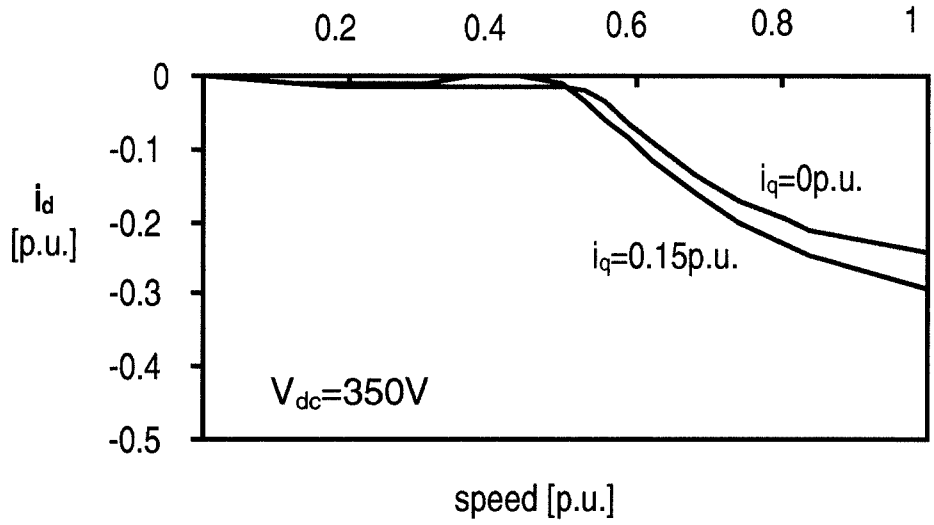

Fig. 3.18. i_d versus *speed* at $350V_{dc}$.

The experiments were performed at no load ($i_q^*=0$) on the shaft, as well as with the load ($i_q^*=0.15$ p.u.) that corresponds to the maximal torque achievable at the maximum speed when $V_{dc}=250$V. As predicted, there is an automatic adaptation of the i_d current that supplies the necessary voltage margin for any load and DC bus voltage, regardless of the values of drive parameters at the given conditions in the system environment.

The lower the DC bus voltage is, the earlier the flux weakening is initiated because of the conformably reduced diameter of the voltage limit circle at the base speed, Fig. 3.2. The absolute value of i_d increases with the decrease of DC bus voltage and/or increase of the load torque, as we can observe in Figs. 3.17 and 3.18. A higher voltage margin has to be provided (at the same speed) by the flux weakening control when the voltage available is lower and/or more torque has to be provided. Consequently, the back EMF has to stay at acceptable values at all operating points in the flux weakening region.

Fig. 3.19 shows the adjustments of the inverter output voltage with the speed for two different values of the mechanical load. Again, the results for 250V and 350V on the DC bus are shown.

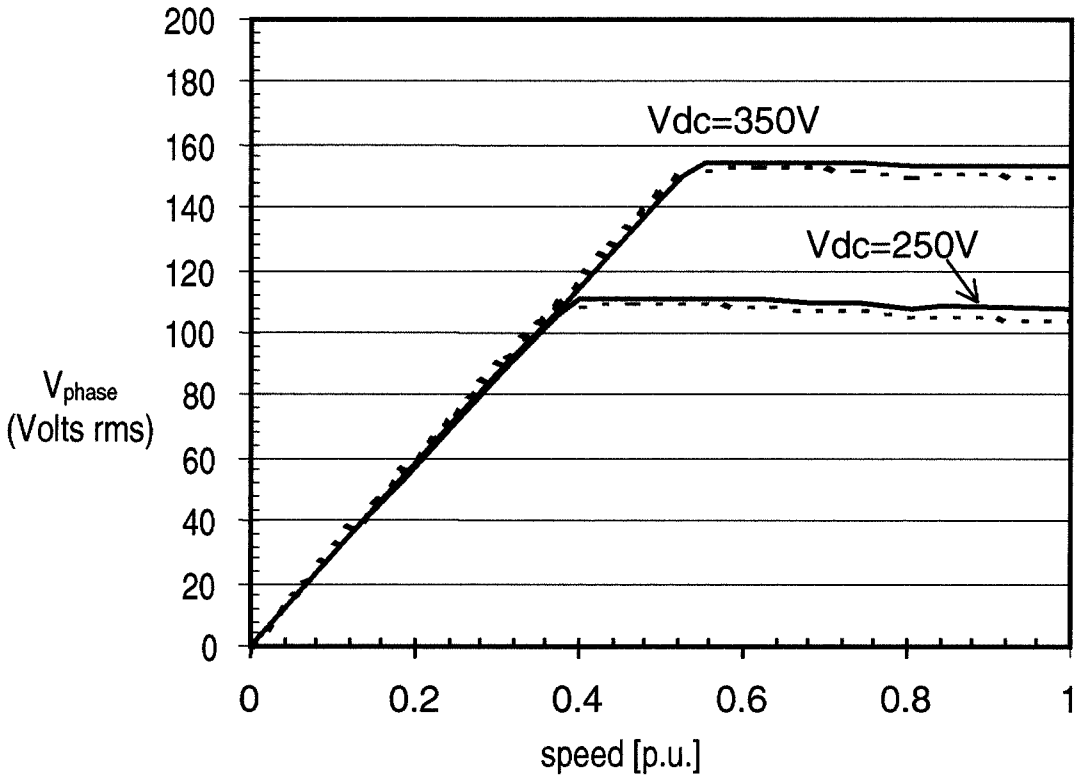

Fig. 3.19. Phase voltage (rms) at the inverter output (i_q=*0*: solid lines, i_q=*0.15*p.u: dashed lines).

We notice that the higher the DC bus voltage – the higher the inverter output voltage. This figure also confirms the maximal DC bus voltage utilization related to SVM with over-modulation and six-step modes [29]. Before the voltage limit is reached, the inverter has to provide higher voltage when the load (i.e., i_q current) is present, at the same speed, than in the case of no load operation. Once the voltage limit is reached, the voltage drop increases when the load and the i_q are present.

To verify that the drive prototype satisfies the *torque versus speed* requirement, we measured the characteristics at 250V and 350V at the DC bus. These curves are given in Fig. 3.20. For the more critical case, 250V, the simulation result is also included.

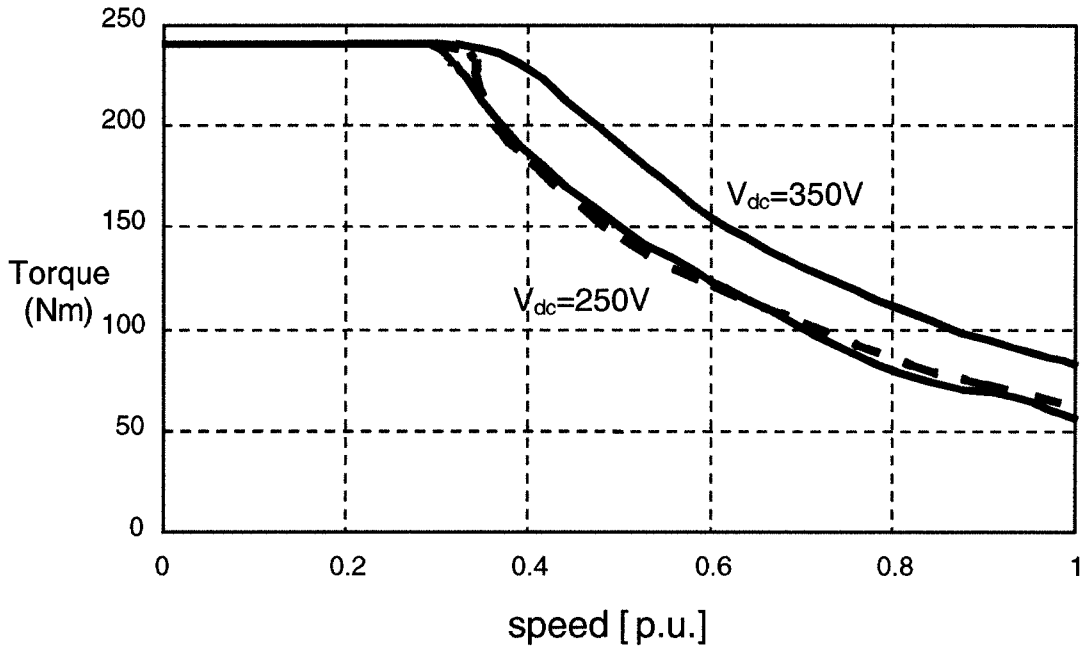

Fig. 3.20. Torque versus speed: experiment (solid lines) at 250V and 350V DC bus and simulation (dashed line) at 250V.

The wide range of the flux weakening operation is achieved. These characteristics satisfy the drive requirements for electric propulsion systems. Even though the results shown are for one quadrant of the torque-speed plane, the control scheme is independent of the direction of rotation and the mode of machine operation (motoring or regeneration). In the constant power region, we see that the higher power can be obtained when more voltage is available because the current limitations are unchanged.

We observe that the simulation result closely matches the experimentally measured characteristic. A slight discrepancy can be accounted for the non-modeled losses that are present in the experimental setup.

Fig. 3.21 illustrates how the current components adjust when the torque step command (with the predetermined slew-rate) is received from the vehicle level control, while the rotor speed is kept constant. The torque component i_q closely follows the shape of the torque command according to the equation 2-11. The flux weakening component i_d adapts to the value to afford the voltage needed for the increased i_q current demand. Namely, when a new value of the reference i_q^* is received, the error signal in the current regulation changes the input to the PI current regulator. As a result, the flux weakening section adapts the reference i_d^* so that the error signals of the current control are reduced to zero in the steady state that follows the transient.

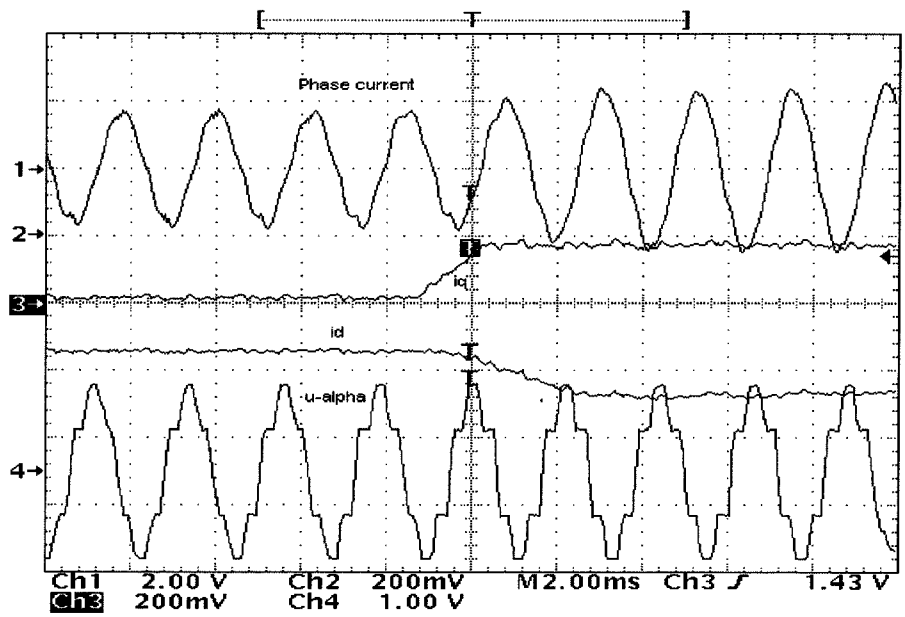

Fig. 3. 21. Transient response following the torque step command.

Since both current components change, we notice the change in the magnitude and phase of the total stator current. Fig. 3.21 also shows the u_α, the stationary frame α component of the inverter output voltage [1]. This voltage is directly proportional to the inverter phase *a* voltage. It illustrates the employed PWM strategy for the maximum DC voltage utilization.

It is apparent that the good transient shape of i_q is accomplished at the expense of a somewhat sluggish i_d response, as discussed in section 3.3.3. It was previously mentioned that the slower i_d response was not critical in this application. However, the i_q current error scheme ought to be considered for applications when a faster transient performance of the flux adaptation is needed.

The experimental efficiency comparison confirms the expected system efficiency advantage of the SMPMS drive over the previously used induction machine (IM) drive, Fig. 3.22. Power and speed points were chosen according to the GM vehicle integration requirements. The system efficiency is the efficiency of the entire system, including the inverter and the machine. The SMPMS drive system efficiency begins deteriorating when the flux weakening operation is initiated due to negative i_d current injection. We noticed a significant advantage in the SMPMS drive over 75% of the total speed range. The efficiencies of two systems become comparable after approximately 7/8 of the range. The highest difference in efficiency between two systems occurs right before the SMPMS enters the flux weakening region. The SMPMS drive efficiency was between 84.5% and 94.2%, whereas the IM drive efficiency was between 72% and 87% for the set of GM road loads.

In electric propulsion applications, any increase in the system efficiency reflects directly in an extension of the vehicle mileage range per battery charge. Having this objective

in mind, the SMPMS drive offered substantial improvements, when compared with the equivalent, previously used IM drive.

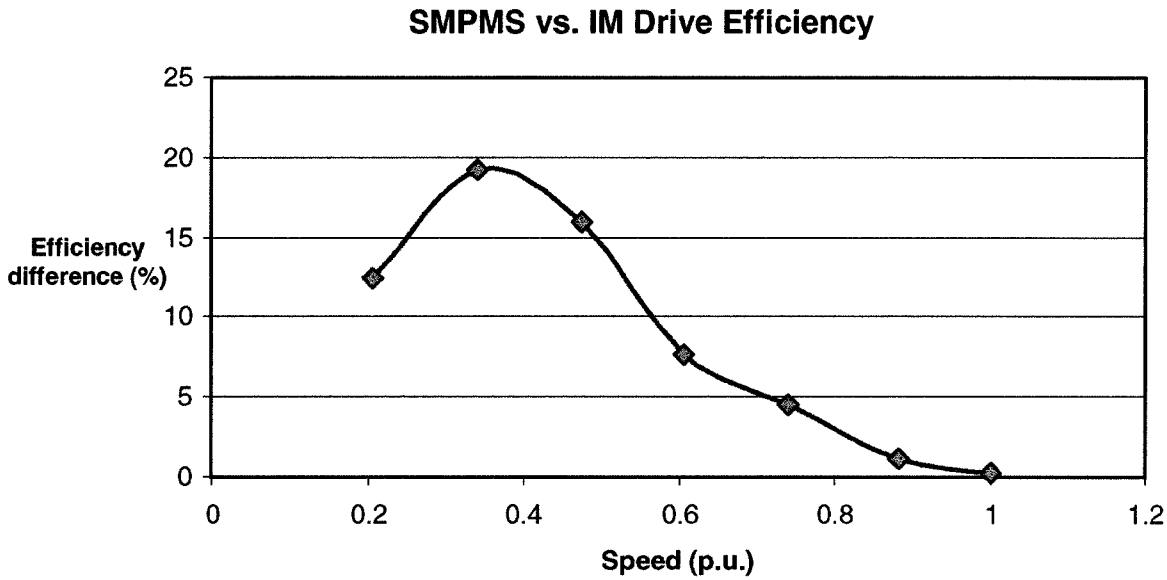

Fig. 3.22. The difference in efficiencies of SMPMS and IM drives over the full speed range (experiment).

3.6. Concluding Remarks

Two advanced flux weakening schemes were presented in this chapter. Both schemes ensure a wide range of constant power operation above the machine base speed. The entrance point for the flux weakening operation and further adaptation of the machine flux are automatically achieved regardless of the DC bus voltage, temperature or load. No DC voltage measurement is necessary. Steady state and transient behavior were compared and the parameter selection guidelines suggested.

The voltage reference control scheme renders advantageous steady state performance, whereas the i_q error method is less computationally demanding and offers a faster transient response. Therefore, the choice of the flux weakening control technique should be made depending on the drive requirements in particular applications.

The achieved speed range in the flux weakening region exceeds all results reported earlier for SMPMS drives. The only maximum speed limitation for the solutions proposed here comes from the machine mechanical characteristics.

The efficiency comparison of the SMPMS drive with an IM drive confirms the advantage of PM drives for applications where this property is critically important, like in autonomous electric vehicles.

References

[1] D. W. Novotny and T. A. Lipo, "Vector Control and Dynamics of AC Drives," Calderon Press • Oxford, 1996.

[2] B. K. Bose (editor), "Power Electronics and Variable Frequency Drives – Technology and Applications," IEEE Press, 1997.

[3] W. L. Soong and T. J. E. Miller, "Field-Weakening Performance of Brushless Synchronous AC Motor Drives," *IEE Proc.-Electr. Power Appl.*, vol. 141, no. 6, pp. 331-340, November 1994.

[4] B. Multon, J. Lucidarme et L. Prévond, "Analyse des possibilités de fonctionnement en régime de désexcitation des moteurs à aimants permanents," *Journal de Physique III*, 5, pp. 623-640, France, 1995.

[5] J. H. Song, J. M. Kim, and S. K. Sul, "A New Robust SPMSM Control to Parameter Variations in Flux Weakening Region," *In Proc. IEEE IECON'96 Conf.*, pp. 1193-1198, 1996.

[6] D. S. Marić, S. Hiti, C. C. Stancu, and J. M. Nagashima, "Two Improved Flux Weakening Schemes for Surface-Mounted Permanent-Magnet Synchronous Machine Drives Employing Space Vector Modulation," *In Proc. of IEEE IECON'98 Conference*, vol. 1, pp. 509-513, September 1998.

[7] T. M. Jahns, "Flux-Weakening Regime Operation of an Interior Permanent-Magnet Synchronous Motor Drive," *IEEE Trans. on Industry Applications*, vol. 23, no. 4, pp. 681-689, July/August 1987.

[8] D. S. Marić, S. Hiti, C. C. Stancu, J. M. Nagashima, and D. B. Rutledge, "Robust Flux Weakening Scheme for Surface-Mounted Permanent-Magnet Synchronous Drives

Employing an Adaptive Lattice-Structure Filter," *In Proc. of IEEE APEC99 Conference*, pp. 271-276, March 1999.

[9] S. D. Sudhoff, K. A. Corzine, and H. J. Hegner, "A Flux-Weakening Strategy for Current-Regulated Surface-Mounted Permanent-Magnet Machine Drives," *IEEE Trans. on Energy Conversion*, vol. 10, no. 3, pp. 431-437, September 1995.

[10]S. Morimoto, T. Ueno, M. Sanada, Y. Takeda, and T. Hirasa, "Variable Speed Drive System of Interior Permanent Magnet Synchronous Motors for Constant Power Operation," *In Proc. of IEEE PCC-Yokohama*, pp. 402-407, 1993

[11]B. Sneyers, D. W. Novotny, and T. A. Lipo, "Field-Weakening in Buried Permanent Magnet AC Motor Drives," *IEEE Trans. on Industry Applications*, vol. 21, pp. 398-407, March/April 1985.

[12]B. K. Bose, "A High-performance Inverter-Fed Drive System of an Interior Permanent Magnet Synchronous Machine," *IEEE Trans. on Industry Applications*, vol. 24, pp. 987-997, November/December 1988.

[13]S. Morimoto, K. Hatanaka, Y. Tong, Y. Takeda, and T. Hirasa, "High Performance Servo Drive System of Salient Pole Permanent Magnet Synchronous Motor," *In Proc. of IEEE IAS Annual Meeting*, pp. 463-468, 1991.

[14]S. Morimoto, M. Sanada, and Y. Takeda, "Wide-Speed Operation of Interior Permanent Magnet Synchronous Motors with High-Performance Current Regulator," *IEEE Trans. on Industry Applications*, vol. 30, pp. 920-926, July/August 1994.

[15]J.-M. Kim and S.-K. Sul, "Speed Control of Interior Permanent Magnet Synchronous Motor Drive for the Flux Weakening Operation," *IEEE Trans. on Industry Applications*, vol. 33, no. 1, pp. 43-48, January/February 1997.

[16]M. F. Rahman, L. Zhong, and K. W. Lim, "A Direct Torque-Controlled Interior Permanent Magnet Synchronous Motor Drive Incorporating Field Weakening," *IEEE Trans. on Industry Applications*, vol. 34, no. 6, pp. 1246-1253, November/December 1998.

[17]M. Terashima, T. Ashikaga, T. Mizuno, K. Natori, N. Fujiwara, and M. Yada, "Novel Motors and Controllers for High-Performance Electric Vehicle with Four In-Wheel Motors," *IEEE Trans. on Industrial Electronics*, vol. 44, no. 1, pp. 28-38, February 1997.

[18]M. A. Rahman and R. Qin, "A Permanent Magnet Hysteresis Hybrid Synchronous Motor for Electric Vehicles," *IEEE Trans. on Industrial Electronics*, vol. 44, no. 1, pp. 46-53, February 1997.

[19]D. M. Lonel, J. F. Eastham, T. J. E. Miller, and E. Demeter, "Design Considerations for Permanent Magnet Synchronous Motors for Flux Weakening Applications," *In IEE Proc.-Electr. Power Appl.*, vol. 145, no. 5, pp. 435-440, September 1998.

[20]R. D. Lorenz and D. B. Lawson, "Performance of Feedforward Current Regulators for Field-Oriented Induction Machine Controllers," *IEEE Trans. on Industry Applications*, vol. 20, no. 6, pp. 1482-1489, November/December 1984.

[21]F. Briz, A. Diez, M. W. Degner, and R. D. Lorenz, "Current and Flux Regulation in Field-Weakening Operation," *In Proc. of IEEE IAS Annual Meeting*, 1998.

[22]L. Harnefors and H. P. Nee, "Model-Based Control of AC Machines Using the Internal Model Control Method," *IEEE Trans. on Industry Applications*, vol. 34, no.1, pp. 133-141, January 1998.

[23]M. V. Kothare, *"Control of Systems Subject to Constraints,"* Ph.D. Dissertation, California Institute of Technology, Pasadena, California, 1997.

[24]D. Borojevic, *"Nonlinear Algorithms for Fast and Robust Control of Electrical Drives,"* Ph.D. Dissertation, VPI&SU, Blacksburg, Virginia, 1986.

[25]V. R. Stefanovic and R. M. Nelms (editors), "Microprocessor Control of Motor Drives and Power Converters," IEEE Press, 1991.

[26]J. Y. Yen, C. J. Huang, and S. S. Lu, "Stability of PDF Controller with Stick-Slip Friction Device," *Journal of Dynamic Systems Measurement and Control*, pp. 486-490, September 1997.

[27]J.-W. Choi and S.-K. Sul, "Design of Fast-Response Current Controller Using *d-q* Axis Cross Coupling: Application to Permanent Magnet Synchronous Motor Drive," *IEEE Trans. on Industrial Electronics*, vol. 45, no. 3, pp. 522-524, June 1998.

[28]D. S. Marić, S. Hiti, C. C. Stancu, J. M. Nagashima, and David B. Rutledge, "Two Flux Weakening Schemes for Surface-Mounted Permanent-Magnet Synchronous Drives – Design and Transient Response Considerations," *accepted for publication and presentation at IEEE ISIE'98 Conference*, July 1999.

[29]J. Holtz, W. Lotzkat, and A. Khambadkone, "On Continuous Control of PWM Inverters in the Overmodulation Range Including the Six-step Mode," *in Proc. IECON '92*, pp. 307-312, 1992.

Chapter 4

Filtering Techniques for Improved Performance of SMPMS Drives in the Flux Weakening Regime

Previous chapters described in detail two advanced flux weakening algorithms for SMPMS machine drives. The schemes offer significant advantages over the previously known solutions. The flux weakening operation is achieved without usage of machine parameters and DC bus voltage measurement. The methods are not dependent on the conditions in the drive environment or the type of the mechanical load. An automatic transition into flux weakening is accomplished by either controlling the reference of the phase voltage magnitude or by detecting and regulating the i_q current error.

However, when the over-modulation and six-step modes are utilized, performance degradation has been observed. Namely, the fifth and seventh stator current harmonics of the fundamental frequency, generated in the over-modulation and six-step modes, propagate through the current control loops, resulting in the sixth harmonic in the reference voltage and deteriorating system performance [1].

In this Chapter, an application of a constrained notch filter (synthesized from allpass sections [2]) for proper attenuation of the unwanted harmonic content is described. The allpass-based lattice-structure filter replaces the simple, straightforward implementation of a zero order hold or moving average function. The lattice filter provides minimal phase delay

and complete attenuation of the sixth harmonic. Theoretically expected behavior of the system with the lattice filter is experimentally verified.

4.1. Drive Performance Deterioration in Over-Modulation and Six-Step PWM Regimes

The maximal DC bus voltage utilization for maximal torque production by employing the over-modulation and six-step modes [3] was thoroughly discussed in the previous chapters. As mentioned there, the maximal torque production is an essential requirement in electric propulsion applications.

As shown in [3], the boundary of the sinusoidal mode is reached for the modulation index of $d=0.867$. As d increases beyond this point, a significant level of higher harmonic content appears in the inverter output voltage. When the six-step mode is reached, the phase voltage at the inverter output, as shown in [4], is:

$$v_{phase,a} = V_1 \cos\omega_e t + \frac{1}{5} V_1 \cos 5\omega_e t - \frac{1}{7} V_1 \cos 7\omega_e t - \ldots \qquad (4\text{-}1)$$

where $V_1 = 2V_{dc}/\pi$. Therefore, in the six-step mode, as well as in the over-modulation, important fifth and seventh harmonics of the stator current are present.

By applying the transformation from a three phase a,b,c system to a synchronous d,q system, the fifth and seventh harmonics result in the sixth harmonic being present in i_d and i_q, and hence in reference voltage duty cycles d_d and d_q, as well as in the i_q error signal. Consequently, in both schemes, the loop that generates the reference i_d^* will feed back the sixth harmonic. This deteriorates drive performance and may cause instability when maximum torque is requested during the flux weakening.

Mathematically, the sixth harmonic of i_d and i_q in the six-step, [1], can be determined as follows:

$$\begin{bmatrix} i_{d,6} \\ i_{q,6} \end{bmatrix} = \mathbf{T} \cdot \begin{bmatrix} I_5 \cos(5\omega_e t + \varphi_5) + I_7 \cos(7\omega_e t + \varphi_7) \\ I_5 \cos(5\omega_e t + \varphi_5 + 120^0) + I_7 \cos(7\omega_e t + \varphi_7 - 120^0) \\ I_5 \cos(5\omega_e t + \varphi_5 + 240^0) + I_7 \cos(7\omega_e t + \varphi_7 - 240^0) \end{bmatrix} \tag{4-2}$$

where the transformation matrix is:

$$\mathbf{T} = \begin{bmatrix} \cos\omega_e t & \cos(\omega_e t - 120^0) & \cos(\omega_e t - 240^0) \\ -\sin\omega_e t & -\sin(\omega_e t - 120^0) & -\sin(\omega_e t - 240^0) \end{bmatrix} \tag{4-3}$$

and I_5 and I_7 are the amplitudes of the fifth and seventh stator current harmonics respectively. From (4-2) and (4-3) it follows:

$$\begin{aligned} i_{d,6} &= \frac{3}{2}\left(I_5 \cos(6\omega_e t + \varphi_5) + I_7 \cos(6\omega_e t + \varphi_7)\right) \\ i_{q,6} &= -\frac{3}{2}\left(I_5 \cos(6\omega_e t + \varphi_5) - I_7 \cos(6\omega_e t + \varphi_7)\right) \end{aligned} \tag{4-4}$$

Assuming that the motor back EMF contains only fundamental frequency, I_5 and I_7 are:

$$\begin{aligned} I_5 &= \frac{V_1}{5\sqrt{R^2 + (5\omega_e L)^2}} \\ I_7 &= \frac{V_1}{7\sqrt{R^2 + (7\omega_e L)^2}}. \end{aligned} \tag{4-5}$$

The sixth harmonic has to be eliminated from the flux weakening section to ensure robust drive performance in the flux weakening region.

4.2. The Sixth Harmonic Filtering

A simple, commonly used approach is to employ a zero-order-hold (*ZOH*) function or moving average filter. The Laplace domain *ZOH* transfer function is:

$$G(s) = \frac{1 - e^{-sT}}{sT} \tag{4-6}$$

In the continuous-time frequency domain, this becomes:

$$G(j\Omega) = e^{-j\Omega\frac{T}{2}} \frac{\sin\frac{\Omega T}{2}}{\frac{\Omega T}{2}} \tag{4-7}$$

The normalized frequency characteristics are shown in Fig. 4.1. The magnitude is in dB's and the phase is in degrees.

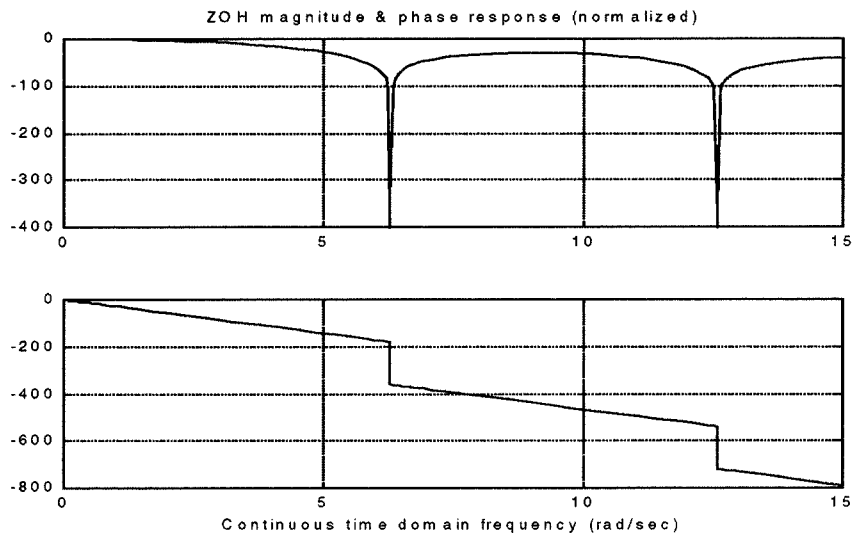

Fig. 4.1. Normalized *ZOH* characteristics (unwrapped phase), *T=1* sec, continuous domain frequency Ω.

In Fig. 4.1, we notice that, for the elimination of a certain frequency Ω_0 (rad/sec), the hold time should be $T=2\pi/\Omega_0$. Here, $\Omega_0=6\times2\pi f_{stator}$, where f_{stator} is the frequency of the SMPMS machine stator currents. Therefore, when the speed and, consequently, stator frequency change, T is adapted according to:

$$T = \frac{1}{6 f_{stator}} \tag{4-8}$$

The phase angle decreases linearly as the frequency increases, and reaches -180^0 when the notch frequency Ω_0 is approached. The phase delay goes to infinity as $\Omega \to \infty$. This can contribute to oscillatory behavior of the i_d^* and system instability during torque command transients at elevated speeds.

The fact that this simple solution only transforms the source of the drive performance degradation from one form to the other (instead of solving the problem) brought attention to the need for a proper filter solution. Since the influences of the twelfth and higher harmonics are negligible, then a single-notch frequency filter for proper attenuation of the sixth harmonic, with good frequency characteristics, is necessary. The coefficient adaptation with speed is an additional concern. The filter structure has to be computationally simple and to provide stable performance for all mechanical loads during the flux weakening operation. We bear in mind that the electrical time constants of the SMPMS drive system are very small. These requirements led to the usage of a constrained allpass-based lattice-structure notch filter [2], whose adaptive version, for instance, was previously used in [6] for communications and sonar applications. The filter order is two, it can be implemented with only two multipliers and, in such a case, the notch frequency adaptation requires that only one coefficient needs to be adjusted when the speed varies.

The straightforward implementation of the second-order notch filter, as used in [5] for instance, leads to a computationally convoluted realization. In such a case, the tuning of the filter requires that five filter coefficients must be adjusted [5]. It was pointed out in [6] that this could also bring up stability problems during the process of the notch frequency adjustments.

In this work, allpass filter blocks are used to synthesize the second-order notch filter. The structure consists of two allpass functions connected in parallel [2], [6]. The Z-domain transformed block diagram of the allpass-based notch filter is given in Fig. 4.2. The filter transfer function is:

$$H(z) = \frac{1 + A(z)}{2} \tag{4-9}$$

where $A(z)$ is a second-order allpass function: $|A(e^{j\omega})| = 1$, for every frequency ω (in radians) that corresponds to the discrete-time domain.

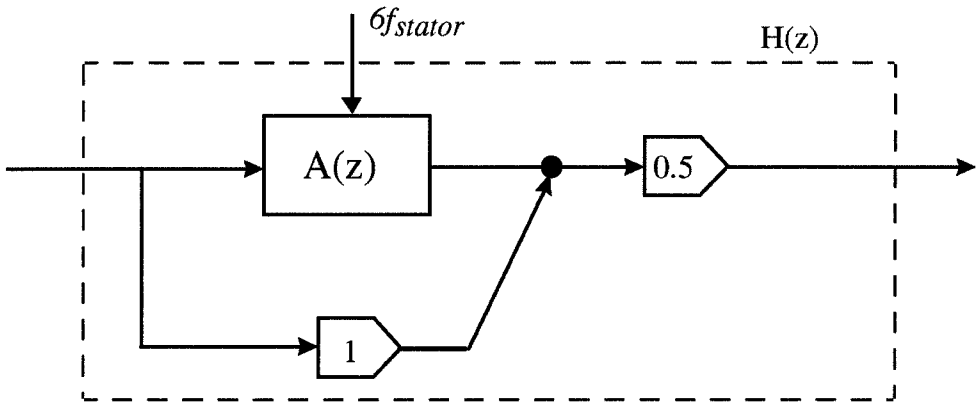

Fig. 4.2. Block-diagram of the allpass-based notch filter. The notch frequency adapts to changes in the stator frequency (i.e., drive velocity).

The notch frequency is the frequency at which the output of the second order allpass filter is in antiphase with the signal in the direct link, Fig. 4.2. Again, a structurally lossless bounded real function is used for the allpass filter. A more detailed review of allpass filters is given in [2] and [7]; however, some properties that are important for this application are reviewed here.

The numerator and denominator polynomials of $A(z)$ form a mirror-image pair. Hence, the second-order allpass function, with poles at $Re^{\pm j\theta}$, is given by:

$$A(z) = \frac{R^2 - (2R\cos\theta)\cdot z^{-1} + z^{-2}}{1 - (2R\cos\theta)\cdot z^{-1} + R^2 z^{-2}} \tag{4-10}$$

It is this symmetry that is used in the adaptive applications when the gradient function of the filter output with respect to a parameter is needed, [6].

Another important property is that allpass filters are lossless. Knowing that for any allpass function: $|A(e^{j\omega})| = 1$, for all ω, and if the transformed input and output of the filter are $X(z)$ and $Y(z)$ respectively, we obtain:

$$\left|Y(e^{j\omega})\right|^2 = \left|X(e^{j\omega})\right|^2 \tag{4-11}$$

Then, integrating both sides over the principal range gives:

$$\frac{1}{2\pi}\int_{-\pi}^{\pi}\left|Y(e^{j\omega})\right|^2 d\omega = \frac{1}{2\pi}\int_{-\pi}^{\pi}\left|X(e^{j\omega})\right|^2 d\omega \tag{4-12}$$

and by Parseval's theorem [2] this implies:

$$\sum_{n=-\infty}^{n=\infty} y^2(n) = \sum_{n=-\infty}^{n=\infty} x^2(n) \tag{4-13}$$

This shows that the output energy is equal to the input energy for an allpass filter. For this reason, these functions are also called lossless functions.

Other interesting properties of the allpass filters (such as the modulus property, the monotone phase-response property, the pole-zero relationship, the time domain meaning, and the most general form of rational allpass functions) are described in [2] and [7].

When an allpass filter is realized, a number of different structures can be used [2], [7]. The characteristics of more conventional (direct form and cascade) structures are mentioned in [7]. However, in this work, the cascaded lattice structure is used. The origins of these structures can be found in the work of Gray and Markel, [9]. Such a structure can be derived for any N^{th} order stable unit-magnitude allpass filter, and has the property that all multipliers have a magnitude less than unity. Its importance lies in the fact that the transfer function remains stable and allpass in spite of the multiplier quantization, as long as the multiplier magnitude is less than one. The realization is structurally passive. The derivation of this structure follows from the following theorem. The details are given in [7].

The order reduction. *Let $G_m(z)$ be an m^{th} order causal, stable, unit-magnitude allpass function. Then it can be implemented as in Fig. 4.3, where: (a) $|k_m|<1$, (b) $G_{m-1}(z)$ is a causal, stable, unit-magnitude allpass function with order (m-1).* ∇

The order reduction theorem sets the theoretical basis for all variations of the lattice cells presented and used in this work.

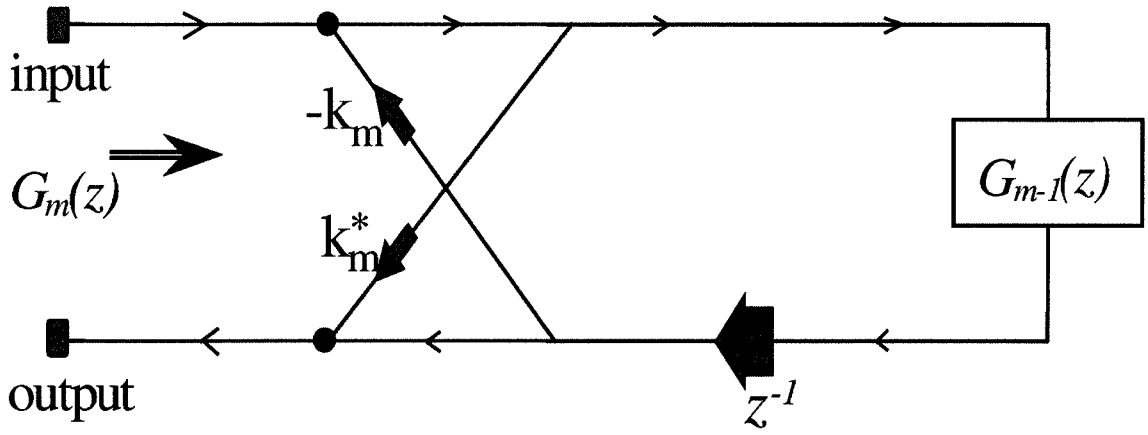

Fig. 4.3. The order reduction theorem is used for generation of the lattice structures for allpass functions.

If we repeat the reduction, we finally get the constant G_0 with $|G_0|=1$, [7]. In this application, we need a real coefficient filter. As shown in [7], in such a case, the coefficients k_m in the lattice are real and less than 1 for all m. Also, G_0 is real and equal to one. This is important for the stability of the system, as mentioned above, but it is very useful to have the multipliers bounded within the *(-1,1)* interval for a digital implementation in the assembly code. z^{-1} is the unit delay block.

When this is applied to our case of the second order, real coefficient allpass function, the resulting structure is shown in Fig. 4.4. The total number of multipliers is four. Using the lattice coefficients [2], the allpass function can be expressed as:

$$A(z)=\frac{k_1+k_2(1+k_1)z^{-1}+z^{-2}}{1+k_2(1+k_1)z^{-1}+k_1z^{-2}} \tag{4-14}$$

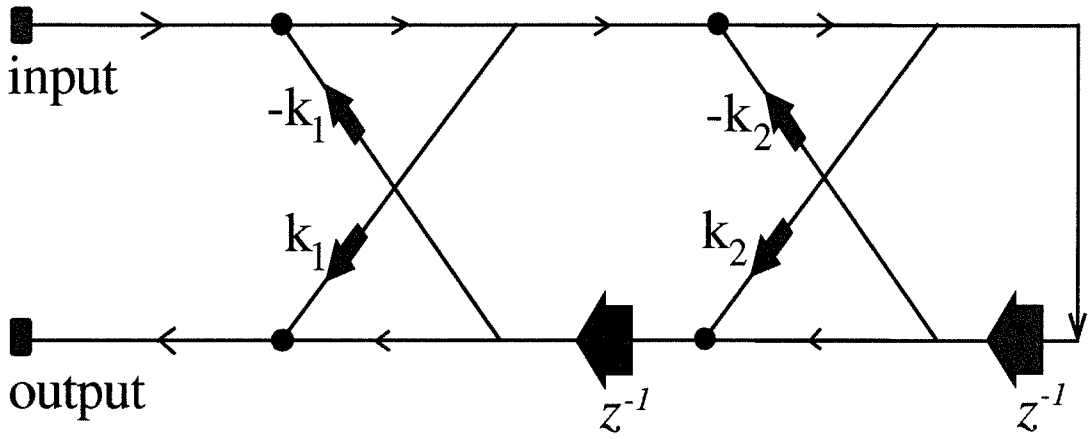

Fig. 4.4. Lattice structure for a real second-order allpass function $A(z)$.

Now, from equations (4-9) and (4-10), the transfer function of the notch filter in Fig. 4.2 can be written as:

$$H(z) = c\frac{1-(2\cos\omega_o)z^{-1}+z^{-2}}{1-(2R\cos\theta)z^{-1}+R^2z^{-2}} \tag{4-15}$$

where $\cos\omega_0$ and c satisfy:

$$\cos\omega_o = \frac{2R}{1+R^2}\cos\theta \tag{4-16}$$

$$c = \frac{1+R^2}{2} \tag{4-17}$$

The additional scaling c in (4-15) and (4-17) means that the notch filter has unity gain at DC (the steady state values of the variables in the synchronous *d-q* reference frame are DC) and at the Nyquist frequency.

A normalized discrete-time frequency response of the filter is given in Fig. 4.5. The phase characteristic is unwrapped. A complete attenuation of the desired harmonic can be achieved, whereas the filter phase delay stays bounded within the $(-90^0, 90^0)$ interval over the entire frequency range. When the drive speed changes, the stator frequency varies; hence, the notch frequency has to be properly adjusted.

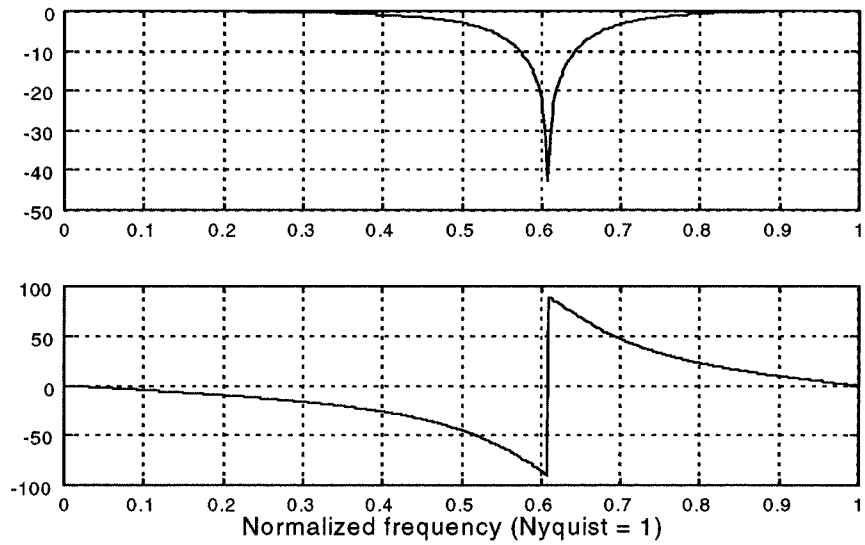

Fig. 4.5. Normalized characteristics of the notch filter, discrete-time domain frequency, unwrapped phase.

When we compare these characteristics with the characteristics shown in Fig. 4.1, we see that the phase characteristic problem is resolved. The added advantage is that the 3dB notch bandwidth can be independently selected according to the maximal allowable phase delay.

From equations (4-10) and (4-14) – (4-16), the lattice coefficients can be expressed in the following form:

$$k_1 = R^2; \qquad k_2 = -\cos\omega_o \tag{4-18}$$

It was shown in [2] and [6] that the 3dB notch bandwidth is:

$$B_W = 2\tan^{-1}\left(\frac{1-R^2}{1+R^2}\right) \tag{4-19}$$

From equations (4-18) and (4-19), it follows that the adaptation of the notch bandwidth and notch frequency can be achieved independently with a separate adjustment of coefficients k_1 and k_2 as the machine stator frequency (rotor speed) varies.

The strategy used here is to preset the notch bandwidth, as in [1], by selecting the coefficient k_1 and, then, to adjust only the notch frequency parameter k_2 as the velocity varies. Therefore, the poles of the notch filter are constrained to lie on a circle within and concentric to the unit circle in the z plane, equation (4-18), when the notch frequency is changed. The k_2 adjustment, according to equation (4-18), follows a cosine function of the desired notch frequency:

$$\omega_o = 6 \times (2\pi f_{stator}) / f_s \tag{4-20}$$

where f_{stator} is the stator frequency of the machine, directly proportional to the rotor speed, and f_s is the sampling frequency used by the digital controller. Since the sampling frequency

is fixed, the k_2 calculation requires a fixed-coefficient cosine table, independent of any drive parameters or operating conditions.

In our case, we use the real coefficient filter, when the structure of the second order allpass function can be implemented with only two multipliers [2], Fig. 4.6, retaining the possibility for the orthogonal tuning of the notch bandwidth and frequency.

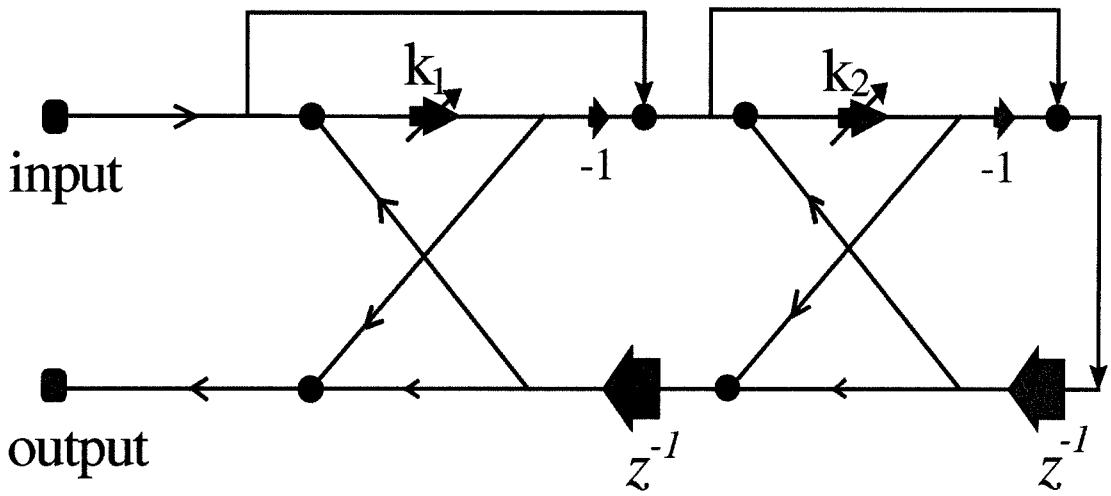

Fig. 4.6. The second order allpass $A(z)$ lattice structure with only two multipliers.

This structure is preferred from the computational point of view. However, for implementation with a fixed-point digital signal processor, some internal lattice signals can overflow, depending on the numeric range of the signals at the input of the filter. This can be handled by using different numeric representations of the numbers to cover the expected range of all signals (for instance, 3.13 representation instead of 1.15). Too wide scaling is not acceptable because of the correspondingly decreased numeric precision. Consequently, in such situations, normalized lattice sections [10] can be utilized.

For our flux weakening application, the worst numeric case occurs when the phase voltage reference control is employed. In such a situation, the maximum expected value at the filter input is two. The practical solution in our fixed-point processor includes the 3.13 numeric representation and the structure shown in Fig. 4.7. The first cell still uses only one multiplier, whereas the second cell is implemented with the aforementioned normalization.

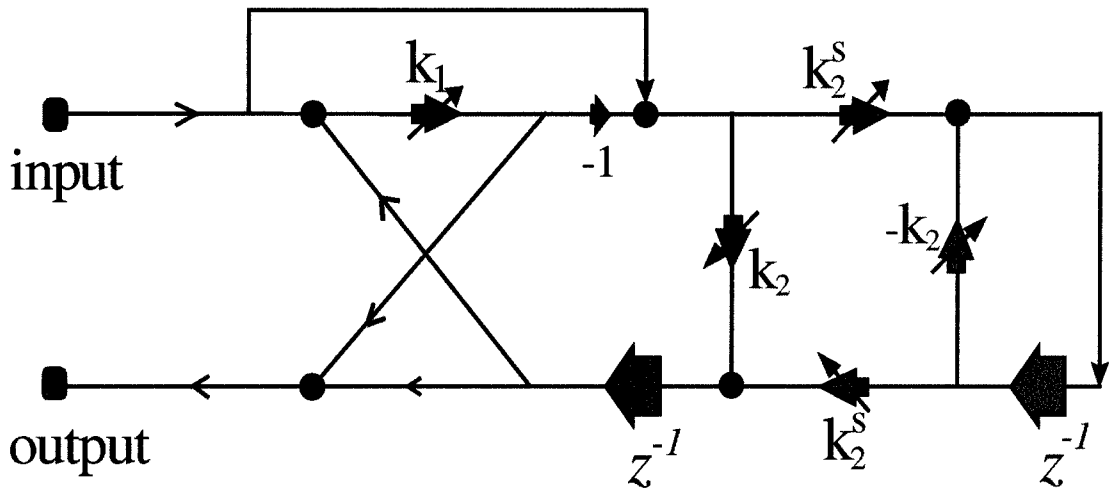

Fig. 4.7. An example of $A(z)$ realization for the fixed-point processor implementation.

The advantageous stability properties of the normalized cell with varying coefficients were pointed out in [10]. The coefficient k_2^s is determined according to:

$$k_2^s = \sqrt{1 - |k_2|^2} \tag{4-21}$$

Using the equations (4-18) and (4-20), we determine that this multiplier requires a simple, fixed sine lookup table:

$$k_2^s = |\sin \omega_0| \tag{4-22}$$

4.3. Simulation

As discussed at the beginning of this chapter, the sixth harmonic has to be filtered before it penetrates into the flux weakening section, when the over-modulation and six-step are utilized. It means that, in Figs 3.4 and 3.13, signals d^e and i_q^{err} ought to be filtered at the entrance of the flux control algorithm.

To prove the effectiveness of the filtering block, the computationally more complex scheme with closed loop voltage reference control is used, Fig. 4. 8. First, the simulations are performed and then the same operation is experimentally verified. The error detection scheme can be analogously modified by adding the filter before i_q^{err} enters the flux section in Fig. 3.13.

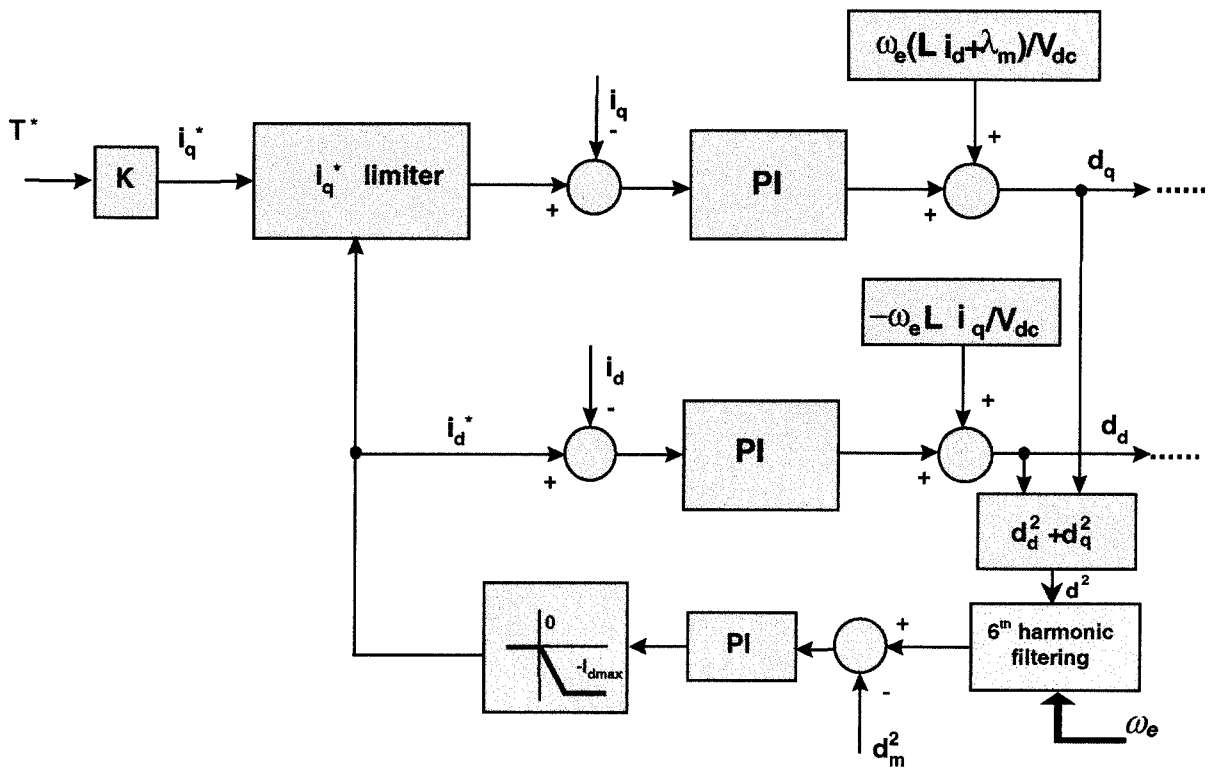

Fig. 4.8. Flux weakening voltage control scheme with improved performance during over-modulation.

The simulation model discussed in the previous chapters was modified to include the filter block. The over-modulation and six-step were enabled again. The results for the acceleration test with the torque generated by the PM machine corresponding to $i_q^*=0.3$ *p.u.* are shown in Fig. 4.9. Below 2000 rpm, the flux weakening operation is disabled. The coefficient $k_f=R^2$ was set to *0.5*, which was sufficient for this application. When the phase lag introduced by the filter needs to be minimized over the certain frequency range (below the notch frequency), the k_f should be accordingly increased. As previously mentioned, the stability is assured as long as we retain $|k_f|<1$.

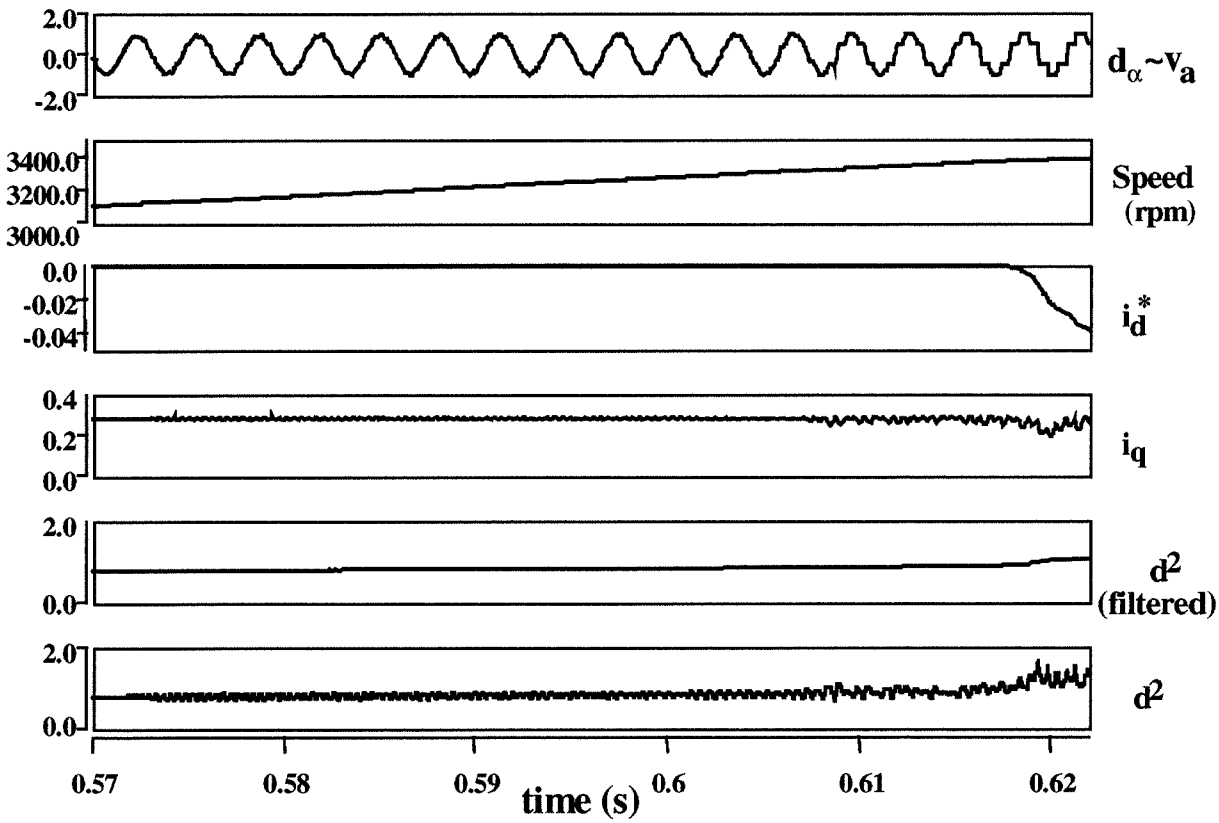

Fig. 4. 9. Validation of the filter operation – simulation results.

The transition into six-step mode begins at 3100 rpm. The sixth harmonic appears as soon as the over-modulation is entered. As the inverter goes through the over-modulation region and further into the six-step, the amplitude of the sixth harmonic increases. The sixth harmonic can be observed in the current i_q, as well as in the unfiltered d^2. Once the voltage limit is closely approached, the flux weakening operation begins. We notice that the filter operation is effective (see d^2 trace after the filtering) and the sixth harmonic is not fed back through the reference i_d^*.

The simulation results confirmed the expected merits of the technique. A complete attenuation of the undesired harmonic component was achieved. Then, the scheme was implemented on the drive prototype.

4.5. Experiment

To verify the filter operation, the coefficient k_1 was set to the same value as it was used in simulations and the structure from Fig. 4.7 was implemented. Fig. 4.10 illustrates the coefficient k_2 adaptation with speed over the entire range. Over the required speed range in our application, the k_2 stays on the monotonous part of the cosine function, far enough from its maximum and minimum, ensuring good sensitivity.

Fig. 4.11 shows the unfiltered and filtered values of the square of the modulation index d^2, as well as the characteristic shape of the phase during the six-step operation. As a result, we see that the sixth harmonic is properly attenuated in the flux weakening section, i.e., the filtered d^2 is flat as expected in the d-q synchronous operation during steady state operation.

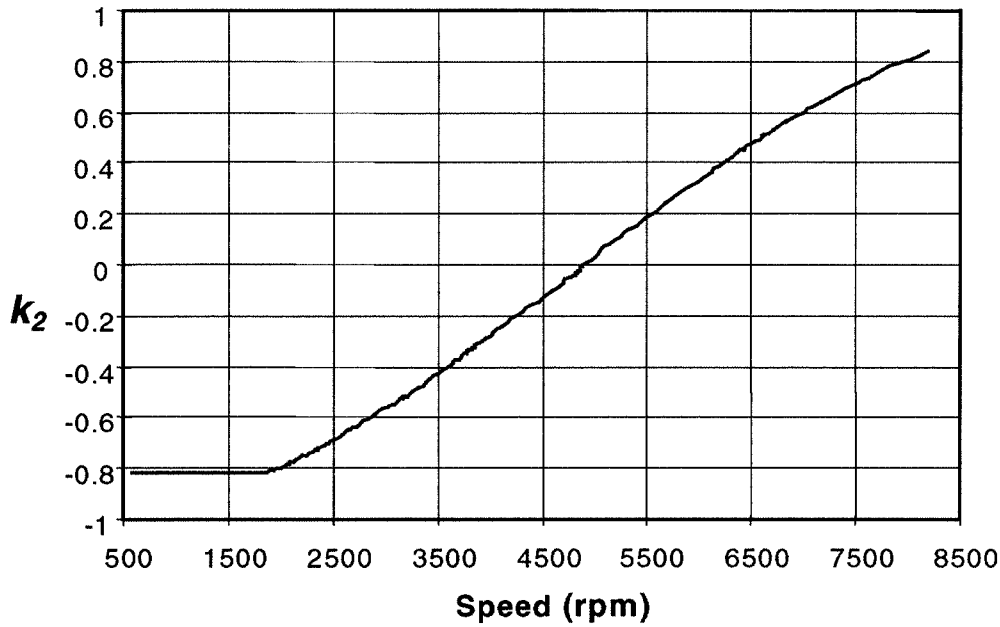

Fig. 4.10. Coefficient k_2 adaptation with rotor speed over the full flux weakening region (experimental result).

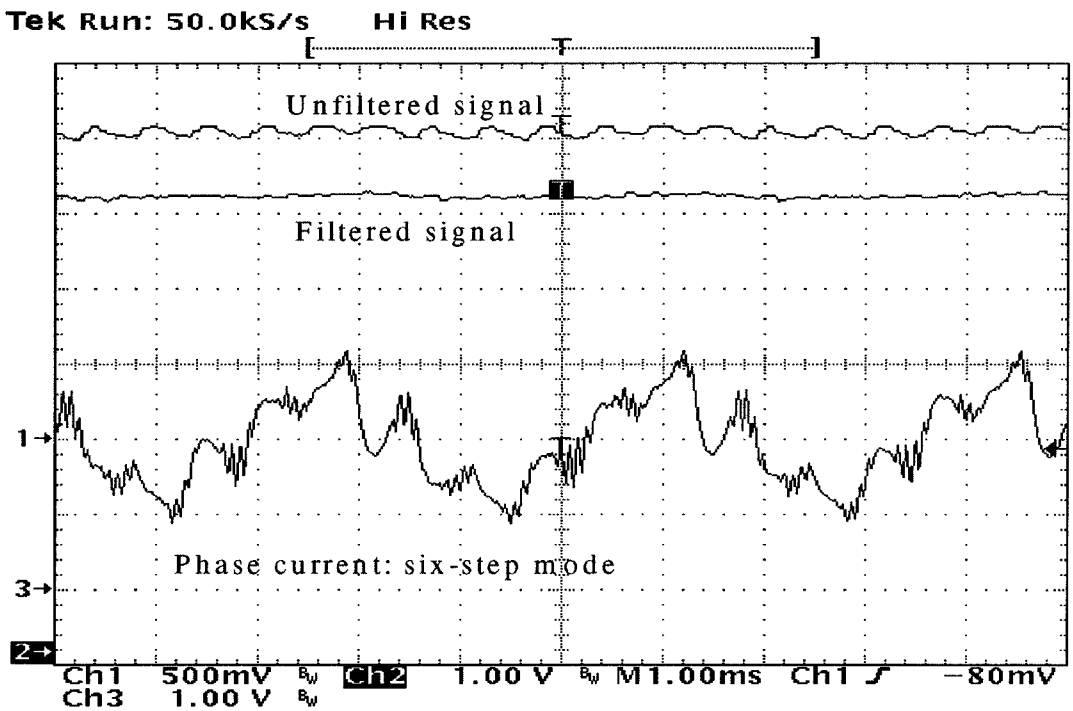

Fig. 4.11. Experimental verification of the filter operation (six-step mode).

4.6. Concluding Remarks

The constrained notch filter synthesized from allpass sections has been used here as a part of an advanced electrical drive control algorithm, improving the performance and stability of the system operating at elevated rotor speeds in the flux weakening region. The over-modulation and six-step modes introduce the sixth harmonic into the flux weakening control section, which significantly deteriorates drive performance.

The filter has a low order transfer function, still providing the desired amplitude and phase characteristics. Its realization is structurally passive and the adaptation of the notch bandwidth and notch frequency is orthogonal. These characteristics ensure a stable drive performance in the flux weakening region when high torque is needed. Also, the filter is very suitable for real-time control of drive systems because of minimized computational requirements for its implementation.

This notch filter, either as an adaptive or non-adaptive version, can be applied in other power electronics and machine control applications, wherever its characteristics are important for the design.

References

[1] D. S. Marić, S. Hiti, C. C. Stancu, J. M. Nagashima, and D. B. Rutledge, "Robust Flux Weakening Scheme for Surface-Mounted Permanent-Magnet Synchronous Drives Employing an Adaptive Lattice-Structure Filter," *In Proc. of IEEE APEC99 Conference*, pp. 271-276, March 1999.

[2] P. A. Regalia, S. K. Mitra, and P. P. Vaidyanathan, "The Digital All-Pass Filter: A Versatile Signal Processing Building Block," *In Proc. IEEE*, 76, (1), pp. 19-37, January 1988.

[3] J. Holtz, W. Lotzkat, and A. Khambadkone, "On Continuous Control of PWM Inverters in the Overmodulation Range Including the Six-step Mode," *In Proc. IECON '92*, pp. 307-312, 1992.

[4] D. W. Novotny and T. A. Lipo, *"Vector Control and Dynamics of AC Drives,"* Calderon Press • Oxford, ISBN: 0198564392, 1996.

[5] S. N. Vukosavić and M. R. Stojić, "Suppression of Torsional Oscillations ina a High-Performance Speed Servo Drive," *IEEE Trans. on Industrial Electronics*, vol. 45, no.1, pp. 108-117, February 1998.

[6] J. A. Chambers and A. G. Constantinides, "Frequency Tracking Using Constrained Adaptive Notch Filters Synthesised from Allpass Sections," *In IEE Proceedings, Vol. 137, Pt. F, No. 6,* pp. 475-481, 1990.

[7] P. P. Vaidyanathan, *"Multirate Systems and Filter Banks,"* Prentice Hall, ISBN: 0136057187, 1993.

[8] A. V. Oppenheim and R. W. Schafer, *"Discrete-time Signal Processing,"* Prentice Hall, Englewood Cliffs, 1989.

[9] A. H. Gray, Jr. and J. D. Markel, "Digital Lattice and Ladder Filter Synthesis," *IEEE Trans. on Audio Electroacustics*, vol. AU-21, pp. 491-500, December 1973.

[10] A. H. Gray, Jr. and J. D. Markel, "A Normalized Digital Filter Structure," *IEEE Trans. on Acoust., Speech, Signal Process.*, vol. ASSP-23, pp. 268-277, June 1975.

Chapter 5

Discussion and Suggestions for Future Work

The past several years have been an exciting time to work in the area of electrical drive systems, in particular for vehicle applications. The digital control has become a dominant approach used in drives and corresponding power electronics systems. This has led to a vast application of digital control theory in this area, where a more traditional analog, continuous-time approach dominated until the late 1980's. The progress has been supported by the tremendous pace of advances in semiconductor technology. However, the current status of the field still leaves enough space for introduction of discrete-time, digital solutions and innovations that, so far, have been used and investigated in other non-related areas of electrical engineering. Also, certain specifics of various electrical drive control techniques motivate work on novel solutions in digital systems theory that can be beneficial to aforementioned, more established areas of discrete-time systems and control.

The SMPMS machine drives have been pushed aside when compared with interior PM and induction motor drives, over the period of time in question. The SMPMS-based systems have been considered difficult to control (e.g., for flux weakening and sensorless algorithms), but their high energy efficiency and low price have attracted significant interest from automotive industry. This work described, in detail, some effective flux weakening techniques that can extend the operating speed range of the drive to satisfy the EV requirements. The emphasis was put on the demands of electric propulsion, but the algorithms are applicable to different high-performance drive systems. The presented flux

weakening algorithms do not require any knowledge of exact values of the system parameters and are independent of any conditions in the environment. However, certain applications (because of different constraints: performance, price and likewise) may require further modifications of the algorithms, their combination with parameter-dependent algorithms, as well as different loop design techniques than these shown here. This work pointed out some interesting avenues for further research work in the area of flux weakening for high-speed operation and showed that SMPMS machines can be utilized in high-performance, wide-speed-range motor drives. The impact of the high harmonic content during the over-modulation on the control system performance in the flux weakening region was shown for the first time and a remedy was proposed. However, different solutions may be investigated in the future. For example, i_q and i_d current components can be filtered immediately after the A/D conversion and transformation of the phase currents. In our system, with small time constants and limited allowable processor speed and calculation time, this was not possible, but may be considered in different motor drives, when necessary. On the other hand, similar or related signal processing modules can be used in numerous power electronics and drives systems. For instance, adaptive or non-adaptive versions of the filter used here can be employed for sensorless velocity and position control of motor drives, based on frequency tracking or other techniques. Present solutions for sensorless velocity and position control of SMPMS drives suffer from serious performance degradation at low speed (e.g., solution in [2]) or are too complex and expensive for practical applications in industry.

Another area of interest encompasses efficiency improvement algorithms. So far, the work was focused on IPM and PM DC brushless drives, for example [3] – [7]. Efficiency is a critically important factor in EP systems for autonomous electric vehicles due to limited

energy supply. Hence, extensions of existing solutions to SMPMS drives, as well as development of new models and algorithms, should be properly addressed in the future.

Although a certain amount of work was invested in developing fault-tolerant PM drives (the latest example is presented in [8]), a practical, effective and low-cost scheme has not been proposed yet. Namely, PM machines produce high amplitude back EMF in the stator windings during the flux weakening operation at elevated speeds. In case of a failure of one or more inverter switches, or some other fault in the control circuitry, the high values of uncontrolled back EMF can initiate modes of operation that are dangerous for the hardware and, possibly, the drive operators. Currently, brute-force solutions increase the space required and price of the PM drives, i.e., more elegant solutions are needed and expected.

Even though this work describes necessary details for developing a fully operational, practical system (which is currently being tested on a prototype electric vehicle), there is space left for work on modeling and control techniques for SMPMS drives since their qualitative and market competitiveness has been proven.

References

[1] D. S. Marić, S. Hiti, C. C. Stancu, J. M. Nagashima, and David B. Rutledge, "Two Flux Weakening Schemes for Surface-Mounted Permanent-Magnet Synchronous Drives – Design and Transient Response Considerations," *accepted for publication and presentation at IEEE ISIE'98 Conference*, July 1999.

[2] D. S. Shet, H. A. Toliyat, and T. A. Nondahl, "Position Sensorless Control of Surface Mount Permanent Magnet AC (PMAC) Motors at Low Speeds," *In Proc. IEEE APEC'99 Conf.*, pp. 1219-1225, 1999.

[3] K. Atallah and D. Howe, "The Calculation of Iron Losses in Brushless Permanent Magnet DC Motors," *Journal of Magnetism and Magn. Materials*, vol. 133, pp. 578-582, 1994.

[4] A. K. Nagarkatti, O. A. Mohamed and N. A. Demerdash, "Special Losses in Rotors of Electronically Commutated Brushless DC Motors Induced by Non-Uniformly Rotating Armature MMFs," *IEEE Trans. on Power Apparatus and Systems*, vol. PAS-101, no. 12, pp. 4502-4507, December 1982.

[5] P. Brissonneau and D. Lebouc, "Core Losses with Trapezoidal Wave Form of Induction," *IEEE Trans. on Magnetics*, vol. MAG-20, no. 5, pp. 1484-1486, September 1984.

[6] R. Schiferl and T. A. Lipo, "Core Loss in Buried Magnet Permanent Magnet Synchronous Motors," *IEEE Trans. on Energy Conversion*, vol. 4, no. 2, pp. 279-284, June 1989.

[7] S. Vaez, *"Loss Minimization Control of Interior Permanent Magnet Drives,"* Ph.D. Dissertation, Queen's University, Kingston, Ontario, Canada, 1997.

[8] M. Zigliotto, M. Zordan, and S. Bolognani, "Experimental Fault-Tolerant Control of a PMSM Drive," *In Proc. IEEE IECON'98 Conf.*, vol.1, pp. 492-297, 1998.

Appendix A

EV Battery Technologies – An Overview

An autonomous electric vehicle requires the presence of energy storage devices. Currently, an electrochemical battery package is the most widely accepted approach. The specific energy and power of the batteries are, in general, much smaller than those of gasoline or diesel fuel, resulting in a large number of batteries needed to provide an acceptable level of EV performance. However, this can significantly reduce luggage and interior space, increase the weight and cost of the vehicle and deteriorate system performance. Therefore, the development of battery technology has been accelerated. The set of main concerns includes: specific energy, specific power, energy efficiency, charging rate, cycle life, operating environment, cost, safety, and the feasibility for recycling, [1] – [3]. The challenge of transforming EV's from concept to reality is to make it safe, convenient and easy for users to charge batteries. Hence, significant attention has lately been devoted to the development of charging systems, [5] – [8].

A.1. Batteries

Until recently, the most mature battery solution appropriate for electric vehicles was based on lead-acid (Pb-acid) technology. Currently, nickel-based batteries are more and more attractive, like nickel-iron (Ni-Fe), nickel-cadmium (Ni-Cd) and especially nickel-metal hydirde (Ni-MH). Also, zinc-halogen batteries such as zinc-bromine (Zn-Br), high-temperature batteries, such as sodium-sulfur (Ni-S), and lithium-based have been

investigated. However, high-temperature, as well as lithium-based batteries, come with increased safety concerns, when utilized in automotive applications. Table A.1 lists the characteristics of available commercial batteries for electric vehicle applications.

Battery	Cell voltage (V)	Specific energy (Wh/kg)	Specific power (W/kg)	Cycle life
Pb-Acid	2.0	35	100	700
Ni-Cd	1.2	45	250	2000
Ni-MH	1.2	80	245	1500
Zn-Br	1.6	80	50	350
Na-S	2.0	80	150	800

Table A.1. Comparison of latest EV batteries.

Lead-acid battery is the most widely used battery. It uses sponge lead for the negative electrode, lead oxide for the positive, and a sulfuric acid solution for the electrolyte. As the cell discharges, the active material is converted into lead sulfate and the sulfuric acid solution is diluted. On charge, the reverse actions take place. Maintenance-free designs, in which the electrolyte is immobilized and loss of water is minimized, have been introduced. However, the limitations for EV applications are the battery's poor low-temperature characteristics (especially its inability to accept charge at low temperatures), its loss of capacity on stand (self-discharge) and its relatively weak mechanical structure.

Nickel-cadmium batteries offer higher power capability, long cycle-life, good low-temperature performance, ruggedness, and reliability. This battery uses nickel oxide for the positive electrode, cadmium for the negative, and an alkaline solution (potassium hydroxide) for the electrolyte. The Ni-Cd battery requires little maintenance and can take considerable abuse. Unlike the Pb-Acid battery, it can be stored in either a charged or discharged

condition without damage. The self-discharge rate is very low. However, the lighter Ni-MH battery, using a hydrogen storage alloy (like Mg-Ni alloy) as the negative electrode has emerged as a currently most promising solution for EV applications due to its significantly higher specific energy but acceptably long cycle life. Also, the Ni-Cd battery requires deep discharge, without which it would develop memory, manifested in shorter and shorter discharge cycles. The latest Ni-MH batteries have almost no memory.

For the future, the EV industry is seeking better batteries to ensure a range between charges that is comparable with ICE systems. The most promising long-term solution utilizes the lithium-based batteries, [9]. The lithium-ion batteries come with increased safety concerns. The lithium polymer batteries are sometimes referred to as the "copper" of the future, [9]. The two electrodes are separated by a thin, ionically conductive polymer membrane acting both as an electrolyte and as a separator between electrodes. The anode electrode is made of ultra-thin lithium foil that serves both as a lithium source and a current collector. The positive electrode is a material based on a reversible intercalation compound of vanadium oxides, which is blended with polymer electrolyte and carbon to form a plastic composite that is backed by a metal foil current collector. The operating temperature is normally maintained at 60 – 80°C. The lithium polymer battery is considered to be the best long-term solution for powering electric vehicles. However, as it was pointed out in [9], this technology is at its early stage, and it will take 5 – 10 years to bring these batteries into full production for EV applications. At the same time, it is expected that, within the ten-year horizon, these batteries should support a viable EV alternative to present ICE systems.

The DC resistance of a battery pack varies greatly depending on numerous operating conditions. However, in general, Pb-acid resistance is higher than Ni-MH, whereas the lithium-based batteries promise further decrease in the DC resistance.

Many researchers are excited by the idea of coupling electrochemical batteries with electric flywheels or ultra-capacitors, which can deliver surges of power. Recently, ultrahigh-speed flywheels, also known as electromechanical batteries, have been reported to have the potential to deliver as much as 5000-10000 W/kg, what is an order of magnitude higher than anything currently achievable with an electrochemical battery. However, at present, the flywheel technology suffers from difficulties in extraction of mechanical energy from ultrahigh-speed rotating systems, as well as from discouraging safety concerns for passenger vehicles.

Another subject of intensive research in the EV industry is a fuel cell system. The operation of the fuel cell is similar to that of the battery except that one or both of the reactants are not permanently contained in the electrochemical cell, but are fed into it from an external supply when power is desired. The fuels are usually gaseous or liquid, and oxygen or air is the oxidant. The most promising solutions include hydrogen cells. A comprehensive treatment of fuel cells is given in [4].

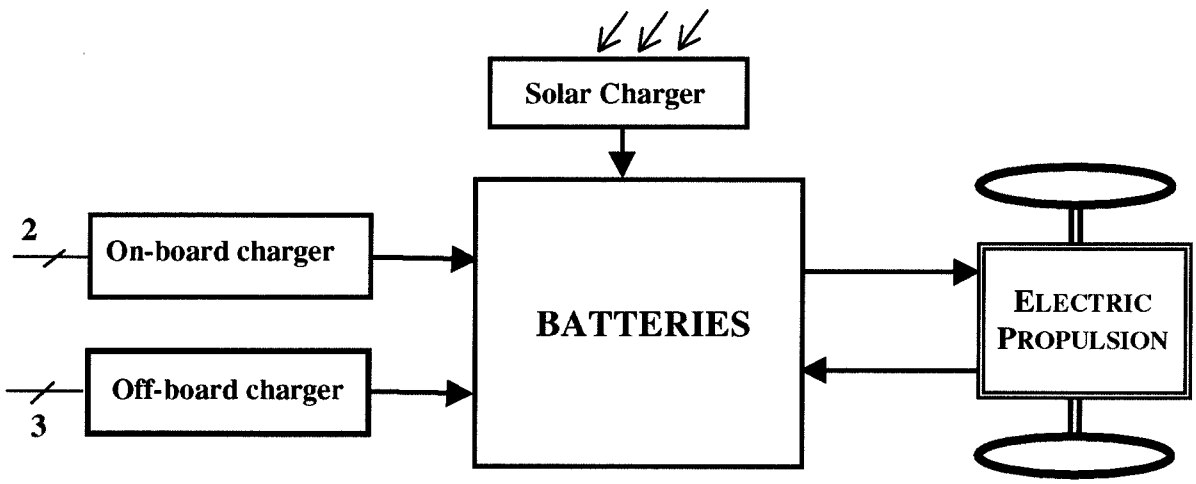

Fig. A.1. Multiple EV charging system.

A.2. Battery Charging

In order to improve convenience and increase charging efficiency, a number of charging methods have been proposed [1]: home charge, regenerative charge, solar charge, park-and-charge, and move-and-charge. Fig. A.1 shows a possible multiple-charging system, aimed to charge batteries using various charging schemes on the same vehicle. An EV is usually parked at home or a storage site at night, the battery charger in the vehicle can be connected into the domestic single-phase AC plug for slow nighttime charging. Depending on the battery capacity and depth of discharge, the charging time takes about 6-8 hours, [1]. The inexpensive, lightweight and compact battery chargers are essential for home charge. As the electricity demand at night is relatively low, this home charge scheme can facilitate the load level control of power utilities.

During deceleration or downhill motion, the EV propulsion machine is operated as a generator to charge batteries through regenerative braking. Therefore, a four-quadrant inverter and drive controller is used in electric propulsion. In the General Motors EV1, for instance, this extends the driving range up to 25%. In order to enhance the use of energy, some manufacturers (Nissan) intend to use solar cells embedded in the vehicle's roof.

When an EV is parked at a charging station, a digitally controlled three-phase off-board charger initiates the power flow and controls the transfer to the vehicle. Charge equalization schemes can be employed to avoid overcharging batteries and to improve the battery life [6]. During quick charge, the current is typically over 100A. Thus, efficient three-phase AC-DC converters with very high current capability are essential for the park-and-charge systems. It should be noted that, from the utility power of view, rapid charge might not be desirable because of the high peak power demand. An incentive-based electricity

billing system can be established to encourage customers to use quick charge only for emergency purposes at dedicated charging stations.

As an alternative to a plugging-type power transfer, an inductive power transfer has recently been developed for the park-and-charge system, [7]. The system features an inductive coupler with a coil that is completely encased in a plastic-covered paddle. The vehicle is equipped with a charging port that also incorporates a coil. This inductive charging system is inherently safe under all weather conditions, i.e., tolerant to water, snow, ice, dirt and dust. To provide a lightweight and compact inductive charging port, low mass magnetic cores and high-frequency AC-DC converters are necessary. Currently, there are systems with power levels from 1.5 kW to 50 kW, with overall efficiency better than 90%, while the power transfer frequency is 40-350 kHz.

To end on a more futuristic note, the most ideal situation for charging EV batteries is to perform the charge while the vehicle is cruising on the road, the so-called move-and-charge method, [1]. This system would be embedded on the surface of a section of highway, the charging zone, and does not need any additional space. The inductive approach is more promising for this purpose than the conductive realization, both for dependability and safety reasons.

References

[1] C. C. Chan and K. T. Chau, "An Overview of Power Electronics in Electric Vehicles," *IEEE Trans. on Industrial Electronics*, vol. 44, pp. 3-13, February 1997.

[2] W. H. Deluca, A. F. Tummilllo, J.E. Kulaga, C. E. Webster, K. R. Gillie, and R. L. Hogrefe, "Performance Evaluation of Advanced Battery Technologies for Electric Vehicle Applications," *In Proc. of Intersoc. Energy Conversion Eng. Conference*, pp. 314-319, 1990.

[3] D. Coates and L. Miller, "Advanced Batteries for Electric Vehicle Applications," *In Proc. of International Electric Vehicle Symposium*, no. 14.03, 1992.

[4] "Fuel Cells Handbook," DOE/METC-88/6096, US Department of Energy.

[5] J. K. Nor, "Fast Charging Advances the Art of Refueling Electric Vehicles," *In Proc. of International Symposium on Automotive Technologies Automation*, pp. 65-72, 1991.

[6] S. T. Hung, D. C. Hopkins, and C. R. Mosling, " Extension of Battery Life via Charge Equalization Control," *IEEE Trans. on Industrial Electronics*, vol. 40, pp. 96-104, 1993.

[7] "Electric Vehicle Chargers," Hughes Power Control Systems, Torrance, CA, 1992.

[8] C. A. Bleijs and J. L. Mazoyer, "Preparing the Infrastructure for the Charging of Tomorrow's Electric Cars," *In Proc. of International Electric Vehicle Symposium*, no. 9.02, 1992.

[9] *1998 EVS-15 Symposium*, Lectures Sessions: Batteries, Brussels, 1998.

Appendix B

Permanent Magnet Materials

Permanent magnets are vital components of many electromechanical systems, but they are usually hidden in subassemblies. System designers and end users often give too little thought to how choice and use of the PM material affect performance, size and cost of the product. Revolutionary developments have recently occurred in the field of permanent magnetism. Hard ferrite became an abundant, inexpensive material, while rare-earth magnets raised the coercivity by an order of magnitude and remanence to above three times the value for ferrites. As a consequence, a rapid broadening of magnet usage is now happening. A confluence of recent developments in PM's, power devices and microprocessors is particularly apparent in the area of drives and motion control [1].

Sintered and cast AlNiCo alloy magnets were the first commercially available materials. Now, their use is decreasing [2]. The main constituents are aluminum, nickel, cobalt and iron, together with a number of other elements. They are alloyed and cast. The resulting material is heat-treated to develop the magnetic properties. AlNiCo can also be sintered. This process is particularly suitable for small parts. All AlNiCo magnets feature a high remanent induction B_r, excellent thermal stability and feasible high temperature operation. The really weak point of this material is its low coercivity H_c, making it very susceptible to demagnetization by external fields.

Sintered ferrite magnets became available in the 1950s. This type of magnet is produced by the powder metallurgy process from a compound of ferric oxide and a

carbonate of either barium or strontium. The sintered compact is very hard and brittle and is often referred to as ceramic. The benefits of this material are cost effectiveness, good corrosion and chemical resistance, as well as a wide range of operating temperature (up to 250°C). Ferrites are very good electrical insulators. Therefore, eddy current losses inside the magnet caused by external magnetic fields do not play a significant role. Their main disadvantage is a relatively low B_r.

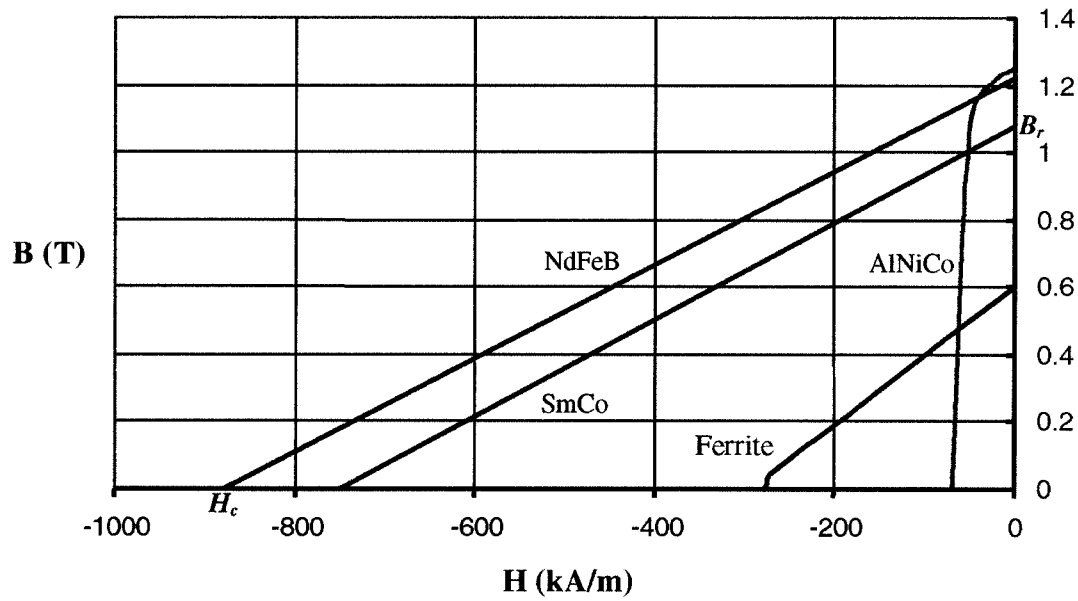

Fig. B.1. Typical demagnetization characteristics at room temperature (20°C).

In the 1960's a magnetic alloy of cobalt with the rare earth element samarium was discovered. This material produces a strong magnet with a linear demagnetization curve, and thus a strong resistance to demagnetizing fields. This quality was a major advance in magnetic materials. The energy density was increased by a factor of six when the Sm_2Co_{17} phase was discovered. This grade became commercially available in the 1970's. The material is produced by the powder metallurgy process and the magnet is field oriented during pressing. The sintered compact is both hard and very brittle. This material has high B_r and

H_c, Fig. B.1, and it is anisotropic. The direction of magnetization is usually in the direction of the thickness of the sample. SmCo is electrically conducting. The weaknesses of this material are the careful handling required to prevent chipping and breaking and its very high price because the strategic materials Sm and Co are not abundant on the market.

Neodymium iron boron (NdFeB) magnets offer the highest energy density presently available from various manufacturers. Sumimoto Special Metals Company and General Motors discovered it in 1983, and they hold the patents for the alloy. The production route is a powder metallurgy process similar to that of SmCo, [3]. The main features of this material are its very high B_r and H_c, Fig. B.1, and its good machinability properties. It is mechanically stronger, less prone to chipping and has lower cost compared to SmCo alloys. Also, it is anisotropic. The direction of magnetization is usually in the direction of the thickness of the magnet. It conducts electricity. The main weaknesses are its strong temperature dependent properties given its low Curie temperature and its tendency toward corrosion.

To select a proper material for a specific application, some general physical criteria should be followed:

- A high value of energy product $(BH)_{max}$ results in a compact electromagnetic design at a given output power.
- A high value of remanent flux density B_r results in high forces and torques.
- A high value of coercivity H_c results in high demagnetization resistance, especially important in electrical drive applications that require a wide speed range in the flux weakening regime. A permanent demagnetization must be avoided.
- A straight-line characteristic of the demagnetization portion of $B=f(H)$ curve results in low losses during dynamic operation.

These criteria list only the technical requirements. The PM material expenses play a highly important role for all production applications. Some of latest improvements in the materials (important for motor drives applications) are described in [4] and [5].

New developments in material science toward temperature stability, processing cost and advanced magneto-mechanical properties have resulted in investigations of nitride PM alloys, for instance, [6]. Those investigations in the laboratories are very recent. However, the small amount of existing information shows promise for the future development of PM machine technologies.

References

[1] B. K. Bose (editor), "Power Electronics and Variable Frequency Drives – Technology and Applications," IEEE Press, 1997.

[2] K. Hameyer and R. J. M. Belmans, "Permanent Magnet Excited Brushed DC Motors," *In Trans. on Industrial Electronics*, vol. 43, pp. 247-255, April 1996.

[3] M. Sagawa, S. Fugimura, N. Togawa, H. Yamamoto, and Y. Maysuura, "New Material for Permanent Magnets on a Base of Nd and Fe," *Journal of Applied Physics*, vol. 55, no. 6, pp. 2083-2087, 1984.

[4] R. H. Richman and W. P. McNaughton, "Permanent-Magnet Materials: Research Directions and Opportunities," *Journal of Electronic Materials*, vol. 26, no. 5, pp. 415-422, May 1997.

[5] A. S. Kim, "Design of High Temperature Permanent Magnets," *Journal of Applied Physics*, vol. 81, no. 8, pp. 5609-5611, April 1997.

[6] H. Oda, K. Kondo, H. Uchida, Y. Matsumura, S. Tachibana, T. Kawanabe, and K. Midori, "A Samarium Iron Nitride Magnet Fabricated by Shock-Compaction Technique," *Japanese Journal of Applied Physics, Part 2-Letters*, vol. 34, no. 1A, pp. L35-L37, January 1995.